Tuning Tumor Vasculature to Amplify Focused Ultrasound Therapy

---

A

Dissertation

Presented to

the faculty of the School of Engineering and Applied Science

University of Virginia

---

in partial fulfillment

of the requirements for the degree

Doctor of Philosophy

by

Mark Schwartz

May 2025

APPROVAL SHEET

This

Dissertation

is submitted in partial fulfillment of the requirements
for the degree of

Doctor of Philosophy

Author: Mark Schwartz

This Dissertation has been read and approved by the examing committee:

Advisor: Richard J. Price, Ph.D.

Advisor:

Committee Member: Mete Civelek, Ph.D.

Committee Member: Timothy N.J. Bullock, Ph.D.

Committee Member: Andrew Dudley, Ph.D.

Committee Member: Sepideh Dolatshahi, Ph.D.

Committee Member:

Committee Member:

Accepted for the School of Engineering and Applied Science:

Jennifer L. West, School of Engineering and Applied Science

May 2025

Acknowledgements

I came to the University of Virginia expecting to move into a long career in R&D, and I am unfathomably grateful to everyone who has shaped my winding path into something completely different. First and foremost, Rich, I (obviously) wouldn't be here today without you taking in a rotation-less student in March of 2020 and welcoming me to the lab with open arms. You've shaped me into a better engineer, scientist, and self-advocate. You've made me reach beyond my own professional comfort zones. You've wholeheartedly supported me pursuing professional avenues you know so little about without doubting my ability to keep my dissertation moving. And above all else, you've always put us students first, for which I am eternally grateful. But as every Price Lab member knows, Rich is one pillar of the lab, and Ji is another. Despite my occasional forgetfulness and mess, you've always pushed me to be a better scientist, have kept our lab running unbelievably smoothly in every single way, and are always a fabulous gossip. Rich and Ji, without your constant support these last five years, and I probably would have quit—or worse, worked in a lab environment that wasn't as wonderful and supportive as the one you have so carefully cultivated over the years.

Along the way, I've met and worked with some wonderful faculty members, and so I asked many of them to be on my committee. Tim, your dry sense of humor, wealth of tumor immunology knowledge, and insatiable desire for a firm hypothesis has made me a better researcher by leaps and bounds. Drew, you've taught me so much about cancer and sparked the most important ideas my dissertation, and I am forever grateful for it. Mete, you've been a wonderful mentor in the department these past few years, and I can't say thank you enough for being my chair. And Sepideh, your immunological expertise, thoughtful eye towards my work, and willingness to question its basis have made my research so much stronger. You have all made a wonderful committee, and I am indebted to you all for working with me and with one another the past years to support me and my work.

Of course, many students have shaped my time at UVA—most of all, those in the Price Lab. You are truly the people I want to be with in the worst of times, and I know that I'd be hard-pressed to find a better group of friends and coworkers. To those who have moved on from our lab: Natasha, you always question my work and push it forwards, and it has been a delight to see you grow as junior faculty—Alex, although we only briefly overlapped, your contribution to the lab culture will never be forgotten—Andrew, you made me doubt every result I ever got, but in the best way, and I miss you making me a better scientist and your griping every day—

Delaney, the lack of your laugh echoing throughout lab is a constant reminder of the incredible scientist and great friend who moved on to a post-doc at Duke last year, and we are so, so proud of you. To those who I am leaving—Matt, you have been a wonderful, goofy friend to talk about anything and everything with, and I'm endlessly thankful for your thoughtful reworking of our ablation regimens—Katie, sitting next to you for the last five years has been a wonderful, enriching experience where I've made a new friend whose hands only sometimes smell like onions but always brings a smile and an uncanny ability to place a tail vein (a good skill for a double doctor!)—Tor, from making lab art to long science conversations to complaining about who knows what, "my issue is" that we're not going to be coworkers anymore—Anna, we came into lab as Thing 1 and Thing 2 and we've been by each other's side ever since; beyond the amazing discoveries you've made, I am so proud of your perseverance and ability to stay silly in the worst of times—Lydia, you have been the most amazing source of immunology information and are the best partner on a long flow day—Kathy, you can muster up a laugh no matter what, and I'm so proud of you for pursuing options outside of R&D—Matt, we've taught each other a lot on long MRI days, not only about current events but also about the importance of not judging a book by its cover—Nareen, you have been a joy to train and build a beautiful friendship with, and you've brought me so much knowledge about the world, movies, and good eats—Tanya, your dedication to your work and healthy dose of sarcasm always brighten my day, especially when I run into you working on the weekends—Eden, your silliness and youth-filled slang makes me feel old and tired sometimes but always lifts me up—Ryan, although you're moving on from UVA, I'm proud of you figuring out what you want from your PhD so soon. Although people move in and out of our Price Lab life, it has been a fabulous five years with you all working too hard and having too much fun at the same time—I love you all and wish you the best at UVA and beyond.

Finally, my friends and family have been the most amazing support system during my time at UVA, and although you weren't all here with me, I'm sure you heard about it more than you asked to. To old friends in my cohort: thank you for being a wonderful COVID pod to lean on during a very hard year and beyond. To new friends I've met here in Charlottesville: Caylee and Ella, you two and Barkley have been the best neighbor friends we could imagine—Ellie, thank you for bringing so much joy to our lives and dinner parties—Sam, thank you for your endless support in my science policy journey. To my friends from SLU, especially the Bungalow, I am indescribably happy at how close we have stayed these past six years since graduating together—we are always there for one another, and I cherish every moment together. To my

family: Mom, every morning before school you told me to “have fun, learn lots!”, which was some of the best advice you could give me, and you have been an incredible rock and the best mom during my time at UVA—Dad, even when we don’t agree, you challenge me to think differently, which has made me a better researcher; you have been an amazing, stoic part of my support system in school and in life—Matthew, we are as similar as we are different; you’ve come a long way from the annoying little boy I used to see you as, and I’m grateful every day you tricked me into running that Turkey Trot—Gram, your sass is unmatched and even though you might think I might work at Best Buy after graduation, I love you to pieces. And finally, to my family here in Charlottesville: Millie and Finn, you were both semi-impulsive, discount dogs, but you light up my life and I cherish you crazy doodles every day. Jacob, I never could have imagined when I came to UVA that a small-town, South Carolina boy would become my best friend and the best partner I could have asked for. Not only did you bring your love for the Golden Girls, a good front porch swing, and an extra dirty martini with Grey Goose into my life, you constantly push me to be a better me, a better researcher, and have been an endless well of support these past five years during the ups and downs of life in graduate school. As we move on to our next adventure in Cincinnati, I am so incredibly proud of what you have accomplished and can’t wait to see you grow into the amazing professor I know you will be—I love you so, so much. To everyone who has played a role in supporting me during my time at UVA, both mentioned and unmentioned in these Acknowledgments, I thank you from the bottom of my heart.

TABLE OF CONTENTS

CHAPTER 1: PREFACE

1.1 ABSTRACT

For many solid cancers, metastatic spread is the primary source of patient suffering and death. Even after isolating this root cause and developing new therapies, solid tumor diagnosis is followed by a ~50% 10-year survival rate, which varies by indication. One promising class of anti-cancer drugs that has recently received attention—immunotherapy—may extend survival but fails to significantly improve the cure rate of solid tumors writ large. In tumor types which are more refractory to these treatments, properties inherent to tumors often prevent a sufficiently powerful anti-tumor immune response. And in tumor types which typically respond well, some patients still respond poorly to immunotherapy. Given the simultaneous promise and patient response heterogeneity of immunotherapy, novel approaches to improve immunotherapy's efficacy are necessary.

One intervention that enhances the effects of immunotherapy is focused ultrasound (FUS). FUS, which refers to concentrated sound energy deposition into tumor tissue in a non-invasive, non-ionizing manner, induces bioeffects ranging from blood vessel disruption to thermal ablation to mechanical fractionation of tissue. We argue that two FUS modalities could render immunotherapies more effective. First, the efficacy of immunotherapy if a larger quantity of a given drug can enter the tumor. Lower-intensity mechanical FUS (mFUS) induces the oscillation of systemically administered, gas-filled microbubbles (MBs). When targeted to the site of the tumor, these MBs temporarily disrupt tumor blood vessels and permit greater drug delivery. mFUS has been shown to augment drug delivery, especially in the brain. Second, the efficacy of immunotherapy may improve when an immune stimulus is introduced. Thermal FUS (tFUS) leverages short pulses of high-intensity ultrasonic energy to heat tumor tissue above 70°C, causing tissue damage and releasing tumor antigen and damage-associated molecular patterns

(DAMPs) allowing the host immune system more tools to “see” the tumor. Although tFUS as a monotherapy has not been consistently shown to provide sustained solid tumor control, studies combining tFUS with immunotherapy demonstrate encouraging results. We expect both mFUS and tFUS to separately enhance immunotherapy’s efficacy.

In many contexts, mFUS can effectively augment drug delivery to tumors. However, we anticipate that its capacity to drive drug delivery can be further improved by pharmaceutically modulating tumor blood vessel function prior to mFUS treatment—solid tumors vasculature is systematically dysfunctional compared to that of healthy tissue and likely impede maximal mFUS efficacy. As cancer cells proliferate, the resulting neoplasm requires oxygen and nutrients. Pro-angiogenic cell-cell signaling then accelerates, causing the rapid formation vessels whose aberrant construction prevents them from functioning adequately. Chronically poor tumor vessel function is expected to constitute a major impediment to successful cancer treatment, likely contributing to patient unresponsiveness to drugs like immunotherapeutics. Anti-angiogenic drugs have previously been found to improve tumor vessel function in a concept known as “vascular normalization”, most notably by blocking vascular endothelial growth factor receptor 2 (VEGFR2). Since vascular normalizing drugs have been shown to improve both drug delivery and immune-related metrics within tumors, we expect this class of drugs to enhance the effects of both mFUS and tFUS.

In Aim 1 of this dissertation, we combine mFUS and a VEGFR2-blocking antibody, DC101, to study how modulating tumor vasculature can improve FUS-mediated drug delivery. First, we test if DC101 induces vascular changes in a 4T1 murine triple-negative breast cancer model—we find that DC101 reduces blood vessel coverage and increases blood vessel function as assessed by histology and live perfusion imaging, respectively. We then leverage magnetic resonance imaging (MRI) to quantify intratumoral delivery of two MRI-visible model drugs following DC101 treatment, with and without mFUS. The delivery of Gadovist, about the size of a

chemotherapeutic, is enhanced by both DC101 and mFUS individually. DC101 and mFUS additively augment Gadovist delivery, and additionally, improve the distribution of Gadovist throughout the tumor. The delivery of Gadospin-D, about the size of an antibody fragment, is synergistically improved with DC101 and mFUS. Finally, we refine mFUS parameters to maximize Gadospin-D delivery, demonstrating that treatment point density and FUS peak-negative pressure must be judiciously balanced to realize DC101-mediated benefits to mFUS drug delivery. We ultimately find that the capacity of mFUS to drive model drug delivery and homogenize model drug delivery distribution is significantly enhanced by vascular normalization, with model drug size and mFUS parameters being important variables.

In Aim 2 of this dissertation, we examine how VEGFR2 blockade, anti-PD1 immunotherapy, and tFUS synergize to control primary tumor growth and induce prolonged anti-tumor immunity. First, we confirm that DC101 generates a more immunologically favorable environment in two murine triple-negative breast cancer (TNBC) models, EMT6 and 4T1. We then find that, as others have shown, that tFUS, DC101, and anti-PD1 alone do little to abrogate tumor growth and eradication. However, combining DC101 with tFUS, anti-PD1 with tFUS, and all three therapies in both the EMT6 TNBC model and YUMMER1.7 melanoma model greatly improves primary tumor growth, tumor eradication, and animal survival. Not only does the triple combination group eradicate 80% of tumors, but all three combinations listed above yield contralateral rechallenge rejection, which we find to be dependent on T cells. These studies highlight not only immunomodulatory drugs DC101 and anti-PD1 can boost tFUS' capacity to drive long-term, anti-tumor immune responses, but that DC101 may be a more effective drug to combine with tFUS than anti-PD1, which is a commonly used immunotherapy in the clinic.

1.2 Preview of Dissertation

In Chapter 2, we present background information for mFUS, tFUS, and VEGFR2 blockade. In Chapter 3, we showcase the first combination of VEGFR2 blockade and mFUS to

augment model drug delivery, wherein we employ a novel MRI platform to spatiotemporally quantify delivery dynamics and refine mFUS parameters to maximize delivery of larger model drugs. In Chapter 4, we employ a novel combination of tFUS with VEGFR2 blockade and anti-PD1 immunotherapy to induce primary tumor control, eradication, and long-term immunity. Finally, we consider future applications of the work highlighted in this dissertation in Chapter 5.

CHAPTER 2: INTRODUCTION

Solid, malignant tumors and their metastases result in human suffering and are a primary cause of death worldwide. Although scientists and clinicians have added small molecule inhibitors, immunotherapy, and even more novel therapeutics to their arsenal of surgery and chemotherapy, many patients remain refractory to the standard of care. One reason for which tumors are difficult to treat is their vasculature, or blood vessel network. Tumor blood vessels grow quickly in response to quickly proliferating tumor cells in need of oxygen and nutrients—as a result, these vessels are large, malformed, tortuous, and leaky compared to those in healthy tissue. These undesirable vessel properties are a major driver of solid tumor treatment challenges, as demonstrated throughout Chapter 2 and the remainder of this dissertation.

2.1 SOLID TUMORS

2.1.1 THE STATE OF SOLID TUMOR THERAPY

Cancer-related deaths adjusted to population continue to decline in the United States—the number of deaths per 100,000 individuals sank from 173.5 to 146.2 between 2009 and 2019 [1]. A 15% decline in deaths due to cancer in just 10 years is a testament to increased testing and awareness as well as the pursuit of novel methods to address cancer's lethality. However, not all cancer is created equal—of the 12 most commonly diagnosed cancers and the 8 most deadly cancers in the United States in 2024, about 90% of the cases diagnosed and 90% of the reported deaths were due to solid tumors and their metastases [2]. Solid tumors are not only more common but present unique treatment challenges compared to hematological malignancies, which arise from in the blood or bone marrow. With a dense stroma [3], immunosuppressive microenvironment [4], and dysfunctional vasculature [5], solid tumors present efficacy roadblocks that prevent novel drugs and therapies from even accessing the tumor itself, which significantly hampers their effect.

Nonetheless, as cancer treatment innovation has moved beyond chemotherapy and surgical resection, scientists have begun to design therapies that function as more of a molecular scalpel as opposed to a sledgehammer. Many cancer cells can be targeted with therapeutics that bind to receptors or ligands on or within cells of interest, decreasing the toxicity of these more tailored treatment options. The advent of immunotherapy has brought drugs to the clinic that spark immune reactions against cancer itself, which can generate long-term immunity within patients against their cancer and prevent relapse. And gene therapy has sought to treat solid tumors by genetically repairing cellular functions that have gone awry and introducing new proteins in cancer cells to make them more visible to the immune system, among other genetic manipulations. And yet, the current armamentarium of clinical approaches devised in biomedical laboratories is insufficient to treat so many patients as evidenced by relatively low complete response rates and short survival timelines for patients with several solid cancer subtypes.

2.1.2 Clinical Need for Improved Solid Tumor Therapies

Although clinical need depends on solid tumor etiology, several tumor characteristics prevent curative treatment. One such challenge is therapeutic targeting—many tumors do not express proteins or ligands that are easily targeted with clinically available drugs. Triple-negative breast cancer (TNBC) falls under this umbrella, where the patient standard of care typically involves a combination of radiotherapy, chemotherapy, and immunotherapy [6]. All of these interventions often harm a patient's healthy tissue, eliciting undesirable side effects [7]. Moreover, they also require the administration of a much higher drug dose into the patient than a targeted approach may necessitate [8]. This higher drug dose can incur both severe systemic side effects and financial cost upon the patient.

Another challenge related to molecular targeting is the entry of therapeutics into the tumor itself. Many treatment regimens cannot spatially target the tumor itself—injections of pharmaceutics into the tumor is invasive and varies in effectiveness—further contributing to on-

target, off-tumor toxicity in other tissues. More importantly, many novel therapeutics are larger in size compared to chemotherapeutics and small-molecule inhibitors (e.g. tyrosine kinase inhibitors). These larger molecules' size prevents them from adequately penetrating into tumor tissue to reach target cells. In addition to tumors' dense extracellular matrix, which hinders molecular motion within a tumor's parenchyma [9], many tumors exhibit high fluid pressure within the interstitial space around blood vessels. This elevated extravascular pressure prevents the convective transport of molecules into the surrounding tumor tissue [10], especially for larger molecules like immunotherapies and less so for smaller molecules like chemotherapies. For these reasons, designing interventions that improve therapeutic penetration and accumulation in tumors is essential to maximize therapeutic effect, especially when many novel therapeutics are substantially larger than clinical standard of care drugs.

Finally, patient responsiveness to immunotherapy remains a challenge. This novel class of cancer drugs stimulates the immune system to more effectively abolish cancer cells and, as a monotherapy, improves patient outcomes in certain patient subsets [11]. However, many solid tumors are immunologically "cold", or devoid of T cells with significant immunosuppressive immune populations [12] and often low mutational burdens [13]. A lack of T cells for immunotherapy to act on, and neoantigens for immune cells to recognize, leaves many patients with "cold" tumors unresponsive to immunotherapy—this leaves an enormous efficiency gap in a theoretically promising class of cancer therapies. Combining immunotherapies with one another or with chemotherapy has been shown to increase their efficacy [14], [15], but this often results in severe immunological side effects [15]. Given the potential for immunotherapy to improve long-term patient outcomes, it is essential to maximize the efficacy of immunotherapies currently employed in the clinic.

2.2 Focused Ultrasound (FUS)

Focused ultrasound (FUS) is a clinical solution to challenges in spatial treatment targeting and immunostimulation. Unlike diagnostic ultrasound, which sends sound waves into the body with a flat transducer to capture *in vivo* images of a patient in real time, FUS employs a curved transducer to focus ultrasonic energy into millimeter-scale volumes. When these focused sound waves are applied to a patient, FUS parameters and intensity largely dictate the resulting bioeffects—these can range from vascular disruption, which is commonly used for drug delivery applications, to thermal ablation, which is used for tissue debulking and immunotherapy, and mechanical ablation, a newer FUS modality also used for tissue debulking and immunotherapy that does not heat the targeted tissue. The first two of these effects—those related to vascular disruption and those related to thermal ablation—are leveraged in this dissertation to potentiate the utility of immunotherapy in solid tumors.

2.2.1 Mechanical FUS for Drug Delivery (mFUS)

Mechanical FUS (mFUS) is most commonly used for blood brain barrier (BBB) disruption, which aims to augment drug delivery to the brain. This is necessary due to the BBB's protection of the brain against most foreign agents, barring small lipophilic particles [16]—this inherently prevents many therapeutic agents from penetrating into the brain parenchyma. When FUS is applied to the brain and small gas-filled microbubbles (MBs) are injected into systemic circulation, the MBs volumetrically oscillate and interact with vessel walls in the sonicated region, causing disruptions in intercellular junctions and temporarily permeabilizing the sonicated vasculature [17]. When drugs are intravenously injected alongside these MBs, FUS-mediated vascular permeabilization permits larger molecules to extravasate into the surrounding brain tissue, improving local drug delivery [18][19][17]. These applications of FUS extend to the clinic, where FUS has proven effective at increasing small-molecule drug delivery in the brain [20][21], including in brain tumors [22][23].

Separate from the context of the BBB, many characteristics of tumor vasculature are not amenable to drug accumulation in extracranial tumors. Tumor blood vessels are characteristically leaky [24], which permits fluid and serum proteins from blood to seep into the space surrounding the vessels [25]. As fluid accumulates in the extravascular space, interstitial pressure rises [26]. This does not hamper the accumulation of small molecules as much as larger molecules, as smaller molecules depend more heavily on diffusion than convection due to their size [27]. Therefore, vascular leakiness and the high interstitial pressure that ensues in tumors prevents the extravasation of larger drugs—such as antibody biologics, a major class of immunotherapies—into the tumor parenchyma. FUS has been shown to augment the targeted delivery of larger molecules to solid tumors, which can partially overcome the physical barrier that tumor blood vessels present.

Several groups have investigated the application of FUS and MBs in solid tumors outside from the brain, including those studying the delivery of fluorescent dyes [28], doxorubicin, a common chemotherapy [29], and fluorescently labeled nanoparticles [30]. While these studies shed light on the ways that ultrasound can be used to drive drug delivery in solid tumors, a gap of understanding remains in how FUS-mediated delivery can be spatially and temporally quantified across a range of drug sizes and FUS parameters. Given the promise of mFUS that these studies present, it is essential to better understand how mFUS treatment can be refined to maximize drug delivery. This is particularly true for larger molecules given the substantial delivery challenges they face and the newer class of promising therapeutics they represent.

2.2.2 Thermal FUS for Thermal Ablation (tFUS)

Another common application of FUS is for thermal ablation of tissue. Several energy deposition modalities, including laser interstitial thermal therapy (LITT), microwave, radiofrequency, cryoablation, electroporation, and thermal ablation with focused ultrasound

(tFUS) [31], are commonly deployed to debulk solid tumors in the clinic. While these non- or minimally-invasive ablative techniques are typically leveraged to elicit local cancer cell death, modulation of tumor immune landscape is also known to occur in many instances [32], [33], [34], [35], [36], [37], [38], [39], [40], [41], [42], [43], [44], [45]. For example, while tFUS is typically used to elicit coagulative necrosis [46], debulk neoplasms [47], and temporarily control primary tumor growth [48], [49], [50], it also induces damage-associated molecular pattern expression [51], [52], liberates tumor antigen [53], and drives several other responses that may be associated with anti-tumor immunity [4], [5], [6]. Since cancer metastasis primarily drives patient mortality in many cancer subtypes (e.g. breast cancer and melanoma), it is important to consider how these immunological responses to tFUS can be leveraged to drive systemic anti-tumor immunity against distal metastases. Yet, despite tFUS' ability to modulate tumor immune landscape [28], [30], [32], [33], [34], [35], there is little evidence that tFUS as a monotherapy can robustly and reproducibly control metastatic disease.

For this reason, many researchers have begun to incorporate other therapies into tFUS regimens. tFUS has primarily been combined with drugs which may stimulate anti-tumor immunity, and in some studies this combination can drive immune-mediated tumor control [54], [55], [56], [57]. Given the limitations for tFUS application as a monotherapy, it is imperative to investigate combinations of tFUS with other immunostimulatory drugs, particularly drugs that are already on the market or in clinical trials.

2.3 Tumor Vasculature and Vascular Normalization

2.3.1 Characteristics of Tumor Blood Vessels

Many characteristics of solid tumor vasculature present significant obstacles to the effective treatment of cancer. First, tumor vessels are inherently leaky [58]—this leakiness originates from rapid pro-angiogenic signaling that occurs as tumors grow and require more

angiogenesis to supply new tissue with nutrients [59]. As these vessels grow much more rapidly than those in healthy tissue, endothelial proliferation becomes de-coordinated with the recruitment of supporting cells like pericytes that maintain vessel stability [60]. Leakiness of fluid and serum proteins into the surrounding tumor tissue is a result of the rapid endothelial expansion observed in solid tumors. At first glance, this may seem to enhance drug accumulation in tumors. However, excessive fluid within tumors augments the fluid pressure outside of vessels, preventing convective transport of molecules within the bloodstream [61]. Though this may not impact small-molecule drugs like chemotherapies due to their small size, it more likely impacts large drugs, such as many immunotherapies and advanced drug and gene delivery constructs, whose transport depends more on convection [62]. Due to the increased development and theoretical promise of these large, biologics, it is imperative to design delivery systems that can overcome the effects of vascular leakiness in solid tumors.

Second, tumor blood vessels are tortuous and poorly organized. Unlike in healthy tissue, where capillaries are regularly spaced to ensure that tissue oxygenation and nutrient transport is homogenous throughout a given tissue, rapid cancer and endothelial cell proliferation yields heterogeneous vascularization throughout the tumor [63]. Under-vascularized pockets of the tumor often lack adequate blood flow and are challenging for systemically injected pharmaceutical agents to access, rendering these regions nearly impossible to effectively treat [64], [65]. This fundamental quality of tumor vascular networks necessitates the development of interventions capable of overcoming inherently non-homogenous drug delivery within tumors.

Finally, tumor blood vessels foster immunosuppression, which stems from two main sources: hypoxia and dysregulated cell adhesion molecule expression. The aforementioned heterogeneous vasculature within tumors not only affects drug delivery, but also often results in hypoxia due to insufficient oxygen exchange. Many cancer cells can survive in hypoxic conditions, unlike cells from health tissues, including the immune cells essential for mounting

anti-tumor immune responses [66]. Intratumoral hypoxia impairs both T cell effector function and proliferation [67], [68], [69] and dendritic cell function [70], which are two key immune cell subsets responsible for cancer cell recognition and killing. Myeloid-derived suppressor cells (MDSCs), however, survive comparatively well in hypoxic conditions, where they continue to carry out immunosuppression [71], [72]. In addition to essential cells experiencing limited function in hypoxic environments, tumor blood vessels fail to upregulate cell adhesion molecules (CAMs), a phenomenon known as endothelial anergy. CAMs like vascular cell adhesion molecule 1 (VCAM-1) [73], intercellular adhesion molecule 1 (ICAM-1) [73], E-selectin [74], and P-selectin [74], [75] are essential for T cell rolling, adhesion, and extravasation from blood vessels into the surrounding tissue, and their chronically low expression in tumors renders vessels chronically unresponsive to the numerous inflammatory signals present within tumors [76], [77], [78]. This makes T cell extravasation into tumors less likely, hindering effector T cell function—in other words, low CAM expression prevents the patient's immune system from recognizing and fighting against a growing tumor. Ultimately, tumor blood vessels not only impede drug delivery, but also stymie anti-tumor immune responses.

2.3.2 Anti-angiogenic Drugs and Vascular Normalization

Preclinical studies in the early 2000s began to demonstrate that many unfavorable tumor vessel characteristics could be reversed, at least temporarily, by administering low doses of anti-angiogenic drugs [79], [80], [81], [82]. Unlike high doses of anti-angiogenic drugs, which mostly ineffective at preventing cancer progression and improving patient survival in clinical trials [83], [84], [85], lower doses of these same drugs have been shown to modulate tumor vessel form and function in a phenomenon known as "vascular normalization".

Vascular normalization has been found to reduce tumor vessel diameter, make tumor vessels leaky, render them more phenotypically mature [86], diminish intratumoral interstitial fluid pressure [87], homogenize blood flow [88], augment perfusion throughout the tumor [89],

lower intratumoral hypoxia [90], [91], increase adhesion molecule expression on vessel lumens [92], [93], and enhance T cell extravasation into tumors [94], [95]. Although this intervention alone does not substantially impact tumor growth, vessel normalization has been found to improve both drug delivery and immunological deficiencies which typically hinder therapeutic efficacy in tumors. Vascular normalization has been shown to improve delivery of nanoparticles to tumors [96], especially smaller nanoparticles. This size dependency illustrates how making tumor blood vessels more functional may make smaller molecules accumulate more readily in tumors, as they depend more on diffusion, but leaves room to explore how modulating tumor vessel properties may enhance delivery of immunotherapy and larger nanoparticles. The combination of vascular normalization with immunotherapy (ITX) such as anti-cancer vaccines [97], [98], [99], adoptive immune cell transfer [100], [101], [102], and immune checkpoint inhibitors (ICIs) [103], [104], [105], [106], [107], [108], [109], [110], [111] has increased ITX effectiveness in controlling tumor growth and eliciting systemic anti-tumor responses. This is thought to be due to subsequent upregulation of cell adhesion molecules on tumor blood vessels, which facilitate immune cell extravasation into tumors, and increased oxygenation within tumors, which can improve T cell function. Given the propensity of vascular normalization to change drug delivery and immunological dynamics within tumors, we see ample opportunity to combine anti-angiogenic drugs with mFUS and tFUS. We expect that the increased functionality of tumor blood vessels following anti-angiogenic therapy will augment the efficacy of therapeutic focused ultrasound in the context of solid tumors, both to augment drug delivery and to drive anti-tumor immune responses.

2.3.3 Vascular Normalization in Genetically Engineered Mouse Models of Cancer

To date, most preclinical studies examining vascular normalization have centered around implantable tumor models, where a bolus of cells is injected into a mouse to induce

murine cancer. Vascular access is required to sustain the growing tissue, which results in upregulated pro-angiogenic signaling that vascular normalization hinges upon. However, human cases of cancer rarely grow this rapidly with sustained angiogenesis—in lieu of using transplantable cancer models, a more faithful rendition of human cancer can be recapitulated using inducible genetically engineered mouse models (GEMMs) of cancer. Depending on the method used to genetically manipulate the mice, these models of cancer can either occur spontaneously or can be induced by tamoxifen injection, both of which yield a slower-growing cancer on a genetically modified background [112]. In addition to extensively characterization of vascular normalization in transplantable tumor models, it has importantly been studied in GEMMs as well.

Low-dose anti-angiogenic drug administration in GEMMs largely recapitulates the body of evidence supporting vascular normalization as observed in transplantable models. Some studies demonstrate that vascular density and blood flow are affected by anti-angiogenic drugs like anti-VEGF [113] and sunitinib, a tyrosine kinase inhibitor whose targets include VEGFR2 [114], [115]. However, most anti-angiogenic research leverages vascular normalization to improve other therapies. Several studies use anti-angiogenic drugs in GEM models of colorectal cancer [116], breast cancer [117], non-small cell lung cancer [115], [118], small cell lung cancer [114], and pancreatic cancer [114] to augment the tumor control and survival benefits conferred by immune checkpoint blockade and chemotherapy. Some studies go further in linking this therapeutic benefit to an increase in CD8 T cell activity [116], [117]. And others improve drug delivery to tumors with hyaluronic acid depletion [119], a stromal normalization strategy that will be discussed in the Future Directions section.

In summary, few studies directly examine the effects of anti-angiogenic drugs on GEMM tumor vasculature, likely due to the high cost of genetically engineered mice—the studies that have probed the effects of VEGF blockade on GEMM tumor vasculature align with the results

found in implantable tumors. Most importantly, anti-angiogenic drugs are capable of boosting the effects of immunotherapy and chemotherapy across a range of GEM models, which further validates this approach as a clinically translatable therapy.

2.3.4 Clinical Applications of Anti-angiogenic Drugs and Vascular Normalization

Clinical studies have employed anti-angiogenic agents for several decades, but researchers have pivoted from the high-dose regimens that aimed to starve tumors of blood supply. These approaches proved to be ineffective due to compensatory feedback mechanisms and may have increased tumors' metastatic potential [120]. More recent clinical studies combine lower-dose anti-angiogenic drugs with other therapies, aiming to leverage the benefit of anti-angiogenic agents put forth in the vascular normalization hypothesis. The limited extant clinical [121] can reduce vessel tortuosity [122], decrease vessel size [123], [124], and can increase pericyte coverage [124]. Additionally, high circulating VEGF levels in patients receiving combination treatment correlated with a lower survival rate, but did not correlate with responsiveness to anti-VEGF alone, indicating VEGF's utility as a biomarker for vascular normalization combination therapy [125]. This indicates that many preclinical vascular normalization findings translate to clinical contexts, despite the difference between many preclinical models of cancer and human disease.

To apply the wealth of preclinical findings that anti-angiogenic drugs amplify the effects of secondary therapies, many clinical trials have examined the effects of anti-angiogenic agents in combinatory contexts. For instance, anti-angiogenic drugs have been shown to increase overall survival of patients who are also undergoing chemotherapy [126]. Renal cell carcinoma patients who had anti-angiogenic agents layered on top of anti-PD-1 immunotherapy experienced higher median progression-free survival [127]. Similar results were found with non-small cell lung cancer patients and chemotherapy [128], metastatic colorectal cancer patients

and FOLFOXIRI [129], advanced melanoma patients with immunotherapy [130], and early-stage triple-negative breast cancer patients with immunotherapy [131]. Although these studies demonstrate the ability for anti-angiogenic drugs to extend patient survival by several months compared to chemotherapy or immunotherapy alone, they also highlight the need for further optimization of anti-angiogenic dosing as well as the development of novel, more effective therapies to address human cancer.

CHAPTER 3: NEOADJUVANT VASCULAR NORMALIZATION AUGMENTS FOCUSED ULTRASOUND-MEDIATED MODEL DRUG DELIVERY TO SOLID TUMORS

Mark R. Schwartz[1#], Matthew R. Hoch[1#], G. Wilson Miller[2], Catherine M. Gorick[1], Richard J. Price[1,2]

# Authors contributed equally

1. Department of Biomedical Engineering, University of Virginia, Charlottesville, VA

2. Department of Radiology and Medical Imaging, University of Virginia, Charlottesville, VA

3.1 ABSTRACT

Background: The delivery and penetration of intravenously administered drugs into solid tumors may be augmented by focused ultrasound (FUS) combined with microbubbles. However, heterogeneous perfusion and high interstitial pressure limit the efficacy of this approach. Here, we tested whether neoadjuvant normalization of tumor vasculature could augment subsequent FUS-mediated drug delivery and penetration of two model drugs.

Methods: A VEGFR2 blocking antibody (DC101) was intraperitoneally administered to 4T1 tumor-bearing BALB/c mice to modulate tumor vasculature, which was confirmed by CD31 immunofluorescence and contrast-enhanced ultrasound. T1-mapping MRI was used to spatiotemporally quantify the influence of neoadjuvant VEGFR2 blockade, both with and without FUS, on Gadovist (model small molecule drug; 600 Da) and Gadospin-D (model biologic drug; 17 kDa) delivery and subsequent distribution in the tumor microenvironment. FUS treatment density and peak-negative pressure (PNP) were then modulated to maximize Gadospin-D delivery.

Results: DC101-normalized tumor vasculature, as evidenced by reduced vessel diameter and density and increased perfused tumor fraction. Both DC101 and FUS augmented total model small molecule drug (Gadovist) delivery; however, delivery with FUS was only marginally improved by vascular normalization. For the model biologic drug (Gadospin-D), neither FUS nor vascular normalization alone enhanced total delivery; however, when preceded by vascular normalization, total FUS-mediated Gadospin-D delivery was increased by ~80%. Importantly, the spatial distribution of Gadovist, but not Gadospin-D, was far more uniform when vascular normalization preceded FUS treatment. We additionally find that DC101-mediated Gadospin-D delivery enhancement varies across FUS parameters.

Conclusions: Clinically feasible neoadjuvant vascular normalization has the potential to markedly augment the therapeutic efficacy of FUS-mediated drug delivery to solid tumors.

3.2 Introduction

Malignant solid tumors account for ~90% of cancer cases diagnosed each year, [132] amounting to 1.8 million patients in 2023. Several obstacles reduce the efficacy of anti-cancer drugs for treating said patients. One major challenge is the limited delivery and penetration of many intravenously administered drugs into solid tumors. Drug delivery is hindered by heightened pro-angiogenic signaling within the tumor microenvironment, which causes dysregulated vessel growth[59], poor pericyte coverage [58], and fluid and plasma leakage into the tumor microenvironment[58]. In turn, this causes high interstitial tumor pressure, leading to poor convective transport into the tumor [133]. The lack of a convective transport gradient ultimately limits the amount of drug that may enter the tumor from the systemic circulation [134]. In addition to limiting drug delivery, the heterogenous and disorganized tumor vasculature results in tumor regions with limited to no drug exposure [135]. This lack of drug delivery, coupled with heterogeneous drug exposure across the tumor volume, is a challenging clinical problem.

Focused ultrasound (FUS), applied in conjunction with systemically administered microbubbles (MBs), is a noninvasive platform to overcome this hurdle and augment drug delivery to solid tumors [136]. FUS causes the gas-filled microbubbles to volumetrically oscillate and interact with vessel walls in the target tissue [17]. These interactions are now well-known to be capable of improving drug delivery [18][19][17]. In the clinic, FUS has proven effective at increasing small-molecule drug delivery [20][21], including in brain tumors [22][23]. Nonetheless, many characteristics of tumor vasculature that limit passive drug delivery likely limit FUS-mediated delivery as well. Tortuous and dilated tumor vessels may yield unpredictable levels of energy transfer from oscillating microbubbles, heterogenous blood flow will limit the access of microbubbles to some tumor regions, and high interstitial fluid pressure will still prevent convective transport, even after FUS has been applied. These represent significant delivery

barriers given the recent development of effective anti-cancer immunotherapeutics, nanoparticle drug delivery systems, and gene therapies.

In these studies, we propose that reversing aberrant characteristics of solid tumor vasculature via “vascular normalization” (VN) will improve subsequent FUS-mediated drug model delivery. VN has been proposed as a solution to tumor vessel dysfunction [137]. Most VN approaches curb angiogenic signaling [138], [139] or extracellular matrix (ECM) production [140] and have been found to temporarily restore “normal” vessel function in preclinical tumor models. This normalized vasculature contains vessels which are smaller, less leaky, and more mature [86]. The remodeled tumors often experience lower interstitial fluid pressure [87] and more homogenous blood flow[88]. Combining this concept of VN with immunotherapy has been found to augment their therapeutic effects [141], [142] and combining VN with model drug delivery has been shown to increase these drugs’ intratumoral flow rates [96].

To test whether neoadjuvant VN augments FUS-mediated drug delivery, we employed magnetic resonance imaging (MRI) in the form of T1-mapping to quantify the FUS-mediated delivery of model drugs Gadovist (605 Da) and GadoSpin-D (17 kDa). These two MRI contrast agents model small-molecule and biologic-sized drugs, respectively, and have been previously used by our group for such purposes [143]. We leveraged the resultant data to determine how neoadjuvant VN affects the ability of FUS to augment both total drug deposition and the spatial uniformity of model drug distribution throughout the tumor microenvironment.

3.3 RESULTS

3.3.1 DC101 INDUCES VASCULAR NORMALIZATION IN 4T1 TUMORS

We first verified that DC101, a vascular endothelial growth factor 2 (VEGFR2) antibody, produced the expected VN effects. We chose 4T1 as a solid tumor model due to its responsiveness to vascular normalization [96], [144],[145], its proclivity to metastasize [146], its similarities to clinical triple-negative breast cancer [147], and its difficulty to treat [148]. However, at this time point, DC101 induced visible vascular (CD31 immunofluorescence) changes in 4T1 tumors compared to IgG2-treated mice (**Figure 3.1A**). We observed trending decreases in median vessel area (**Figure 3.1B**) and vessel density (**Figure 3.1C**) and a significant decrease in total vessel area (**Figure 3.1D**). These histological findings aligned with prior publications on VN, which also found that antiangiogenic drugs reduced vessel size and density [141], [149]. To then investigate how DC101 affects the tumor vessel function by the fraction of tumor volume that is perfused, we performed contrast-enhanced ultrasound (CEUS) imaging, using B-mode to assess microbubble perfusion (**Figure 3.1E**). DC101 treatment nearly doubled the fraction of tumor perfused by microbubbles (**Figure 3.1F**), indicating that, despite blood vessels in DC101-treated tumors appearing smaller and sparser, their remodeled network structure permits a more homogeneous perfusion of tumor volume. Despite these vessel changes, there was no difference in tumor growth during this time period (**Figure 3.1G**).

3.3.2 VASCULAR NORMALIZATION AUGMENTS TOTAL FUS-MEDIATED MODEL SMALL MOLECULE DRUG DELIVERY AND IMPROVES DELIVERY HOMOGENEITY

We next tested whether FUS, in combination with MBs, increases the delivery of a model small molecule drug [Gadovist (600 Da)] to 4T1 tumors, both with and without neoadjuvant vascular normalization with DC101. First, we visualized the final T1 concentration maps of tumors in each treatment condition (**Figure 3.2A**), which qualitatively show an increase

in Gadovist concentration with the addition with DC101 and FUS, both individually and together. We then quantified the mean Gadovist concentration over time (**Figure 3.2B**) and observed a concentration plateau by the end of the scan duration. We thus compared the final Gadovist concentration between groups and found that the $DC101^{+}/FUS^{+}$ mean Gadovist concentration generated a nearly two-fold and significant increase in VN^{-}/FUS^{-} mean concentration (**Figure 3.2C**). To more fully capture the time component of delivery, we then calculated and the area under the curve (AUC) of these concentration curves, which represent the total exposure of the tumor to Gadovist within this time period [150]. Individually, DC101 ($DC101^{+}/FUS^{-}$) and FUS ($DC101^{-}/FUS^{+}$) increased average Gadovist exposure by ~30%, with a more powerful 70% increase when added together ($DC101^{+}/FUS^{+}$) (**Figure 3.2D**).

We then compared the spatial delivery distributions of Gadovist following VN and/or FUS using statistical metrics that indicate distribution uniformity: coefficient of variation and kurtosis.

First, we assessed the coefficient of variation (COV) of the model small drug distributions between $DC101^{-}/FUS^{-}$ and the other three treatment conditions. The COV illustrates the concentration distribution's standard deviation normalized to the mean concentration and can be utilized as a measure of the dispersion of concentration values about the mean. For example, a lower COV implies that the distribution has more values with a small absolute difference to the mean value. $DC101^{+}/FUS^{+}$ yielded a trending ~30% decrease in distribution COV compared to $DC101^{-}/FUS^{-}$, with no difference after DC101 or FUS alone (**Figure 3.2E**). These results indicate that although DC101 and FUS individually do not tighten the distribution of Gadovist around the mean, combining them likely does.

Next, we compared the kurtosis of the model drug distributions between $DC101^{-}/FUS^{-}$ and the other three treatment conditions. Kurtosis reflects the size of the distribution's tails, effectively another metric of distribution dispersion about the mean. After injecting Gadovist,

DC101$^-$/FUS$^+$ and DC101$^+$/FUS$^-$ had no effect on its distribution's kurtosis (**Figure 3.2F**). However, DC101$^+$/FUS$^+$ did result in a significant ~70% decrease in kurtosis (**Figure 3.2F**). This provides an additional statistical measure which underscores VN's homogenizing effect on small molecule distribution throughout 4T1 tumors.

3.3.3 Vascular Normalization Augments Total FUS-Mediated Model Biologic Drug Delivery

We then investigated whether VN and FUS (DC101$^+$/FUS$^+$) could augment the delivery of a larger model biologic drug, Gadospin-D, when compared to DC101 alone (DC101$^+$/FUS$^-$) or FUS alone (DC101$^-$/FUS$^+$). While this contrast agent has a lower molecular weight (17 kDa) than a monoclonal antibody (~150 kDa), its hydrodynamic diameter of ~5 nm approximates that of monoclonal antibodies (~5-6 nm) [151]. We first depicted Gadospin-D delivery with a map of a representative sample in each experimental condition (**Figure 3.3A**), with DC101$^+$/FUS$^+$ showing the greatest qualitative delivery improvement. Although Gadospin-D delivery over time (**Figure 3.3B**) and concentration at the final scan time point (**Figure 3.3C**) did not indicate differences across treatment conditions, the AUC exposure metric corroborated our qualitative findings. DC101$^+$/FUS$^+$ increased Gadospin-D exposure, including a 50% increase over the control condition (**Figure 3.3D**). Thus, FUS and VN do cooperate to synergistically improve biologic-sized model drug delivery.

We then evaluated differences in spatial distribution of Gadospin-D with VN and/or FUS using the same coefficient of variation and kurtosis metrics. Assessing the COV of the Gadospin-D distribution, we saw no change compared to the VN$^-$/FUS$^-$ mice. Similarly, we observed no change in the kurtosis of the Gadospin-D distribution compared to the DC101$^-$/FUS$^-$ treatment condition. This indicates that DC101$^+$/FUS$^+$ does not impact the Gadospin-D concentration distribution around the mean, unlike our Gadovist delivery findings.

3.3.4 Refining FUS Parameters to Maximize Gadospin-D Delivery Impact of DC101

After observing different effects of DC101 and FUS on the delivery of both model drugs, we decided to further compare FUS delivery enhancement between Gadovist and Gadospin-D. Doing so, we found that when mice were pre-treated with IgG control antibody, the ratio of final Gadovist concentration in FUS-treated mice to those not treated with FUS was lower for Gadospin-D than for Gadovist (**Figure 3.4A**). This was also true for the ratio of Gadovist and Gadospin-D exposure (**Figure 3.4C**). However, for mice pre-treated with DC101, there was no difference in ratio of final drug concentration (**Figure 3.4B**) or in ratio of drug exposure (**Figure 3.4D**). Since FUS is known to enhance biologic-sized delivery in tumors, we decided to explore a wider set of FUS parameters to maximize intratumoral Gadospin-D concentration.

We then decided to vary the density of the treatment scan and the peak-negative pressure (PNP), or intensity, of the FUS—modulating both of these parameters is known to impact FUS-mediated drug delivery. Following the framework from the above studies, we acquired time-course data for Gadospin-D accumulation following DC101 or IgG treatment and/or FUS sonication. We then calculated AUC exposure measures for each condition and evaluated the capacity for FUS to augment delivery—we therefore took the ratio of the $DC101^{+}/FUS^{+}$ to $DC101^{+}/FUS^{-}$ treatment and the $DC101^{-}/FUS^{+}$ to $DC101^{-}/FUS^{-}$. With a higher PNP and lower treatment density, the parameters we utilized for the above studies, we observed the ability for FUS to enhance delivery increase with the addition of DC101 (**Figure 4A**)—this was also the case for a lower PNP and a higher density (**Figure 4D**). However, this was not the case for the treatment conditions of dense treatment and high PNP (**Figure 4B**), or for sparse treatment and low PNP (**Figure 4C**). These findings highlight that the capacity for DC101 to enhance large model drug delivery only applies to a subset of FUS parameters.

3.4 Discussion

3.4.1 Rationale for Therapeutic Combinations

Building upon FUS research from our research group and VN work from others, we establish synergistic potential for both technologies to improve drug delivery to solid tumors. After characterizing the vascular effects of DC101, a VEGFR2 inhibitor, we exploit VN to enhance FUS's drug delivery capacity in a solid tumor model. Although DC101 alone only affects small model drug accumulation, it slightly boosts FUS's propensity to enhance delivery of small-molecule Gadovist and, to a much greater degree, delivery of large-molecule Gadospin. Not only does DC101 augment intratumoral drug concentration, it also improves FUS's capacity to homogenize delivery throughout the tumor. Given the limitations of each individual therapy, we rationally combine FUS with VN for the first time in a published manuscript. This work lays the groundwork for increasing delivery of large-molecule therapeutics in solid tumors.

3.4.2 DC101 Impacts 4T1 Vessel Form and Physiology

In this work we offer a unique set of findings pertaining to DC101's effects on vessel form and function in 4T1 tumors. 10 mg/kg dosing of DC101 yielded smaller, less dense tumor blood vessels via immunofluorescent imaging. These effects align with previous studies of VN in this tumor model. CEUS imaging uncovered a two-fold higher perfused fraction in normalized tumors, suggesting that the remaining vessels function better despite being less numerous. The volumetric blood flow within tumors also decreases slightly within DC101-treated tumors, a possible effect of vessels returning to a more capillary-like physiology under DC101 treatment.

3.4.3 MRI Techniques for Quantifying Model Drug Delivery

T1-weighted MRI is often used to quantify blood-brain barrier disruption with FUS in the brain [136], [152], but quantitative T1-mapping is almost always used to detect

pathologies or malignancies [153], [154], [155], [156], not to assess drug delivery. In rare circumstances, T1-mapping has been used to answer questions of model drug delivery within cancer-like brain pathologies like cerebral cavernous malformations or to assess glymphatic drainage into cervical lymph nodes [157], but not in extracranial tumor applications. This is due to the challenges of T1 signal to noise ratio in tumors, poor spatial resolution in many preclinical MRI magnets, and the difficulty in integrating drug delivery systems like FUS with MRI equipment. In this work, we overcome these challenges to successfully quantify spatiotemporal delivery of contrast agents with MRI T1-mapping, adding to the novelty of this work.

3.4.4 DC101 Augments Model Drug Delivery Enhancement After FUS in a Size-Dependent Manner

In addition to the effects that DC101 imparts on vessels and the known effects of FUS on drug delivery, these two interventions interact to boost model drug delivery in the 4T1 tumor model. Using this drug analog, Gadovist, we observe that although FUS can enhance delivery exposure to about 30% above baseline, VN only improves upon this delivery by about 20%. Conversely, using a biologic-sized drug analog, Gadospin D, we observe that neither VN nor FUS augments Gadospin-D exposure within tumors, while adding VN to FUS nearly doubles its delivery to FUS alone. Our findings that DC101 augments smaller drugs' accumulation more than larger drugs corroborates other groups' work, which has demonstrated similar size-dependent effects [158]. Combining DC101 and FUS highlights that FUS drives drug delivery into solid tumors in a manner dependent on the drug's size. Despite being lauded as a technology capable of augmenting biologic delivery in the brain and other tumors, FUS seems incapable of doing so in this solid tumor model. However, treatment of mice with DC101 prior to sonication rescues the drug delivery capacity of FUS for large, biologic-sized molecules.

VN's ability to improve FUS-mediated drug delivery may result from one or several biological phenomena. First, the reduction in tumor vessel size after VN [141], [159] may increase the interactions of sonicated MBs with the vasculature, allowing more vessel perturbation and model drug delivery where the tumor is sonicated. Second, the increase in tumor area perfused by functional vessels [89], [160], [161] underscores an increase in functional vessels in the sonicated region of the tumor, expanding the potential surface area for mass transfer thus increasing the amount of drug delivery. Finally, VN is known to decrease the interstitial fluid pressure within tumors [87], [162], [163], [164], [165], a barrier to particle transport via convective flow which may primarily drive large molecule delivery. Drug delivery with FUS may hinge on convective transport, as larger molecules depend more on convective flow than smaller molecules, which depend more on diffusion. Therefore, DC101 pretreatment may increase the potential for larger molecules to be transported into the tumor parenchyma during FUS sonication. Although detangling these mutually inclusive theories is challenging, they likely contribute to the size-dependent effects of DC101 on drug delivery enhancement with FUS.

3.4.5 DC101 Improves Intratumoral Model Drug Distribution in a Size-Dependent Manner

In addition to an increased quantity of biologic-sized model drug delivered with FUS after DC101 treatment, we also observed size-dependent shifts in model drug distribution. Treating mice with DC101 before FUS treatment yields a much higher reduction in coefficient in variation and kurtosis of the Gadovist concentration distribution than that of Gadospin-D. This shows that the distribution of all Gadovist concentrations within the tumor is much more tightly clustered around the mean and that there are fewer extreme low and high concentrations throughout the tumor. In other words, Gadovist is being delivered at a more homogenous range of concentrations throughout the tumor when mice are treated first with DC101. Tumors often

have inaccessible pockets where drugs cannot access due to drug delivery barriers enumerated above—DC101 likely decreases these high-concentration pockets. This likely permits greater access of drug to the tumor, which is beneficial when considering biologic drug applications. Many tumors contain regions of hypoxia and/or irregular blood flow where drugs may not be able to penetrate the parenchyma; these are regions where the biologic is least likely to be effective. We anticipate that reducing these regions is a net benefit for drug delivery in tumors.

3.4.6 FUS Parameters May be Tuned for Synergistic Delivery with DC101

After demonstrating that FUS and DC101 failed to increase Gadospin-D delivery but their combination significantly boosted delivery, we aimed to better understand which FUS parameters underly this synergy. Our initial sparse-scan treatment at a higher FUS PNP yielded synergy between DC101 and FUS (**Figure 4.5A**). The PNP that we used, 1 MPa, is much higher than that which is typical for FUS drug delivery to the brain. Although this may damage some tumor vasculature at the center of the FUS sonication focus, we expect that a significant share of the tumor is treated at a much lower PNP immediately outside these treatment points. We also anticipate that DC101 treatment may prevent FUS-related vessel damage, as VEGFR2 blockade has been shown to increase the presence of key vascular support cells like pericytes around vessels [139].

To probe the FUS parameter space, we adjusted the FUS PNP and the scan density, as these were variables of question following our first studies. When we applied FUS at 0.7 MPa, a lower intensity, and treater with a denser scan, we observed similar synergy between DC101 and FUS (**Figure 4.5D**). We expected this result, as it affirmed our hypothesis that treating a larger share of the tumor with a lower PNP would improve delivery. Conversely, treating with a higher PNP and a denser scan yielded no benefit from DC101—we expect that this parameter combination indeed damaged the tumor vasculature. On the other hand, we also saw no DC101 benefit when treating with a lower PNP and a sparser scan. This may be due to the existence of

a treatment threshold—while employing a lower PNP and a sparser treatment scan, only a small share of the tumor may have been treated, lowering the utility of DC101. Therefore, it is essential to balance FUS PNP and treatment point density to realize drug delivery enhancement with DC101, at least when it comes to biologic-sized drugs.

3.5 CONCLUSION

The increased development of large-molecule therapeutics combined with the simultaneous poor delivery of large molecules to solid tumors necessitates novel methods to augment drug delivery and guarantee these nascent therapeutics' efficacy. To advance delivery methods in this space, we developed an mFUS-based delivery paradigm that leverages vascular changes following anti-angiogenic therapy to augment local drug delivery in solid tumors. After confirming that DC101, an anti-angiogenic drug, elicits expected effects on tumor vessels, making them less numerous but more functional, we employed quantitative T1-mapping MRI to track the delivery of two differently sized model drugs post-FUS and DC101 therapy. We find that DC101 + mFUS improves both the delivery and the dispersion of a chemotherapy-sized model drug, Gadovist, and that DC101 + mFUS synergistically enhances the delivery of an antibody fragment-sized model drug, Gadospin-D. After observing this combinatorial effect with Gadospin-D, we modulate the mFUS parameters of peak-negative pressure and treatment point density, finding that the DC101 + mFUS delivery benefit requires these two parameters to be carefully controlled. To our knowledge, these studies are the first to use T1-mapping MRI to quantify drug delivery in an extracranial tumor and the first to combine vascular normalization with focused ultrasound, permitting the field to move forward with novel insights into how mFUS delivery effects can be amplified using vascular normalization.

3.6 Materials and Methods

3.6.1 Cell and Animal Maintenance

The 4T1 cell line was purchased from ATCC. 4T1 cells were maintained in 1X RPMI 1640 + L-Glutamine (Gibco #11875-093) supplemented with 10% Fetal Bovine Serum (FBS, Gibco #16000-044) at 37°C and 5% CO2. Thawed cells were maintained in logarithmic growth phase for all experiments, did not exceed 12 passages from the time of purchase, and tested negative for mycoplasma prior to freezing.

All animal experiments adhered to ethical guidelines and regulations approved by the University of Virginia Animal Care and Use Committee. The animals were housed in accordance with standard laboratory conditions, maintaining a temperature of 22°C and a 12-hour light/12-hour dark cycle and supplied food ad libitum. 7-10 week-old female BALB/c mice were purchased from Jackson Laboratories (Jax #000651) and acclimated for at least 48 hours in our animals facilities. To prepare the animals for inoculations, they were anesthetized with an intraperitoneal injection of ketamine (50 mg/kg Zoetis) and dexdomitor (0.25 mg/kg Pfizer). Their right flanks were shaved and 4x105 4T1 cells were subcutaneously injected in 100 µL 1X PBS (Gibco #10010-023) with a 25G x 1 ½ inch needle (BD PrecisionGlide Needle #305127) into the right flank of the mice, allowed to rest for 30 minutes, and injected intraperitoneally with Antisedan for anesthesia reversal and recovery. Tumor outgrowth was assessed with digital calipers, with tumor volume = (length x width2/2). Seven days following inoculation, mice were randomly placed in experimental groups while matching the starting tumor mean volume and minimizing intragroup variation.

3.6.2 VEGFR2 Blockade

To induce vascular normalization, mice were injected with 10 mg/kg DC101 (DC101 #BE0060 BioXCell) or appropriate IgG antibody control (rat IgG1 HRPN #BE0088 BioXCell)

diluted in sterile 1X PBS (Gibco #10010-023). DC101 and IgG were prepared the day of injections, and the 10 mg/kg calculation was determined at the day 7 size matching and continued throughout the duration of the experiment. Mice were interperitoneally injected with 100 µL of diluted DC101 or IgG at days 7, 10, and 13 post-inoculation.

3.6.3 Immunofluorescent Staining and Sample Imaging

Mice for terminal studies were euthanized with 50 µL of Euthasol injected interperitoneally. Tumors were removed and placed in 10 mL Zinc Formalin fixative diluted to 10% in deionized water for 48 hours, then placed in 60% sucrose dissolved in 1 X PBS for about 1 week. Tumors were then placed in cassettes filled with optimal cutting medium, frozen in 100% ethanol cooled with dry ice, and stored at -80°C until cryosectioning.

Samples were cryosectioned into 15 um sections, then stained with anti-CD31 antibody and mounted with DAPI mounting medium. Samples were imaged at 10X magnification on a Zeiss 880 Confocal Microscope, for which 5-7 representative images were acquired. Images were analyzed with an in-house ImageJ script which used the threshold function to count and measure CD31+ vessels in 4T1 tumors.

3.6.4 MRI Acquisition

Data for T1 maps were acquired with a 9.4T Bruker small bore MRI. A set of interleaved multi-slice 2D spin echo (SE) images were taken at varied repetition times (TR) to generate a saturation recovery curve. The slice gap was set to 100% of the slice thickness to eliminate cross talk. 2 sets of 7 images, a total of 14 scans, were acquired prior to FUS and contrast agent administration to obtain saturation recovery curves with a satisfactory dynamic range. The two sets of image series were offset by the slice gap in the slice select plane to ensure 3D coverage of the brain. The parameters for these scans were: TR=790, 1040, 1350, 1750, 2300, 3215, and 7000 ms, TE=6.71 ms, slice thickness=0.6 mm, slice gap=0.6 mm, FOV=35 x 35

mm, matrix size=200 x 200, rare factor=10, and R= 0.175 x 0.175 x 0.6 mm3. After FUS and contrast agent administration, 10 SE images were acquired with identical parameters except at a fixed TR=1040 ms. The acquisitions alternated between slice package orientations resulting in 7 images at each slice profile geometry. Time per acquisition was 1 minute and 19 seconds.

3.6.5 Data Processing

A saturation recovery approach was utilized to calculate M_0 and all T1 values (pre and post-contrast) on a voxel-by-voxel basis by fitting the data to the signal equation:

$$|S| = M_0\left(1 - e^{\frac{-TR}{T_1}}\right)e^{\frac{-TE}{T_2}} \qquad \text{Eqn [1]}$$

In equation 1, $|S|$ is the magnitude of the signal within the voxel, M_0 is the product of the thermal equilibrium magnetization and coil sensitivity, TR is the repetition time (ms), T1 is the spin-lattice relaxation (ms), TE is the echo time (ms), and T2 is the spin-spin relaxation (ms). The echo time exponential is assumed to be 1 due to TE<<T2, resulting in the final form seen in equation 2.

$$|S| = M_0\left(1 - e^{\frac{-TR}{T_1}}\right) \qquad \text{Eqn [2]}$$

A custom-written MATLAB script fit the signal magnitude data on a voxel-by-voxel basis to equation 2. Each fitting procedure simultaneously fit the data to 6 functions: function 1 incorporated the 7 pre-contrast variable TR scans, while functions 2-6 incorporated the singular scan at a fixed TR but different time points. The fits were constrained to having the same M_0 value but allowed different T1 values. Pre-contrast and post-contrast T1 values were then used to calculate the contrast agent concentration on a voxel-by-voxel basis at each time point using equation 3.

$$\frac{1}{T_{1\_Post}} = \frac{1}{T_{1\_Pre}} + r_1 C_1 \quad \text{Eqn [3]}$$

In equation 3, T_{1_Post} is the post-contrast value at a particular time point (ms), T_{1_Pre} is the pre-contrast T1 value (ms), r_1 is the contrast agent relaxivity (L/mmol/ms), and C1 is the contrast agent concentration (mM). At the conclusion of this process, concentration values for slice package 1 existed for time points (minutes): 1.32, 3.95, 6.58, 9.22, and 11.85, while concentration values for slice package 2 existed for time points (minutes): 2.63, 5.27, 7.90, 10.53, and 13.17. To obtain 3D coverage at each time point, concentration data was calculated at the missing time points by linearly interpolating between the acquired points. This required an assumption of 0 concentration at minute 0 for slice package 2. The 13.17-minute time point was not used because it required that data be extrapolated past minute 11.85 for slice package 1. A second custom MATLAB script was used to calculate average concentrations with manually drawn regions of interest (ROIs) on the concentration maps which corresponded to the area of the tumor.

3.6.6 Tumor Sonication with FUS

Tumors were sonicated with the RK-300 small bore FUS device (FUS Instruments, Toronto, CA). Mice were prepared by depilating the area around their tumor before being placed with their right side down and coupled to the transducer using degassed ultrasound gel. Immediately prior to sonication, clinical-grade Optison™ (GE HealthCare) microbubbles were intravenously administered as a bolus of 2X10^5 microbubbles per gram of body weight, with an average body weight of ~20 g. The distribution of microbubble diameter and microbubble concentration were evaluated using a (Multisizer 3; Beckman Coulter, Fullerton, California) before FUS treatment. FUS was applied using a 1.1 MHz single-element transducer with a 10 ms burst length over a 2000 ms period. A total of 40 sonications were administered during a 2-minute duration. For most experiments in this Aim, a PNP of 0.7 MPa was employed for the duration of treatment, except when specified that a PNP of 1.0 MPa was used.

3.6.7 Contrast Agent Injections

MultiHance® (gadobenate dimeglumine; Bracco), the smaller drug analog, and GadoSpin D™ (dendritic Gd-chelate; Viscover), the biologic drug analog, were both intravenously administered as a bolus injection of 0.2 mM/kg body weight diluted in saline, with an average body weight of ~0.020 kg. Contrast agent was injected immediately prior to MRI acquisition for experimental groups excluding FUS and immediately following sonication and prior to MRI acquisition for experimental groups including FUS.

3.6.7 Statistical Analyses

All results are reported as the mean ± the standard error of the mean (SEM). Statistical significance was assessed at $p < 0.05$ for all experiments and was calculated using GraphPad Prism 9 (San Diego, USA).

3.6 CHAPTER 3 FIGURES

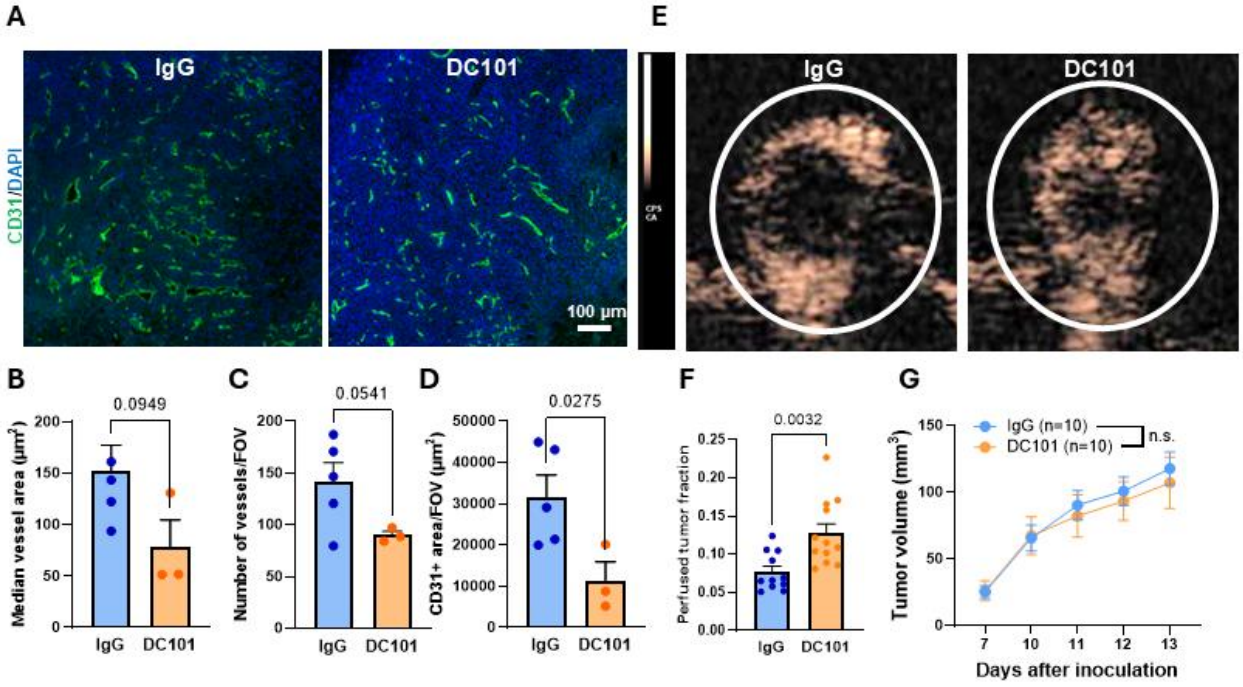

Figure 3.1. DC101 induces vascular normalization in 4T1 tumors. (A) Green CD31 vascular stain and blue DAPI nuclear staining of 4T1 tumors taken from mice treated with 10 mg/kg IgG or 10 mg/kg DC101. **(B)** DC101 induces a trending decrease in median tumor vessel cross-sectional area (Welch's t-test, p = 0.0949), **(C)** number of vessels per field of view (Welch's t-test, p = 0.0541), and **(D)** significantly decreases the CD31+ area within the tumor (Welch's t-test, p = 0.0275). CEUS imaging with infusion of 4E5 microbubble/g **(E)** demonstrates that **(F)** the fraction of the tumor perfused by vessels following DC101 treatment is nearly double that of control tumors (Welch's t-test, p = 0.0032). **(G)** DC101 does not affect 4T1 tumor growth within this time period (Two-way ANOVA with Geisser-Greenhouse correction, p = 0.7833).

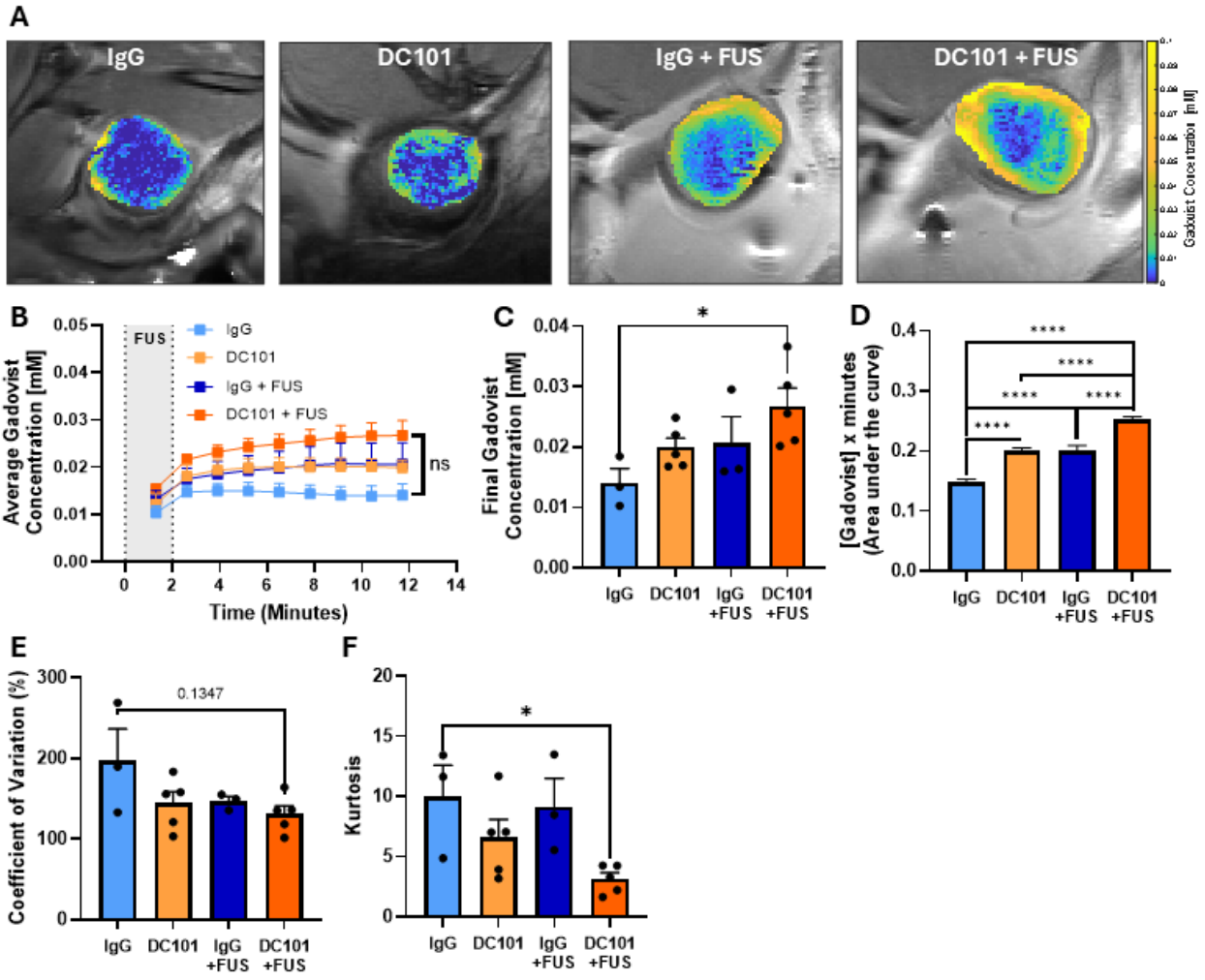

Figure 3.2. DC101 and FUS additively increase small molecule delivery. (A) Visualization of Gadovist deposition in 4T1 tumors in all four experimental groups. **(B)** There is no significant difference between the four treatment conditions on Gadovist concentration over time (Repeated measures two-way ANOVA with Geisser-Greenhouse correction, p = 0.12). **(C)** DC101+/FUS+ does afford a ~70% increase in average Gadovist concentration at the final imaging timepoint (Two-way ANOVA with Tukey post-hoc test, p = 0.0292), as well as **(D)** a significant increase in total Gadovist exposure as represented by the area under the concentration curves (Two-way ANOVA with Tukey post-hoc test, p < 0.0001). DC101+/FUS- and DC101-/FUS+ also increase Gadovist exposure by about 30%, each (Two-way ANOVA with Tukey post-hoc test, p < 0.0001, , p < 0.0001). In addition to an increase in Gadovist concentration, DC101+/FUS+ causes **(E)** a trending decrease in the Gadovist concentration distribution's coefficient of variation (Two-way ANOVA with Tukey post-hoc test, p = 0.1347) and **(F)** a significant decrease in the distribution's kurtosis (Two-way ANOVA with Tukey post-hoc test, p = 0.0315).

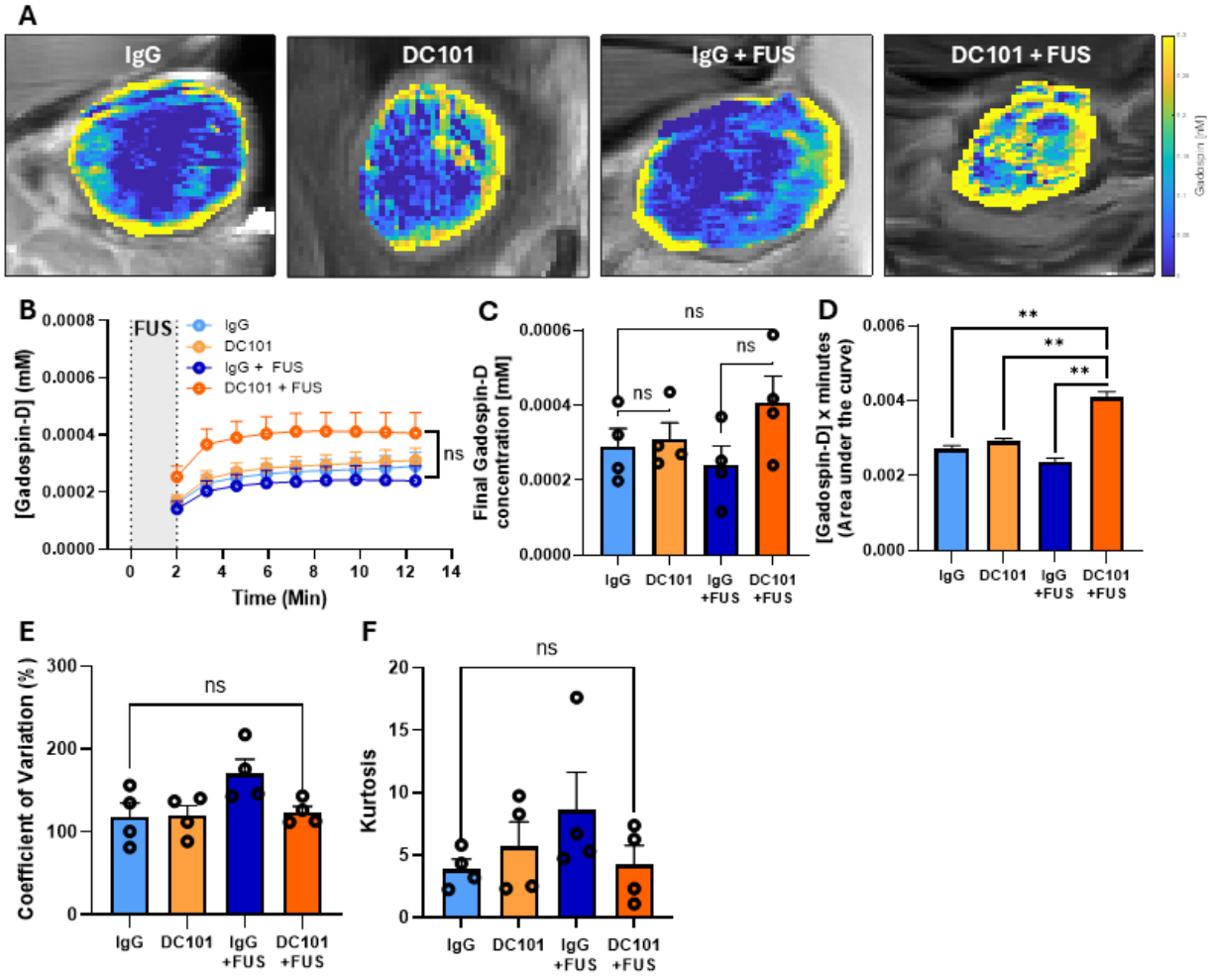

Figure 3.3. DC101 and FUS synergistically augment Gadospin-D delivery. (A) Visualization of Gadospin-D deposition in 4T1 tumors in all four experimental groups. **(B)** There is no significant difference between the four treatment conditions on Gadospin-D concentration over time (Repeated measures two-way ANOVA with Geisser-Greenhouse correction, $p = 0.104$). **(C)** DC101+/FUS+ does not significantly impact Gadospin-D concentration at the final imaging timepoint (Two-way ANOVA with Tukey post-hoc test, $p = 0.5503$), but it does **(D)** a significantly increase in total Gadospin-D exposure over time (One-way ANOVA with Tukey post-hoc test, $p < 0.0067$). However, DC101+/FUS- and DC101-/FUS+ do not increase Gadospin-D exposure (Two-way ANOVA with Tukey post-hoc test, $p = 0.3590$, $p = 0.3996$). DC101+/FUS+ does not affect **(E)** Gadospin-D's concentration distribution's coefficient of variation (Two-way ANOVA with Tukey post-hoc test, $p = 0.9941$) or **(F)** the distribution's kurtosis (Two-way ANOVA with Tukey post-hoc test, $p = 0.9993$).

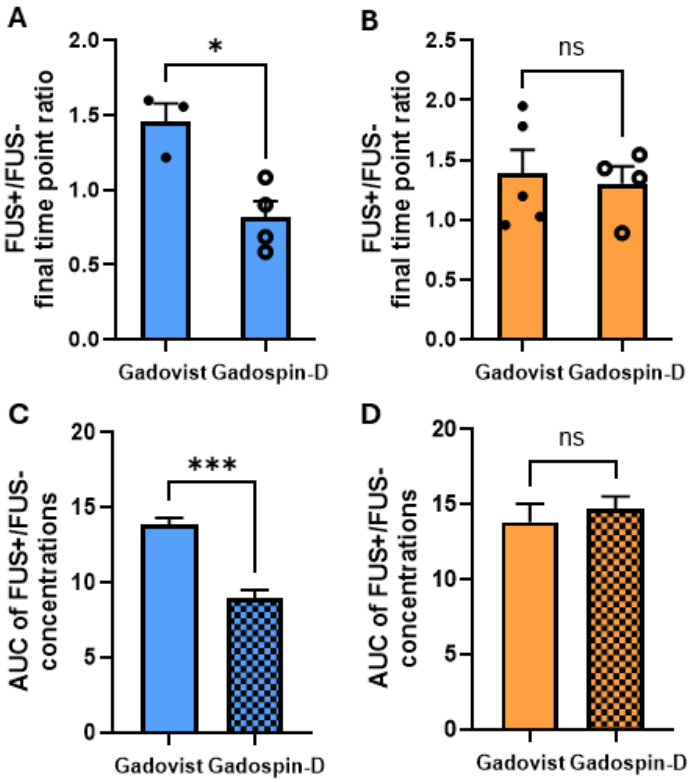

Figure 3.4. FUS and DC101 interact differently to deliver differently sized molecules. Taking the ratio of FUS+/FUS- treatment at the final imaging timepoint, we find that **(A)** Gadovist concentration is amplified more than Gadospin-D on an IgG background (Welch's t-test, p = 0.0130), a difference not present on **(B)** a DC101 background (Welch's t-test, p = 0.7588). The same trends hold when an area under the curve analysis is applied to the FUS+/FUS- concentration ratio over time. On an IgG background, **(C)** Gadospin-D exposure is smaller when compared to that of Gadovist (Welch's t-test, p = 0.0007), but **(D)** there is no difference between the two on a DC101 background (Welch's t-test, p = 0.5658).

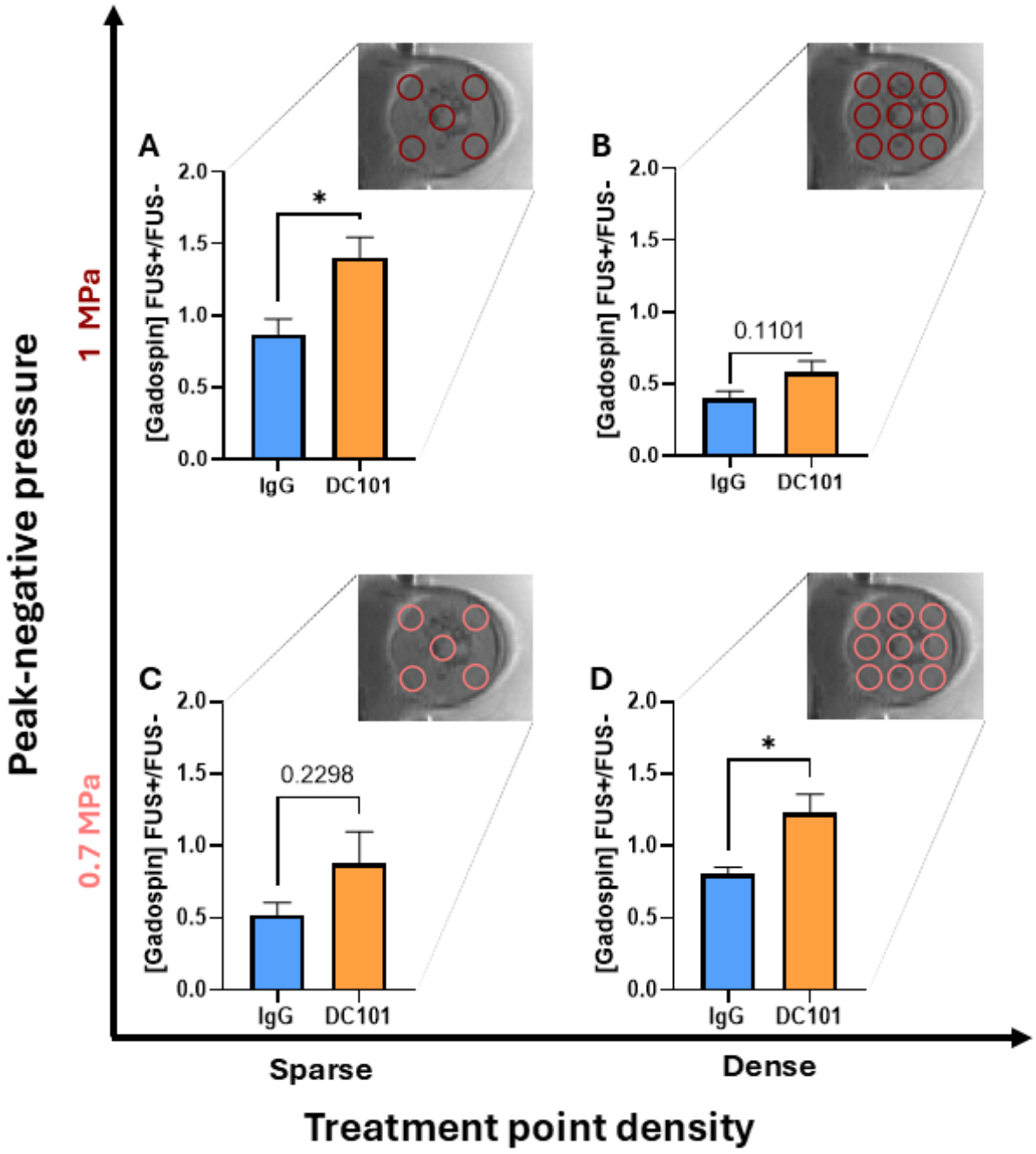

Figure 3.5. DC101 boosts FUS-mediated Gadospin-D as a function of FUS parameters. Modulating the FUS parameters of peak-negative pressure (PNP) and treatment point density, we find that **(A)** DC101 improves FUS delivery as compared to FUS alone when the PNP is higher and the treatment density is lower (Welch's t-test, p = 0.0249) or when **(D)** the PNP is lower and the treatment density is higher (Welch's t-test, p = 0.0419). DC101 cannot augment FUS-mediated delivery when **(B)** FUS PNP is high and treatment density is higher (Welch's t-test, p = 0.110) or when **(C)** FUS PNP is low and treatment density is lower (Welch's t-test, p = 0.230). T1-map outsets with treatment points reflect typical sparse and dense treatment schematics, with each point representing a -6dB FUS focus.

CHAPTER 4: VEGFR2 BLOCKADE CONVERTS THERMALLY ABLATIVE FOCUSED ULTRASOUND INTO A POTENT DRIVER OF T CELL-DEPENDENT ANTI-TUMOR IMMUNITY

Mark R. Schwartz[1], Nareen Z. Anwar[1], Lydia E. Kitelinger[2], Timothy N.J. Bullock[2], Matthew R. DeWitt[1], Richard J. Price[1,3]

1. Department of Biomedical Engineering, University of Virginia, Charlottesville, VA

2. Department of Pathology, University of Virginia, Charlottesville, VA

3. Department of Radiology and Medical Imaging, University of Virginia, Charlottesville, VA

4.1 ABSTRACT

BACKGROUND: Many patients with solid tumor malignancies remain refractory to immunotherapy. Preclinical and clinical studies indicate that thermal tumor damage can initiate anti-tumor immune responses. Separately, vascular endothelial growth factor (VEGF) blockade has shown to immunologically prime tumors for greater immunotherapy responsiveness. We thus engineered a treatment paradigm including thermally ablative focused ultrasound (tFUS), DC101, which can block VEGF signal transduction, and anti-PD1, a common immunotherapy used in the clinic

METHODS: We developed a non-invasive FUS partial thermal ablation regimen in combination with DC101 and anti-PD1, the combinations of which were used to treat syngeneic murine solid tumors including EMT6 (triple-negative breast cancer), 4T1 (triple-negative breast cancer), and YUMMER1.7 (melanoma). In addition to establishing this treatment regimen, we assessed circulating and intratumoral immune composition with spectral flow cytometry and performed systemic T cell depletion to evaluate immune-dependent response mechanisms.

RESULTS: After confirming the immune effects of DC101 with flow cytometry, we employed a partial thermally ablative FUS regimen to tumors in combination with these two drugs in a range of preclinical solid tumor models. We then tested whether the effects of our treatment combinations were durable and adaptive with rechallenge and T cell depletion experiments. Particularly with the favorable immunomodulation provided by neoadjuvant DC101, its combination with tFUS was sufficient to control primary tumor growth and drive long-term, T cell-dependent immunity. These effects were further enhanced by the addition of anti-PD1.

CONCLUSIONS: tFUS combined with immunomodulatory drugs such as VEGFR2 blockade and immunotherapies such as anti-PD1 shows promise as a novel combination therapy capable of curbing solid tumor growth and evoking potent adaptive immunity.

4.2 INTRODUCTION

Several energy deposition modalities, including laser interstitial thermal therapy (LITT), microwave, radiofrequency, cryoablation, electroporation, and thermal ablation with focused ultrasound (tFUS) [31], are commonly deployed to debulk solid tumors in the clinic. While these non- or minimally-invasive ablative techniques are typically leveraged to elicit local cancer cell death, modulation of tumor immune landscape is also known to occur in many instances [32], [33], [34], [35], [36], [37], [38], [39], [40], [41], [42], [43], [44], [45]. For example, while tFUS is typically used to elicit coagulative necrosis [46], debulk neoplasms [47], and temporarily control primary tumor growth [48], [49], [50], it also induces damage-associated molecular pattern expression [51], [52], liberates tumor antigen [53], and drives several other responses that may be associated with anti-tumor immunity [4], [5], [6]. Because, for many cancer indications (e.g. breast cancer and melanoma), it is metastatic, not primary, tumor growth and dissemination that causes patient mortality, it is intriguing to consider how these immunological responses to tFUS could be leveraged to drive systemic anti-tumor immunity against metastatic deposits. Yet, there is little evidence that tFUS as a monotherapy can robustly and reproducibly control metastatic disease, despite its ability to modulate tumor immune landscape [53], [55], [57], [58], [59], [60]. Here, we hypothesize that local responses to tFUS could be leveraged to immunologically control distal metastatic disease via logical combinations with standard of care therapies.

To this end, one potential class of candidate drugs for combination with tFUS is angiogenesis inhibitors, which can reverse immunosuppression in the tumor microenvironment, primarily through modulation of tumor vessel properties [89], [91], [92], [166], [167]. Tumor blood vessel dysfunction is a primary factor in patients' unresponsiveness to anti-cancer drugs, including immunotherapy. This aberrance presents both at the macro-level, with a disorganized vascular network [168] that insufficiently perfuses tumor tissue [169], and at the micro-level, with an anergic response to inflammatory stimulus and poor capacity for leukocyte extravasation

[76], [95], [170], [171]. Low doses of angiogenesis inhibitors have proven effective in temporarily reversing undesirable tumor vessel properties in a process known as vascular normalization (VN)—this includes improving blood vessel perfusion [89], intratumoral hypoxia [90], [91], adhesion molecule expression on vessel lumens [92], [93], and T cell extravasation into tumors [94], [95]. Although this intervention alone may not substantially impact bulk tumor growth, its combination with immunotherapy (ITX) such as anti-cancer vaccines [97], [98], [99], adoptive immune cell transfer [100], [101], [102], and ICIs [103], [104], [105], [106], [107], [108], [109], [110], [111] has increased ITX effectiveness in controlling tumor growth and eliciting systemic anti-tumor responses. This is thought to be due to subsequent upregulation of cell adhesion molecules on tumor blood vessels, which facilitate immune cell extravasation into tumors, and increased oxygenation within tumors, which can improve T cell function. Since tFUS is also known to elicit anti-tumor immune responses, we expect that the immunostimulatory effects of tFUS to also be enhanced with VN.

Immune checkpoint inhibitors (ICIs) are yet another drug class that may be logically combined with tFUS. ICIs effectively treat cancer subtypes like lung [172], bladder [173], kidney [174], colorectal [175], prostate [176], and early-stage skin cancers [177]. This drug class acts by inhibiting cell-cell signaling that typically hinders effector T cell activity, permitting cytotoxic T cells to more effectively kill cancer cells. However, sizeable subsets of triple-negative breast cancer [178], metastatic melanoma [177], and pancreatic cancer [179] patients are refractory to ICIs. This is due to intratumoral immunosuppression, poorly functioning tumor vessels, and low antigenicity. Combining tFUS with ICI may overcome some of these factors, particularly by temporarily abolishing immunosuppressive intratumoral cells and releasing tumor antigen.

In these studies, we tested whether these three therapeutic interventions—tFUS, VN, and ICI—can be combined to eradicate solid tumors and generate systemic anti-tumor immunity to resist subsequent rechallenge. In these studies, we used a syngeneic murine triple-negative

breast cancer (TNBC) model, EMT6, and a syngeneic murine melanoma model, YUMMER1.7, as a secondary model. After confirming the ability for DC101, a vascular endothelial growth factor receptor 2 (VEGFR2) inhibitor, to modulate tumor T cell infiltrate, we combined DC101—αPD1, a common ICI—and tFUS, finding varying cooperation in primary tumor control and eradication depending on the combination. Contralateral rechallenge, T cell depletion, and a second rechallenge in mice whose primary tumors were eradicated indicate that the long-term response depended on systemic adaptive immunity. Therefore, our findings demonstrate that VN and ICI, individually and together, can potentiate durable, systemic anti-tumor immune responses induced by tFUS. The results suggest that combining tFUS with anti-angiogenic drugs and/or PD1 represents a clinically promising therapeutic strategy for treating metastatic disease.

4.3 RESULTS

4.3.1 PARTIAL THERMAL ABLATION OF EMT6 TUMORS TEMPORARILY CURBS GROWTH

We first developed a FUS application protocol that yields partial thermal ablation (tFUS) of solid tumors. We employed a FUS system with 4 therapeutic transducers and a central imaging transducer for treatment guidance (**Figure 4.1A, B**). tFUS was applied at 1.5-mm intervals in the X and Y directions, with treatment planes 2 mm apart. We confirmed that temperatures > 70°C were achieved using thermochromic gels treated with the same sonication parameters (**Figure 4.1C**), in addition to staining tumors with 2,3,5-Triphenyltetrazolium chloride (TTC), which reveals metabolically active cells (**Figure 4.1D**). The outer edges of the tumor stained red, the tFUS treated center stained white, and the periablative “transition” zone stained pink, indicating partial tFUS ablation was achieved.

We next tested how this tFUS application scheme affected EMT6 tumor growth. As assessed with tumor growth curves, tFUS application at 14 days post-inoculation (tumor volume = ~100 mm^3) was insufficient to control EMT6 tumor growth compared to a sham control (**Figure 4.2A**). Individual growth curves highlight several ablated tumors that experienced delayed outgrowth (**Figure 4.2B**). An “area under the curve” metric, which is a measure of integrated tumor burden, indeed yielded an ~2-fold decrease in tumor burden with tFUS (**Figure 4.2C**). However, tFUS improved neither animal survival (**Figure 4.2D**) nor tumor eradication rate (**Figure 4.2E**). Thus, this tFUS protocol yields modest and transient primary tumor control.

4.3.2 DC101 VEGFR2 Blockade Beneficially Modulates Intratumoral T Cell Composition

After establishing this tFUS partial ablation protocol, we next asked whether VEGF-R2 blockade could synergize with tFUS to drive T-cell dependent anti-tumor immunity. As a first step in addressing this question, we tested whether VEGF-R2 blockade beneficially remodels the immune landscape in EMT6 tumors. A VEGF-R2 blocking antibody (DC101) was administered intraperitoneally and EMT6 tumor growth was tracked beginning 7 days after inoculation (**Figure 4.3A**). A subset of tumors was harvested 14 days post-inoculation when tumors measured ~100 mm^3 and assessed for T cell representation by flow cytometry, with our gating strategy outlined in **Figure 4.S1**. The number and share of $CD8^+$ T cells in these tumors were unchanged by DC101 treatment (**Figure. 4.3B, C**). However, the number and share of $CD4^+Foxp3^+$ regulatory T cells (Treg) were decreased by ~3-fold and ~1.5-fold, respectively (**Figure 4.3D, E**). As a result, the CD8/Treg ratio, a useful predictor of improved clinical outcomes [180], [181], nearly doubled with DC101 treatment (**Figure 4.3F**). Additionally, about half of $CD8^+$ cells were $PD1^+$ following either IgG or DC101 treatment (**Figure 4.3G**). However, in the other subset of EMT6 tumors, DC101 treatment did not control tumor (Figure **4.3H, I**), improve integrated tumor burden (**Figure 4.3J**), extent animal survival (Figure 3K), or demonstrate eradication benefit (**Figure 4.3L**). Therefore, DC101 induces favorable immune changes within EMT6 tumors but fails to impact tumor growth or eradication.

4.3.3 DC101 Synergizes with Sparse tFUS to Control Tumors, Extend Survival, and Induce Anti-Tumor Immunity

After establishing that VEGF-R2 blockade remodels tumor immune landscape, we tested whether it synergizes with tFUS in the treatment of EMT6 tumors using the experimental timeline in **Figure 4.4A**. DC101 + tFUS significantly controlled EMT6 tumor growth when

compared to DC101 and IgG control groups (**Figure 4.4B, C**). At 2 weeks post-tFUS, the DC101 + tFUS-treated tumor volume was fully 5-fold lower than IgG control and 3.5-fold lower than tFUS monotherapy. Tumor control was reflected in the AUC metric as well, corresponding to 3.5-fold decrease in tumor burden for DC101 + tFUS compared to IgG control and a 2-fold decrease compared to tFUS (**Figure 4.4D**). The effect of this combination therapy was found to be synergistic in nature (**Figure 4.7A, B**). Survival was also extended significantly in the DC101 + tFUS group (**Figure 4.4E**). Additionally, 50% of tumors treated with DC101 + tFUS were entirely eradicated, an improvement from 17% of tumors eradicated by tFUS (**Figure 4.4F**). Neither the DC101 group nor the IgG group yielded tumor eradication (**Figure 4.4F**). Similar results were observed using the 4T1 tumor model, where observed a significant growth control benefit when treating 4T1 a trending decrease in volume of lung metastases 4 weeks post-inoculation (**Figure 4.S2**).

To then test whether DC101 + tFUS-treated mice with eradicated primary tumors harbored systemic immunity against EMT6 tumors post-eradication, we performed EMT6 rechallenges in the contralateral flank. Here, 83% of mice rejected the rechallenge (**Figure 4.4F**), suggesting that the presence of systemic immunity prevented secondary tumor growth. To verify that tumor rejection in these mice was T cell-dependent, we employed systemic αCD4 and αCD8 antibody depletion, followed by a second rechallenge. Three months after CD4/CD8 depletion, T cell reconstitution was complete (**Figure 4.4G-I**). EMT6 cells were again injected in the contralateral flank. Post-recovery, tumors were significantly larger than the rechallenge tumors that grew in the same mice pre-depletion (**Figure 4.4J**), indicating that the immunity conferred by the combination treatment was T cell dependent. After this time point, most tumors rechallenged post-reconstitution did regress, which is consistent with previous literature suggesting that tissue resident memory T cells in the skin and lungs are difficult to deplete with systemic αCD4 and αCD8 antibodies [182], [183], [184].

4.3.4 αPD1 Combined with tFUS Additively Controls Tumor Growth and Augments Anti-Tumor Immunity

After determining that neoadjuvant VEGF-R2 blockade converts tFUS into a potent driver of T cell-dependent anti-tumor immunity, we asked whether a conventional checkpoint inhibitor (αPD1) could elicit this same response. EMT6 tumors are known to be partially responsive to similar drugs [44][44][46]. We dosed EMT6-bearing mice with αPD1 (4 doses using a standard concentration and timing for mice) and applied tFUS on day 14 (**Figure 4.5A**). We observed a trending decrease (p=0.064) in tumor volume for the αPD1 + tFUS group when compared to IgG (**Figure 4.5B, C**) and no significant differences when compared to tFUS and PD1 monotherapies. The effect of this dual combination was found to be additive in nature (**Figure 4.7C, D**) The AUC metric did reveal an ~3-fold decrease in integrated tumor burden with αPD1 + tFUS compared to IgG control (**Figure 4.5D**), as well as a trending (p=0.12) survival advantage compared to IgG control (**Figure 4.5E**). Notably, this protocol was repeated in a second solid tumor model (YUMMER 1.7 melanoma). Similar results were observed in YUMMER1.7-bearing mice (**Figure 4.S3B-G**). ~55% of the mice treated with αPD1 + tFUS had their tumors eradicated (**Figure 4.5F**) as compared to only ~15% of αPD1-treated tumors eradicated.

To mirror the DC101 + tFUS experiment, mice with eradicated tumors were rechallenged contralaterally, with ~60% of rechallenges rejected (**Figure 4.5F**). After depleting CD4 and CD8 T cells and allowing circulating T cells to repopulate (**Figure 4.5G-I**), mice were again rechallenged contralaterally. Tumors grew faster post-reconstitution than they did pre-depletion (**Figure 4.5J**). Again, this suggests T cell memory dependency on the anti-tumor immune response generated in most of the tumor-eradicated mice.

4.3.6 DC101 and aPD1, Combined with tFUS, Robustly Control EMT6 Tumor Growth, Confer Survival Advantage, and Induce Anti-Tumor Immunity

DC101 and αPD1 were individually capable of improving the anti-tumor effects of tFUS, and anti-angiogenics like DC101 are known to enhance anti-tumor immunity induced by ICIs like αPD1. As such, we tested whether combining these three therapeutics would induce more potent tumor control than tFUS or DC101 + αPD1 alone. We administered 4 doses of DC101 and αPD1 and applied tFUS on day 14 (**Figure 4.6A**). The DC101 + aPD1 + tFUS-treatment yielded exceptional primary control, as evidenced by the tumor growth curves (**Figure 4.6B, C**) and integrated tumor burden through the AUC metric (**Figure 4.6D**). Specifically, the triple combination reduced AUC 5-fold compared to IgG control and 3-fold compared to tFUS, with a trending 3-fold decrease compared to DC101 + αPD1 (**Figure 4.6D**). The effect of this triple combination was found to be additive in nature (**Figure 4.7E, F**) The triple combination therapy also conferred significant survival benefits (**Figure 4.6E**). DC101 + αPD1 eradicated ~30% of the tumors, while DC101 + αPD1 + tFUS eradicated ~80% of the tumors, which constitutes a significant eradication benefit compared to IgG control and a trending ($p=0.057$) toward a benefit compared to tFUS (**Figure 4.6F**). We found the timing of this combination treatment regimen, as administering one dose of aPD1 pre-tFUS and 3 doses post-tFUS (**Figure 4.S4A**) did not elicit significant growth control (**Figure 4.S4B, C**) or decrease integrated tumor burden (**Figure 4.S4D**).

Similar to previous experiments, we contralaterally rechallenged the mice with eradicated tumors. All DC101 + αPD1 mice rejected their rechallenge, with ~75% of the DC101 + aPD1 + tFUS mice rejecting rechallenge (**Figure 4.6F**). Following CD4 and CD8 T cell depletion and reconstitution (**Figure 4.6G-I, K-L**), mice were contralaterally rechallenged again. Here, we observed faster tumor growth post-reconstitution than we did in the same mice before CD4/CD8

T cell depletion (**Figure 4.6J, M**), indicating the rechallenge rejection observed following primary tumor eradication was T cell dependent.

4.4 Discussion

4.4.1 Rationale for Therapeutic Combinations

In these studies, we aimed to develop a pharmacological strategy that converts tFUS into a non-invasive approach for generating T cell-dependent immunity against solid tumors. We first established a partial tFUS regimen that temporarily slowed tumor growth but did not enhance long-term animal outcomes. Seeking out logical combinations between tFUS and drugs with clinical counterparts, we leveraged the ability of VEGFR2 blockade to favorably immunomodulate solid tumors, demonstrating improvements in T cell infiltrate using DC101. Combining tFUS with DC101 yielded significant eradication and development of T cell-dependent anti-tumor immunity. Because many ICIs bolster anti-tumor immunity and most T cells in EMT6 tumors were $PD1^{+}$, we then combined tFUS with aPD1. This combination was moderately effective, eradicating many tumors and generating T cell-dependent anti-tumor immunity. Combining all three therapeutics eradicated nearly all primary tumors and, again, resulted in T cell-dependent anti-tumor immunity. The three constituent therapies employed in our studies are used separately in the clinic—we demonstrate that in combination, they produce more potent anti-tumor responses than as monotherapies. In particular, VEGFR2 blockade potentiated the effects of tFUS without efficacy as a monotherapy, demonstrating distinct promise for anti-angiogenic therapies as tFUS-enhancing drugs. These findings suggest that VEGFR2 blockade may be leveraged to improve the efficacy of tFUS in clinical settings, both with and without PD1 blockade.

4.4.2 The Utility of tFUS as an Immunotherapy

In these studies, we leverage immunomodulatory drugs to enhance the immune effects of heat-related damage induced by tFUS. Other ablative FUS modalities have been successfully combined with drug administration to drive systemic anti-tumor immunity, and it is informative to

consider our results in light of these other studies. One such modality is histotripsy, which mechanically fractionates tumor tissue with minimal heating and has been reported to be more effective than tFUS in enhancing ICB in certain preclinical cancer models [185]. Histotripsy activates dendritic cells and promotes tumor antigen acquisition in similar tumor models [186]—the lack of tissue heating following histotripsy may preserve more antigen intact than tFUS regimens that ablate the entire tumor. While these studies highlight the promise of histotripsy as an immunomodulatory ablation modality, our data, in combination with other studies [54], [55], [56], [57], indicate that properly applied tFUS still has significant promise for augmenting immunotherapy. tFUS releases DAMPs [51], [52], [53], and partial tFUS generates temperature transition zones where antigen may be effectively released without denaturing. Additionally, partial tFUS likely preserves more tumor parenchyma and vasculature for T cell homing. Together, the choice to utilize partial ablation over complete ablation may rescue tFUS's capacity to generate lasting anti-tumor immune responses.

Several published studies combine tFUS with secondary therapies to induce immune-mediated control [54], [55], [56], [57]. However, key differences separate these studies' approaches and findings from our own, with the most significant difference being that our study is the first to test tFUS in combination with VEGFR2 blockade. Yet another difference is tFUS ablation fraction, estimated at 25% in our study (**Figure 4.1E**). In a previous study, we found that treating a larger ablation fraction per tumor in a 4T1 model induced moderate growth control [54]—this more aggressive ablation regimen was less effective at controlling tumor growth than partial ablation in the EMT6 model. In another case, partial thermal ablation moderately controlled tumor growth [56], corroborating our findings in a $Her2^{+}$ tumor model. However, yet another group found that treatment with a greater number of treatment points controlled CT26 tumors well [57]. None of these studies inquire about the effect of partial versus complete ablation on growth control. However, one such study suggests that partial ablation

may promote dendritic cell infiltration and maturation better than more complete ablation [187]. Differences in ablation regimen and tumor model notwithstanding, the same groups observe similar results when combining various tFUS regimens with immunotherapies: tFUS combined with gemcitabine, a myeloablative drug; CpG, an innate immune agonist, plus aPD1; and aCTLA-4; can induce both growth control in primary tumors due to a systemic anti-tumor immune response. Across these studies, tFUS likely catalyzes DAMP and antigen release and ablates a substantial fraction of cancer and myeloid cells. Without a classical immunotherapy like aPD1, tFUS cannot sufficiently increase effector T cell activity. Our findings not only corroborate the efficacy of partial tFUS combined with immunotherapy but go further in realizing synergistic benefits between tFUS and another drug which is not typically classified as an immunotherapy: DC101. Without DC101, the immunostimulatory spark of tFUS does not catch due to dysfunctional blood vessels, lymphatics, and T cell infiltration. Ultimately, our findings align with recent studies demonstrating utility of tFUS as a potent component of combination immunotherapies [54], [55], [56], [57].

4.4.3 aPD1 and tFUS Additively Induce Anti-Tumor Effects

Our combination of aPD1 and tFUS showed trending tumor growth control and T cell-dependent anti-tumor immunity (**Figure 4.5H**). aPD1 alone partially controls EMT6 tumor growth [188], recapitulating the responder-nonresponder phenomenon seen clinically (**Figure 4.5B**). Yet, aPD1 and tFUS separately failed to control tumor growth (**Figure 4.5C, D**). aPD1 + tFUS yielded a less robust anti-tumor response than DC101 + tFUS, with only trending tumor growth control, trending survival benefits, and half of rechallenged mice rejecting their rechallenge. Using tumor size at day 28 to generate an effect metric, we leveraged two synergy tests [189] to determine that the effects of aPD1 and tFUS are additive (**Figure 4.7C, D**). This additive therapeutic relationship may be due to tFUS-mediated inflammation promoting T cell recruitment to the ablated site, followed by aPD1 augmenting T cell proliferation and effector

function. However, we begin aPD1 treatment prior to tFUS, and tFUS may ablate some intratumoral T cells. For this reason, continuing aPD1 dosing following tFUS may render the aPD1 + tFUS combination more effective. T cell extravasation may also bottleneck aPD1 + tFUS efficiency due to dysfunctional tumor vasculature, which may be addressed by incorporating DC101. Ultimately, aPD1 bolsters T cell proliferation and effector function once T cells have extravasated into solid tumors. However, this is limited by tumors' dysfunctional vasculature, which DC101 addresses, and can be improved by tFUS, which initiates antigen release upstream of T cell homing.

4.4.4 Synergy Between DC101 and tFUS

While DC101 and tFUS individually offered little anti-tumor protection, their combination synergistically controlled tumor growth (**Figure 4.4C, D**, **Figure 4.7A, B**), improved survival (**Figure 4.4E**), and induced long-term adaptive immunity (**Figure 4.4F**). This synergy may stem from several DC101-mediated effects. We demonstrated that DC101 reduced the number of regulatory T cells in EMT6 tumors by nearly 3-fold (**Figure 4.3E**), alleviating immunosuppression. VEGFR2 blockade can also reduce myeloid-derived suppressor cells' (MDSCs) immunosuppressive capacity [71], further reducing intratumoral immunosuppression. tFUS may complement DC101 through MDSC ablation and augmented antigen release. Additionally, DC101 is known to reduce hypoxia [190], interstitial fluid pressure [190], and tumor perfusion [191], potentially improving heat transfer post-ablation, which may result in more functional antigen release and preservation of tumor parenchyma for T cell homing.

Importantly, DC101 can also improve lymphatic function in tumors, despite previous work finding that DC101 primarily impacts interstitial fluid pressure [81]. Although DC101 functions by blocking VEGF-A's primary receptor, VEGFR2, and lymphangiogenesis occurs via VEGF-C and its receptor, VEGFR3, DC101 can also reduce lymphatic vessel density [192], [193]. DC101 treatment also decreases lymphatic vessel hyperbranching, improving lymphatic

vessel function [194]. DC101 promotes the formation of lymphatic structures like high endothelial venules (HEVs) in tumors [195], which assist in antigen trafficking to lymph nodes, and increase dendritic cells' (DCs) MHC-II expression [71], augmenting DC's capacity for antigen presentation. Additionally, DC101 reduces the likelihood for lymphatic metastases [80], [196]. Together, these mechanisms likely drive the durable T cell-dependent anti-tumor responses observed following DC101 + tFUS treatment.

It is also interesting that DC101 was more effective than aPD1 in boosting the immunological efficacy of tFUS. This finding was unexpected because aPD1 monotherapy is a mainstay in the ICI armamentarium, while VEGF blockade has not shown similar clinical effectiveness. However, augmenting T cell activity with aPD1 may be ineffective if T cells struggle to enter, survive, and properly function in tumors, even with an inflammatory event such as tFUS spurring T cell recruitment. DC101's ability to improve leukocyte access, reduce intratumoral hypoxia, curb immunosuppression, and ameliorate lymphatic function may be necessary ingredients to synergize immunomodulatory drugs with tFUS.

DC101 immunologically primes solid tumors. This allows them to readily accept T cells, permit T cell function and proliferation, reduce intratumoral immunosuppression, augment lymphatic function, and facilitate adequate heat transfer post-ablation. Alone, DC101 is largely ineffective, as it does not elicit tumor control. But without DC101, the tumor environment is inadequately prepared to be maximally receptive to aPD1 or tFUS.

4.4.5 Maximal Anti-Tumor Effects Combining DC101, aPD1 and tFUS

Combining DC101, aPD1, and tFUS to treat EMT6 tumors reduced tumor burden by 5-fold (**Figure 4.6D**) in an additive manner (**Figure 4.7E, F**), eradicated 80% of tumors (**Figure 4.6F**), improved animal survival (Figure 6E), and drove durable adaptive immunity (**Figure 4.6M**). This efficacy may stem from both immunological and transport mechanisms. VEGFR2

blockade reduces immunosuppressive capacity of intratumoral myeloid-derived suppressor cells (MDSCs) [71], which may increase aPD1 effectiveness in EMT6 tumors. DC101's promotion of tumor-associated HEVs is known to increase aPD1 efficacy [197], further underscoring our rationale to boost aPD1's impact with DC101. Additionally, DC101 may improve heat transfer out of the tumor, enhancing intratumoral CD8 T cell survival, further synergizing with tFUS. This body of evidence helps elucidate a theory to explain why these three therapeutics enhance each other's effects to maximally control solid tumor progression.

4.5 Conclusion

As the clinical success of promising immunotherapies remains low, understanding how to boost their efficacy is essential. In the studies highlighted in Chapter 4, leveraged the benefits of tFUS-promoted cellular damage, DC101-dependent vascular modulation, and anti-PD1-mediated T cell activity to a novel immunotherapeutic framework. After confirming that DC101 improves intratumoral T cell composition and sparse tFUS elicits little long-term benefit to tumor control in EMT6 tumors, we logically combine these therapies with anti-PD1 across a range of studies to find that many of the ensuing combinations yield significant tumor growth control, eradication, and survival. We reproduce these results in both the 4T1 and YUMMER1.7 models of TNBC and melanoma, respectively. We then demonstrate that many mice whose EMT6 tumors were eradicated remain tumor-free following contralateral rechallenge and isolate this effect to be T cell-dependent. These studies illustrate how sparse tFUS can be potentiated using immunomodulatory drugs with clinical analogs like DC101 and anti-PD1 and why resulting long-term anti-tumor effects occur, offering important insight for future clinical endeavors tackling the treatment of solid tumors and their metastases.

4.6 Materials and Methods

4.6.1 Cell and Animal Maintenance

The EMT6 and 4T1 cell lines were purchased from ATCC. The YUMMER1.7 cell line was gifted by the laboratory of Timothy N.J. Bullock. EMT6 cells were maintained in 1X DMEM + 4.5 g/L D-glucose + L-Glutamine (Gibco #11965-092) supplemented with 10% Fetal Bovine Serum (FBS, Gibco #16000-044). 4T1 cells were maintained in 1X RPMI 1640 + L-Glutamine (Gibco #11875-093) supplemented with 10% Fetal Bovine Serum (FBS, Gibco #16000-044). YUMMER1.7 cells were maintained in 1X DMEM/F12 (1:1) + L-Glutamine + 15 mM HEPES supplemented with 10% Fetal Bovine Serum (FBS, Gibco #16000-044) and 1% MEM Non-Essential Amino Acids (NEAA, Gibco # 11140-050). All cells were maintained in culture at 37°C and 5% CO_2 (Thermo Fisher Scientific, Heracell 150i Cat#51-032-871). Thawed cells were maintained in logarithmic growth phase for all experiments, did not exceed 12 passages from the time of purchase, and tested negative for mycoplasma prior to freezing.

All animal experiments adhered to ethical guidelines and regulations approved by the University of Virginia Animal Care and Use Committee. The animals were housed in accordance with standard laboratory conditions, maintaining a temperature of 22°C and a 12-hour light/12-hour dark cycle and supplied food ad libitum. 7-10 week-old female BALB/c or C57BL/6 mice were purchased from Jackson Laboratories (Jax #000651 or #000664, respectively) and acclimated for at least 48 hours in our animals facilities. To prepare the animals for inoculations, they were anesthetized with an intraperitoneal injection of ketamine (50 mg/kg Zoetis) and dexdomitor (0.25 mg/kg Pfizer). Their right flanks were shaved and $5x10^5$ EMT6 cells, $4x10^5$ 4T1 cells, or $3x10^5$ YUMMER1.7 cells were subcutaneously injected in 100 µL 1X PBS (Gibco #10010-023) with a 25G x 1 ½ inch needle (BD PrecisionGlide Needle #305127) into the right flank of the mice, allowed to rest for 30 minutes, after which animals were given Antisedan

intraperitoneally for anesthesia reversal and recovery. Tumor outgrowth was assessed with digital calipers, with tumor volume = (length x width^2/2). Seven days following inoculation, mice were randomly placed in experimental groups while matching the starting tumor mean volume and minimizing intragroup variation. When appropriate, animals were rechallenged with inoculations following the same procedure, but on the left flank.

4.6.2 VEGFR2 Blockade

For VEGFR2 blockade, mice were injected with 5 or 10 mg/kg DC101 (DC101 #BE0060 BioXCell) or appropriate IgG antibody control (rat IgG1 HRPN #BE0088 BioXCell) diluted in sterile 1X PBS (Gibco #10010-023). DC101 and IgG were prepared the day of injections, and the 5 or 10 mg/kg calculation was determined at the day 7 size matching. Mice were interperitoneally injected with 100 µL of diluted DC101 or IgG at starting on day 7 post-inoculation, with 2 or 3 additional doses administered 3 days apart.

4.6.3 PD-1 Blockade Therapy

For PD-1 blockade, mice were injected with 200 µg aPD1 (RMP1-14 #BE0146 BioXCell) or appropriate IgG antibody control (rat IgG2a 2A3 #BE0089 BioXCell) diluted in sterile 1X PBS (Gibco #10010-023). DC101 and IgG were prepared on the day of injections, and the 10 mg/kg calculation was determined at the day 7 size matching. Mice were interperitoneally injected with 100 µL of diluted aPD1 or IgG at starting on day 7 post-inoculation, with 2 or 3 additional doses administered 3 days apart.

4.6.4 T Cell Depletions

For T cell depletions, anti-CD8 (2.43 clone; Bio X Cell) and anti-CD4 (GK1.5 clone; Bio X Cell) were diluted in sterile 1X PBS (Gibco #10010-023) and administered intraperitoneally daily for three days. Mice were injected with 100 µg of each antibody on each of these three days.

4.6.5 *In Vivo Ultrasound-guided Partial Thermal Ablation*

System 1: This system consists of four 3.78 MHz single-element transducers (SU-102, Sonic Concept), each of 33 mm diameter and 55 mm radius of curvature, with a 3.78 MHz center frequency. These four transducers are embedded in a solid resin and are confocally aligned for a single active aperture of 66 mm. The system is powered by a 200W acoustic amplifier (Electronics & Innovation 1020L) driven by an arbitrary function generator (Tektronix AFG3022C) registered to an ultrasound imaging transducer (MS200, center frequency 30 MHz, FUJIFILM Visualsonics). A degassed water bath at 37°C acoustically coupled mice to both the therapeutic and imaging ultrasound transducers. After acoustic coupling, tumor positioning was driven by a motorized 3D motion stage and the tumor was identified with B-mode ultrasound imaging. Tumors were treated with the transducer operated in continuous wave mode at 18W power for 15 seconds per point, with each treatment point 1.5 mm apart. Tumors were treated in 2 or 3 planes of sonication, each 2 mm apart.

System 2: This system consists of a 64 mm single-element 3.3 MHz transducer (Sonic Concepts) powered by a 400 W amplifier (E&I) orthogonally registered to an 8 MHz linear ultrasound imaging array (Siemens). A degassed water bath at 37°C acoustically coupled mice to both the therapeutic and imaging ultrasound transducers. After acoustic coupling, tumor positioning was driven by a motorized 3D motion stage and the tumor was identified with B-mode ultrasound imaging. A grid of points 3 mm apart was overlayed onto the B-mode images. Tumors were treated with the transducer operated at 3MHz in continuous wave mode at 15W power for 10 seconds per point, and were treated in two planes of sonication, each 2 mm apart.

4.6.6 *TTC Tumor Tissue Staining*

Immediately following ablation, some mice were euthanized with an intraperitoneal Euthasol injection. After confirming successful euthanasia, entire tumors were removed from the

right flank, sectioned down the midline, and placed in 5 mL 2,3,5-triphenyltetrazolium chloride (TTC) stain (298-96-4, Sigma) for 30 minutes at 37°C, taking care to avoid light exposure during the incubation time. TTC is a redox indicator and is reduced to bright-red 1,2,5-triphenylformazan in living cells, where necrotic or dead cells appear white. Tumors were then moved to 10% formalin for 72 hours and gross images of tumor cross-sectional area were acquired for quantification (ImageJ).

4.6.7 India Ink Lung Staining

Approximately 14 days post-ablation, a cohort of 4T1-bearing mice was euthanized with an intraperitoneal injection of Euthasol. Immediately following euthanasia, surgical scissors were used to cut along the animal's midline up to the salivary glands. The trachea was found and isolated using a pipette tip. A 27G needle syringe containing India Ink (J61007.AP, ThermoFisher) was inserted into the trachea in the direction of the lungs, and ink was slowly injected into the lungs until resistance was felt (~1-2 mL). The trachea was cut, the lungs were removed, and the lungs were rinsed with water. The lungs were then placed in a Falcon tube filled with 10 mL room-temperature Fekete's solution (made with 100 mL 70% ethanol, 10 mL formaldehyde, and 5 mL glacial acetic acid) and incubated for 3 days. The lungs were then removed and imaged with a dissecting microscope, after which gross images were quantified (ImageJ).

4.6.8 Flow Cytometry

To isolate intratumoral immune cells, tumors were cut into ~1mm pieces and following removal and incubated in Type I collagenase (5 mg/mL, ThermoFisher) and DNAse I (100ug/mL, Sigma) at 37C for 1 hour followed by mechanical homogenization. The disaggregated tumors were filtered through 100 µm Nitex nylon mesh (Genesee) and applied to a concentration gradient (Lympholyte-M cell separation media, Cedarlane) for cell isolation.

To isolate circulating immune cells, mice were bled via tail vein, after which blood placed in cell media to prevent clotting, then was RBC lysed (00-4333-57, ThermoFisher).

Samples were stained with viability dye (Live Dead BLUE) in 1X PBS, followed by a 15-minute incubation with Fc block (anti-mouse functional grade CD16/32 clone 2.4G2, BD Biosciences). Surface staining was performed in FACS buffer supplemented with 2% normal mouse serum (Valley Biomedical). Cells were permeabilized with Foxp3/Transcription Factor Staining Buffer Set (00-5523-00, ThermoFisher). The following antibodies were used across flow cytometry studies described in the results section: CD3 BUV563 (145-2C11, BD Biosciences), CD3 APC (145-2C11, BioLegend), CD4 eFluor450 (RM4-5, ThermoFisher), CD8a BUV805 (53-6.7, ThermoFisher), CD11b APC Fire 750 (M1/70, BioLegend), CD19 BV650 (1D3, BD Biosciences), CD19 APC Fire 750 (6D5, BioLegend), CD44 FITC (NIM-R8, BioLegend), Foxp3 PE-Cy5 (FJK-16s, ThermoFisher), PD1 BV605 (29F.1A12, BioLegend). Cells were then fixed with 1X FACS Lysis Solution (349202, BD Biosciences).

Samples were acquired on 5-laser Aurora spectral flow cytometer (Cytek) and data were analyzed with FCS Express (De Novo Software). A representative gating strategy for circulating and intratumoral T cells is provided in supplementary Figure 1.

4.6.9 Survival Criteria

The following endpoints were employed for survival studies: euthanasia following tumor outgrowth exceeding 18 mm diameter in any dimension, euthanasia due to weight loss or moribund appearance, or spontaneous death. The following endpoints were censored from survival data: euthanasia due to tumor ulceration.

4.6.10 Combination Therapy Effect-Based Assessments

To determine whether the combinations of DC101, aPD1, and tFUS elicited additive or synergistic effects, two methods were employed to compare individual components of

combination therapies to the resulting combinations: the response additivity model and the Bliss independence model. First, we calculated the percent reduction in tumor size at day 28 post-inoculation for each experimental group compared to the control group average, which we deemed our “effect”. We first used the response additivity model, which assumes synergistic effect when a combination therapy yields a greater response than the sum of the individual therapies’ effects:

$$E_{AB} > E_A + E_B$$

We also used the Bliss independence model, assumes drug synergy when the effect of two combined therapies act on different sites of action and is greater than the difference between their sum and product:

$$E_{AB} > E_A + E_B - E_A * E_B$$

4.6.11 Statistical Analyses

All results are reported as the mean ± the standard error of the mean (SEM). Statistical significance was assessed at $p < 0.05$ for all experiments and was calculated using GraphPad Prism 9 (San Diego, USA). Statistical tests are reported in Figure Legends.

4.6 CHAPTER 4 FIGURES

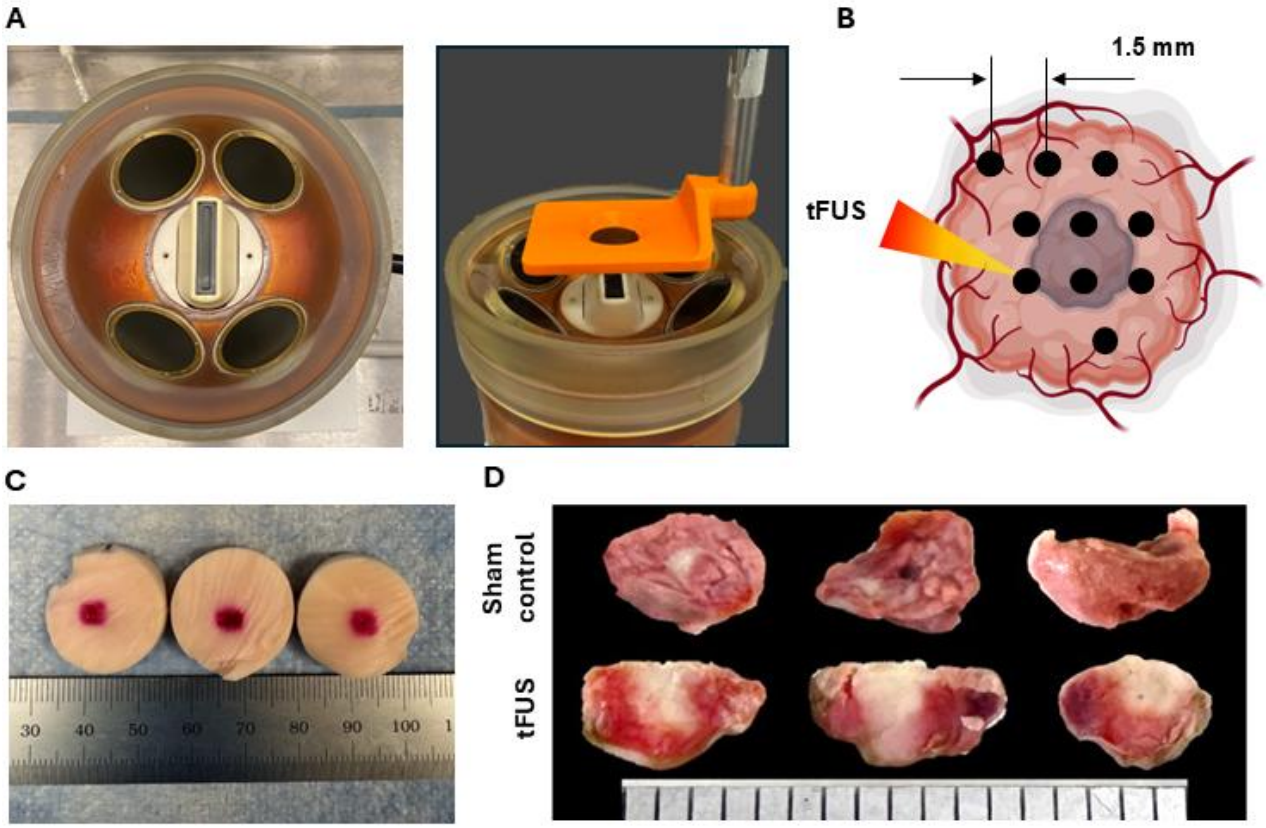

Figure 4.1. Thermal focused ultrasound equipment and parameters. (A) We employed the pictured 3.78 MHz four-element focused ultrasound transducer setup to sonicate animals in the following experiments, using a 1.5 mm spacing between points and 2 mm between treatment planes **(B)**. **(C)** We treated thermochromic gels, achieving temperatures greater than 70C when treating thermochromic gels at 18W of power for 15 seconds with 1.5 mm between treatment points, mimicking our proposed sonication regimen **(D)** We treated tumors with this regimen and used a metabolic TTC stain to assess intratumoral damage, with metabolically active tissue staining red.

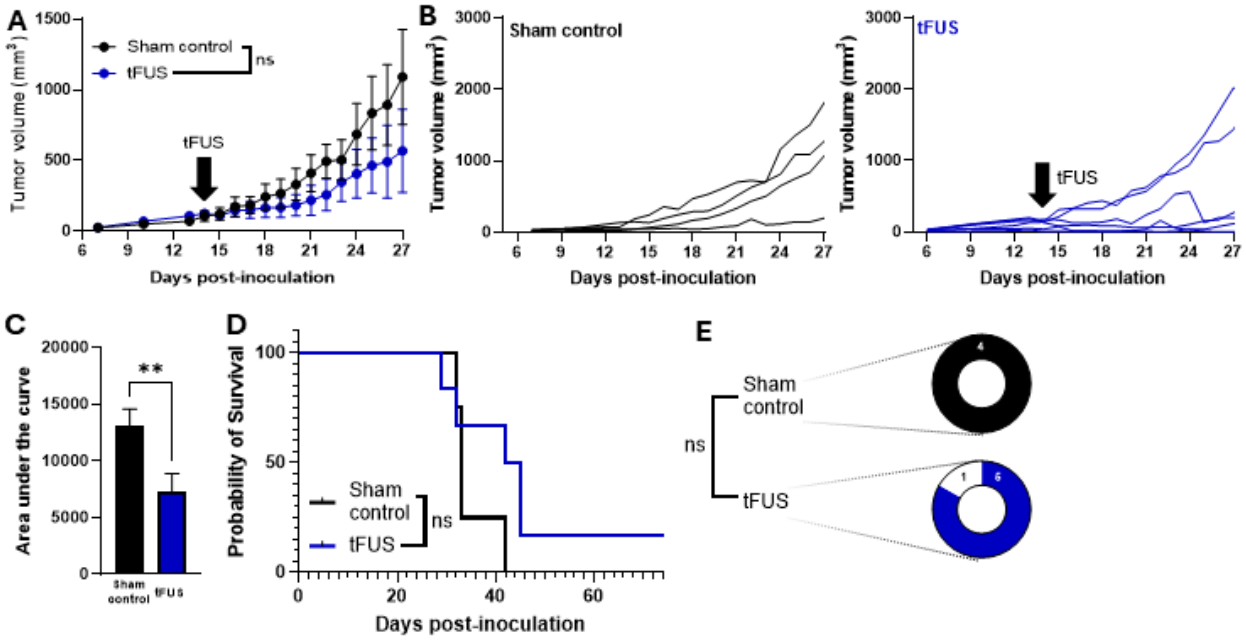

Figure 4.2. tFUS insufficiently slows EMT6 tumor growth. A. Grouped tumor growth over time. Mixed-model, two-way, repeated measures ANOVA ($p = 0.256$). Means ± SEM. **B.** Individual growth curves. **C.** Area under the curve (AUC) for tumor growth. Unpaired Welch's t-test ($p = 0.0074$). Means ± SEM. **D.** Kaplan-Meier curve depicting overall survival ($p = 0.206$), with significance assessed by log-rank (Mantel-Cox). **E.** Tumor eradication rate ($p = 1$). Fisher's exact test.

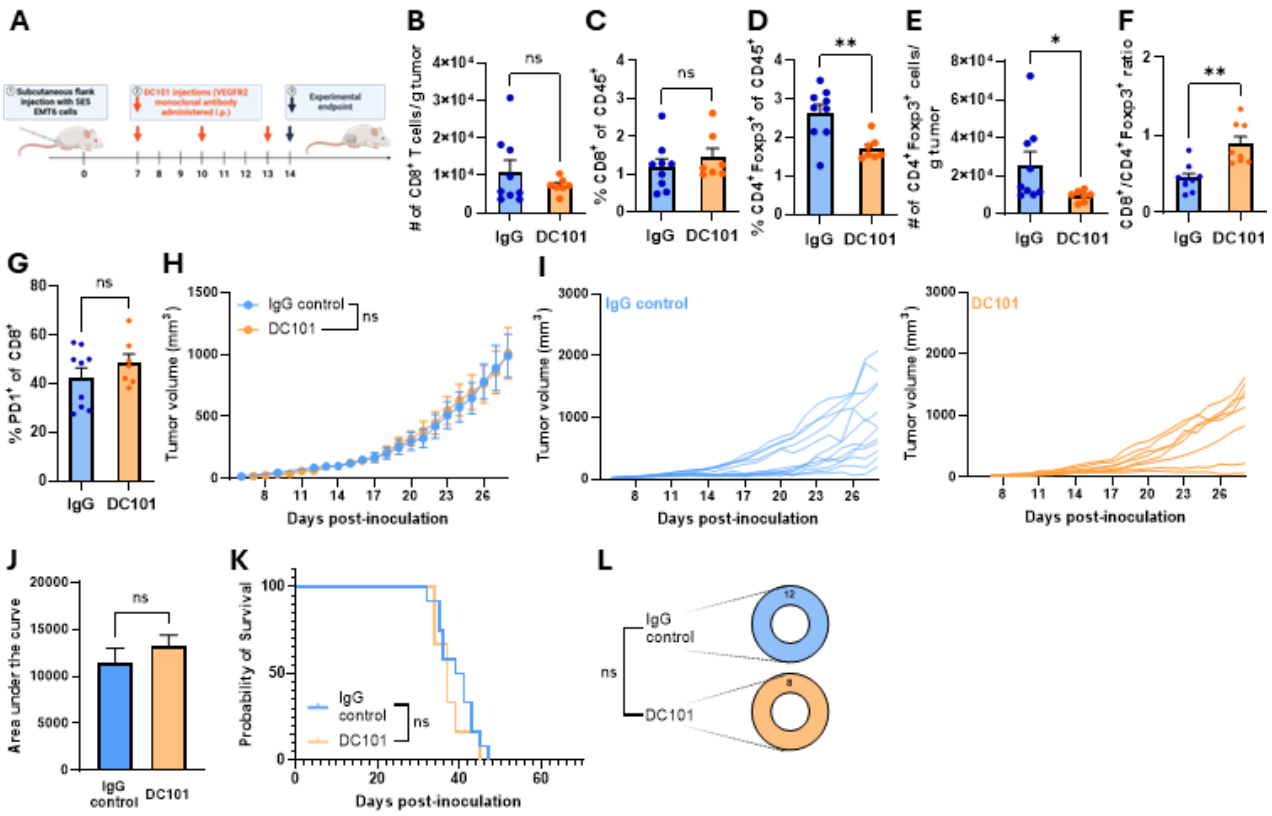

Figure 4.3. Partial VEGFR2 blockade modulates T cell compartment without controlling tumor growth. A. Timeline for inoculation and treatment. **B.** Number of CD8 T cells per gram of tumor ($p = 0.281$). **C.** Percentage of intratumoral immune cells that are CD8 T cells ($p = 0.447$). **D.** Number of CD4 T cells per gram of tumor ($p = 0.0035$). **E.** Percentage of intratumoral immune cells that are CD4 T cells ($p = 0.0499$). **F.** Ratio of intratumoral CD8 to CD4 T cells ($p = 0.0022$). **G.** Percentage of intratumoral T cells that express PD1 ($p = 0.290$). Unpaired Welch's T test. Means ± SEM. **H.** Grouped tumor growth over time. Mixed-model, two-way, repeated measures ANOVA ($p = 0.509$). **I.** Individual growth curves. **J.** Area under the curve (AUC) for tumor growth. Unpaired Welch's t-test ($p = 0.369$). Means ± SEM. **K.** Kaplan-Meier curve depicting overall survival ($p = 0.402$), with significance assessed by log-rank (Mantel-Cox). **L.** Tumor eradication rate ($p = 1$). Fisher's exact test.

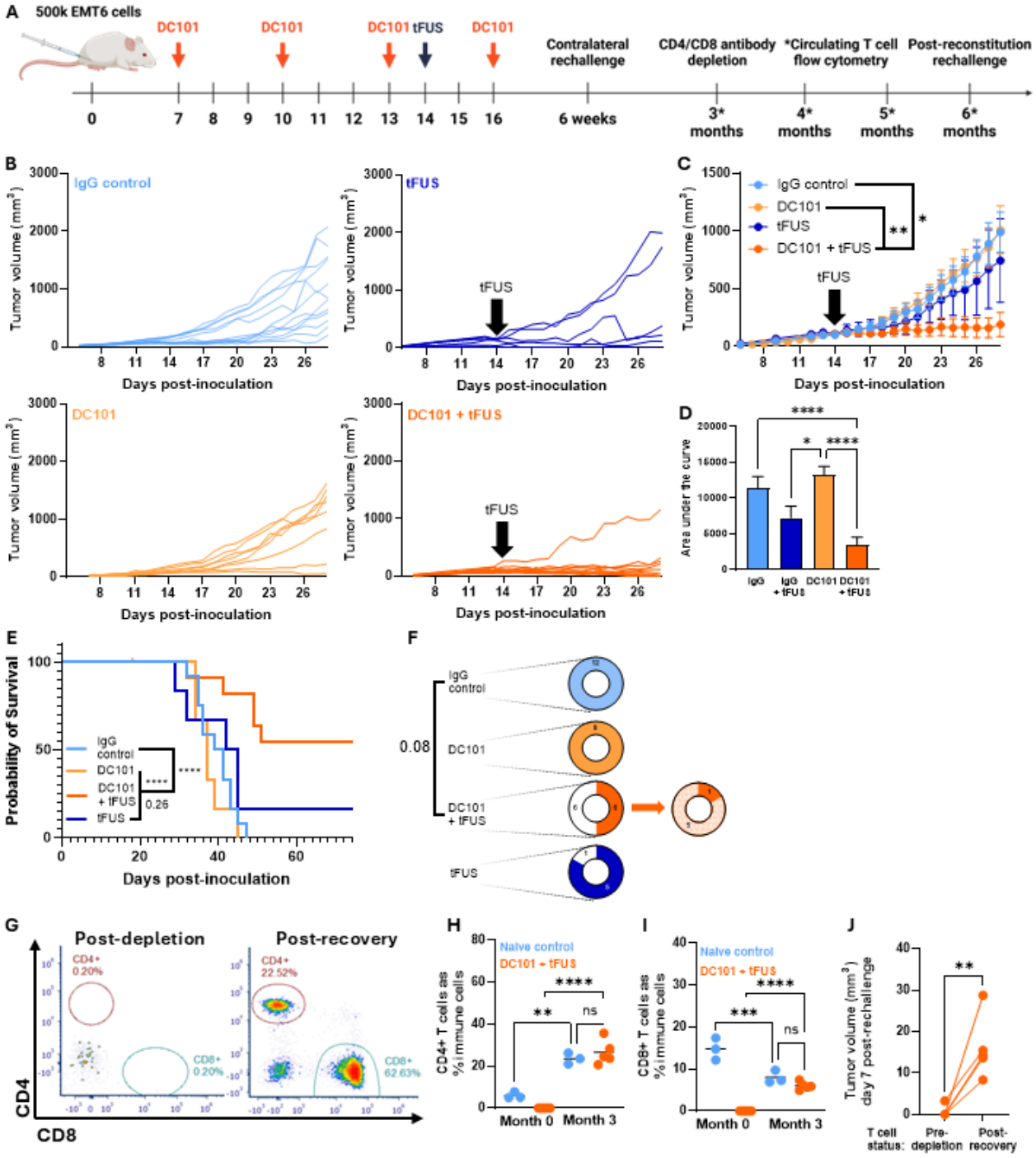
A
500k EMT6 cells
DC101
DC101
DC101
tFUS
DC101
Contralateral rechallenge
CD4/CD8 antibody depletion
*Circulating T cell flow cytometry
Post-reconstitution rechallenge
0
7
8
9
10
11
12
13
14
15
16
6 weeks
3* months
4* months
5* months
6* months
B
IgG control
tFUS
DC101
DC101 + tFUS
Tumor volume (mm³)
Days post-inoculation
C
IgG control
DC101
tFUS
DC101 + tFUS
**
*
D
Area under the curve
****
*
IgG
IgG + tFUS
DC101
DC101 + tFUS
E
Probability of Survival
IgG control
DC101
DC101 + tFUS
tFUS
****
0.26
F
0.08
G
Post-depletion
Post-recovery
CD4+ 0.20%
CD8+ 0.20%
CD4+ 22.52%
CD8+ 62.63%
CD4
CD8
H
Naive control
DC101 + tFUS
CD4+ T cells as %immune cells
Month 0
Month 3
I
CD8+ T cells as %immune cells
J
Tumor volume (mm³) day 7 post-rechallenge
T cell status:
Pre-depletion
Post-recovery

Figure 4.4. tFUS synergizes with DC101 to control primary tumor growth and generate a systemic anti-tumor response. A. Timeline for inoculation and treatment. **B.** Individual growth curves. **C.** Grouped tumor growth over time. Mixed-model, two-way, repeated measures ANOVA ($p = 0.0207$ between IgG control and DC101 + tFUS, $p = 0.007$ between DC101 and DC101 and DC101 + tFUS). Means ± SEM. **D.** Area under the curve (AUC) for tumor growth. Two-way ANOVA with Tukey test (tFUS vs. DC101 $p = 0.0276$, DC101 vs. DC101 + tFUS $p < 0.0001$, IgG control vs. DC101 + tFUS $p < 0.0001$). Means ± SEM. **E.** Kaplan-Meier curve depicting overall survival, with significance assessed by log-rank (DC101 vs. DC101 + tFUS $p = 0.0006$, IgG control vs. DC101 + tFUS $p = 0.0006$). **F.** Tumor eradication rate ($p = 0.08$) and rechallenge rejection rate. Fisher's exact test. **G.** Representative plots of circulating CD4 and CD8 T cells immediately post-antibody depletion and post-recovery 3 months later. **H.** Percentage of immune cells that are CD4 T cells in circulation, immediately post-depletion and 3 months later. Two-way ANOVA with Tukey test (Naïve month 0 vs. naïve month 3 $p = 0.0019$, DC101 + tFUS month 0 vs. DC101 + tFUS month 3 $p = 0.0004$). **I.** Percentage of immune cells that are CD4 T cells in circulation, immediately post-depletion and 3 months later. Two-way ANOVA with Tukey test (Naïve month 0 vs. naïve month 3 $p = 0.0002$, DC101 + tFUS month 0 vs. DC101 + tFUS month 3 $p < 0.0001$). **J.** Tumor volume 7 days post-rechallenge in the same mice, pre-T cell depletion and post-T cell recovery. Unpaired Welch's t-test ($p = 0.0094$).

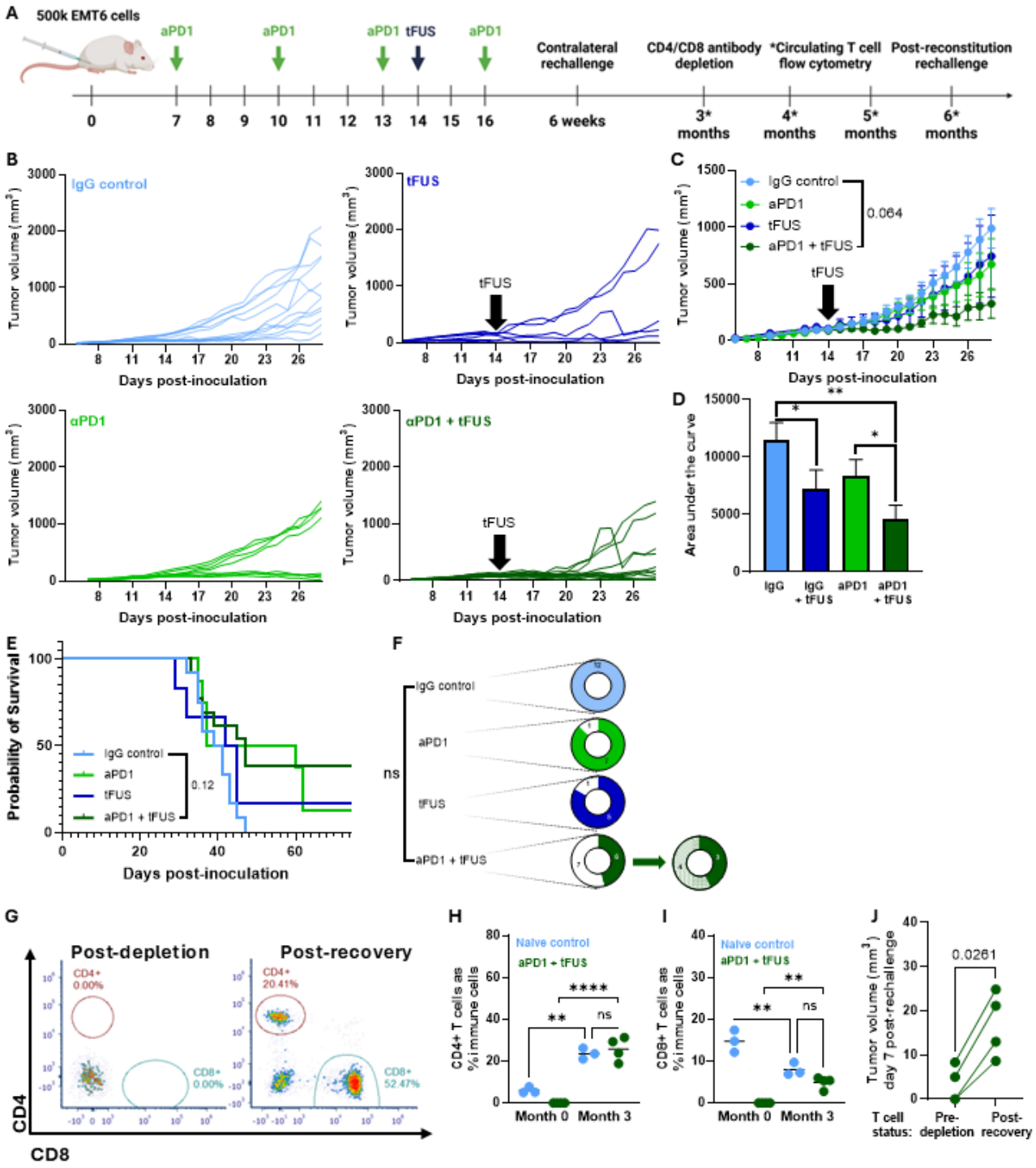
A
500k EMT6 cells
aPD1
aPD1
aPD1 tFUS
aPD1
Contralateral rechallenge
CD4/CD8 antibody depletion
*Circulating T cell flow cytometry
Post-reconstitution rechallenge
0 7 8 9 10 11 12 13 14 15 16
6 weeks
3* months
4* months
5* months
6* months
B
IgG control
tFUS
αPD1
αPD1 + tFUS
Tumor volume (mm³)
Days post-inoculation
C
IgG control
aPD1
tFUS
aPD1 + tFUS
0.064
D
Area under the curve
IgG
IgG + tFUS
aPD1
aPD1 + tFUS
E
Probability of Survival
0.12
F
ns
G
Post-depletion
Post-recovery
CD4+ 0.00%
CD8+ 0.00%
CD4+ 20.41%
CD8+ 52.47%
CD4
CD8
H
Naïve control
aPD1 + tFUS
CD4+ T cells as %immune cells
Month 0
Month 3
I
CD8+ T cells as %immune cells
J
Tumor volume (mm³) day 7 post-rechallenge
0.0261
T cell status:
Pre-depletion
Post-recovery

Figure 4.5. tFUS additively cooperates with aPD1 to control primary tumor growth and induce long-term immunity. A. Timeline for inoculation and treatment. **B.** Individual growth curves. **C.** Grouped tumor growth over time. Mixed-model, two-way, repeated measures ANOVA. Means ± SEM. **D.** Area under the curve (AUC) for tumor growth. Two-way ANOVA with Tukey test (IgG control vs. aPD1 + tFUS $p = 0.0011$, IgG control vs. tFUS $p = 0.0485$, aPD1 vs. FUS + aPD1 $p = 0.0485$). Means ± SEM. **E.** Kaplan-Meier curve depicting overall survival, with significance assessed by log-rank. **F.** Tumor eradication rate ($p = 0.51$) and rechallenge rejection rate. Fisher's exact test. **G.** Representative plots of circulating CD4 and CD8 T cells immediately post-antibody depletion and post-recovery 3 months later. **H.** Percentage of immune cells that are CD4 T cells in circulation, immediately post-depletion and 3 months later. Two-way ANOVA with Tukey test (Naïve month 0 vs. naïve month 3 $p = 0.0018$, aPD1 + tFUS month 0 vs. aPD1 + tFUS month 3 $p < 0.0001$). **I.** Percentage of immune cells that are CD4 T cells in circulation, immediately post-depletion and 3 months later. Two-way ANOVA with Tukey test (Naïve month 0 vs. naïve month 3 $p = 0.0032$, aPD1 + tFUS month 0 vs. aPD1 + tFUS month 3 $p = 0.0091$). **J.** Tumor volume 7 days post-rechallenge in the same mice, pre-T cell depletion and post-T cell recovery. Unpaired Welch's t-test.

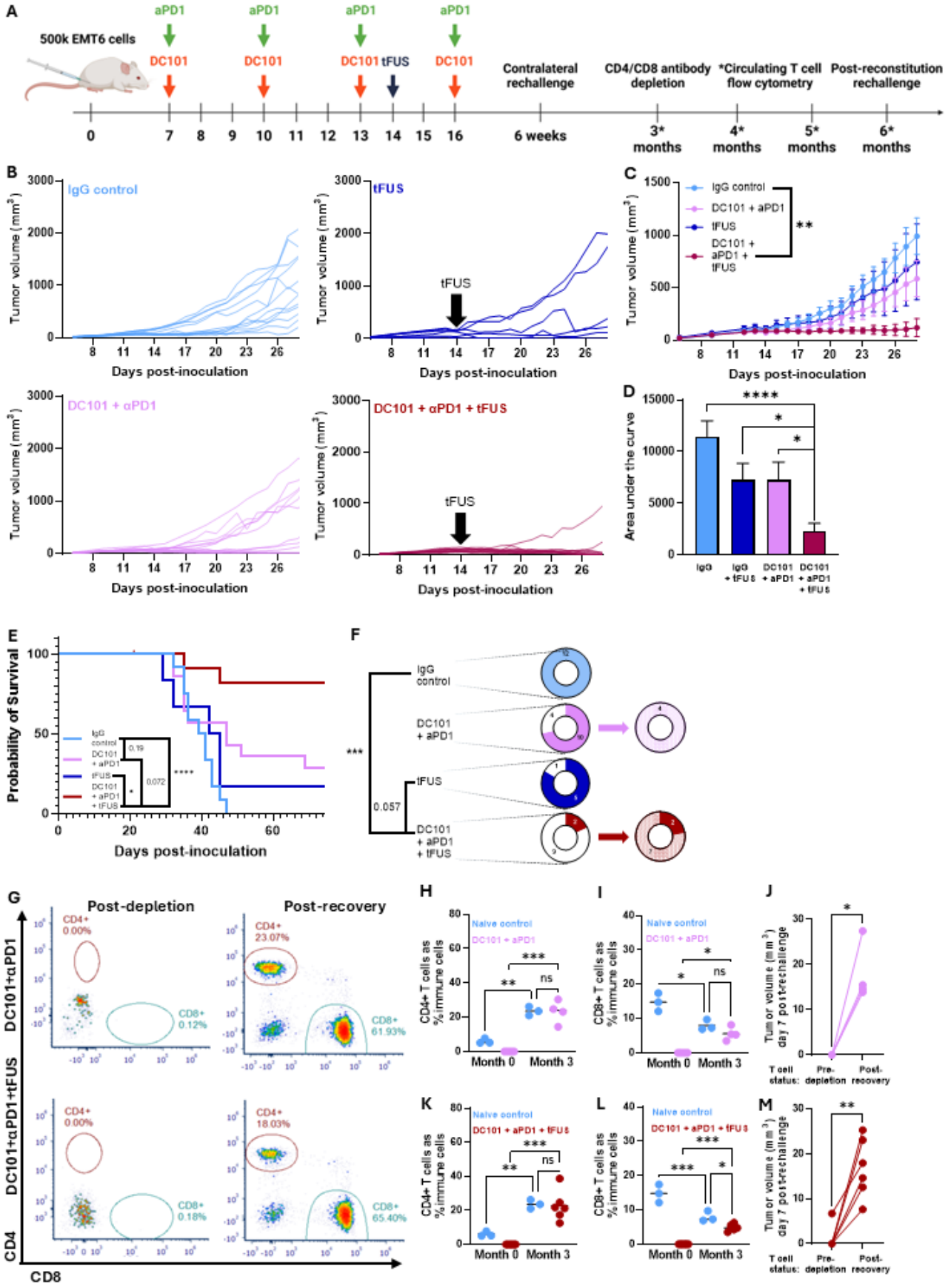
A
500k EMT6 cells
aPD1
DC101
tFUS
Contralateral rechallenge
CD4/CD8 antibody depletion
*Circulating T cell flow cytometry
Post-reconstitution rechallenge
0
7
8
9
10
11
12
13
14
15
16
6 weeks
3* months
4* months
5* months
6* months
B
IgG control
tFUS
DC101 + αPD1
DC101 + αPD1 + tFUS
Tumor volume (mm³)
Days post-inoculation
C
IgG control
DC101 + aPD1
tFUS
DC101 + aPD1 + tFUS
**
D
Area under the curve
****
*
IgG
IgG + tFUS
DC101 + aPD1
DC101 + aPD1 + tFUS
E
Probability of Survival
IgG control
DC101 + aPD1
tFUS
DC101 + aPD1 + tFUS
0.19
0.072
F
IgG control
DC101 + aPD1
tFUS
DC101 + aPD1 + tFUS
***
0.057
G
Post-depletion
Post-recovery
DC101+αPD1
DC101+αPD1+tFUS
CD4
CD8
CD4+ 0.00%
CD8+ 0.12%
CD4+ 23.07%
CD8+ 61.93%
CD4+ 0.00%
CD8+ 0.18%
CD4+ 18.03%
CD8+ 65.40%
H
Naive control
DC101 + aPD1
CD4+ T cells as % immune cells
Month 0
Month 3
ns
I
CD8+ T cells as % immune cells
J
Tumor volume (mm³) day 7 post-rechallenge
T cell status:
Pre-depletion
Post-recovery
K
Naive control
DC101 + aPD1 + tFUS
L
M

Figure 4.6. tFUS, DC101, and aPD1 potently cooperate to eradicate tumors and generate a systemic anti-tumor response. A. Timeline for inoculation and treatment. **B.** Individual growth curves. **C.** Grouped tumor growth over time. Mixed-model, two-way, repeated measures ANOVA ($p = 0.006$). Means ± SEM. **D.** Area under the curve (AUC) for tumor growth. Two-way ANOVA with Tukey test (tFUS vs. DC101 + aPD1 + tFUS $p = 0.0212$, IgG vs. DC101 + aPD1 + tFUS $p < 0.0001$, IgG vs. tFUS $p = 0.0161$, IgG vs. DC101 + aPD1 = 0.0212, DC101 + aPD1 vs. DC101 + aPD1 + tFUS $p = 0.0161$). Means ± SEM. **E.** Kaplan-Meier curve depicting overall survival, with significance assessed by log-rank (tFUS vs. DC101 + aPD1 + tFUS $p = 0.0384$, IgG control vs DC101 + aPD1 + tFUS $p = 0.0006$). **F.** Tumor eradication rate ($p = 0.0006$) and rechallenge rejection rate. Fisher's exact test. **G.** Representative plots of circulating CD4 and CD8 T cells immediately post-antibody depletion and post-recovery 3 months later. **H.** Percentage of immune cells that are CD4 T cells in circulation, immediately post-depletion and 3 months later. Two-way ANOVA with Tukey test (Naïve month 0 vs. naïve month 3 $p = 0.0061$, DC101 + aPD1 month 0 vs. DC101 + aPD1 month 3 $p = 0.0005$). **I.** Percentage of immune cells that are CD4 T cells in circulation, immediately post-depletion and 3 months later. Two-way ANOVA with Tukey test (Naïve month 0 vs. naïve month 3 $p = 0.0168$, DC101 + aPD1 month 0 vs. DC101 + aPD1 month 3 $p = 0.0222$). **J.** Tumor volume 7 days post-rechallenge in the same mice, pre-T cell depletion and post-T cell recovery. Unpaired Welch's t-test ($p = 0.0115$). **K.** Percentage of immune cells that are CD4 T cells in circulating, immediately post-depletion and 3 months later. Two-way ANOVA with Tukey test (Naïve month 0 vs. naïve month 3 $p = 0.0088$, DC101 + aPD1 + tFUS month 0 vs. DC101 + aPD1 + tFUS month 3 $p = 0.0001$). **L.** Percentage of immune cells that are CD4 T cells in circulating, immediately post-depletion and 3 months later. Two-way ANOVA with Tukey test (Naïve month 0 vs. naïve month 3 $p = 0.0004$, DC101 + aPD1 + tFUS month 0 vs. DC101 + aPD1 + tFUS month 3 $p = 0.0004$). **M.** Tumor volume 7 days post-rechallenge in the same mice, pre-T cell depletion and post-T cell recovery. Unpaired Welch's t-test ($p = 0.0012$).

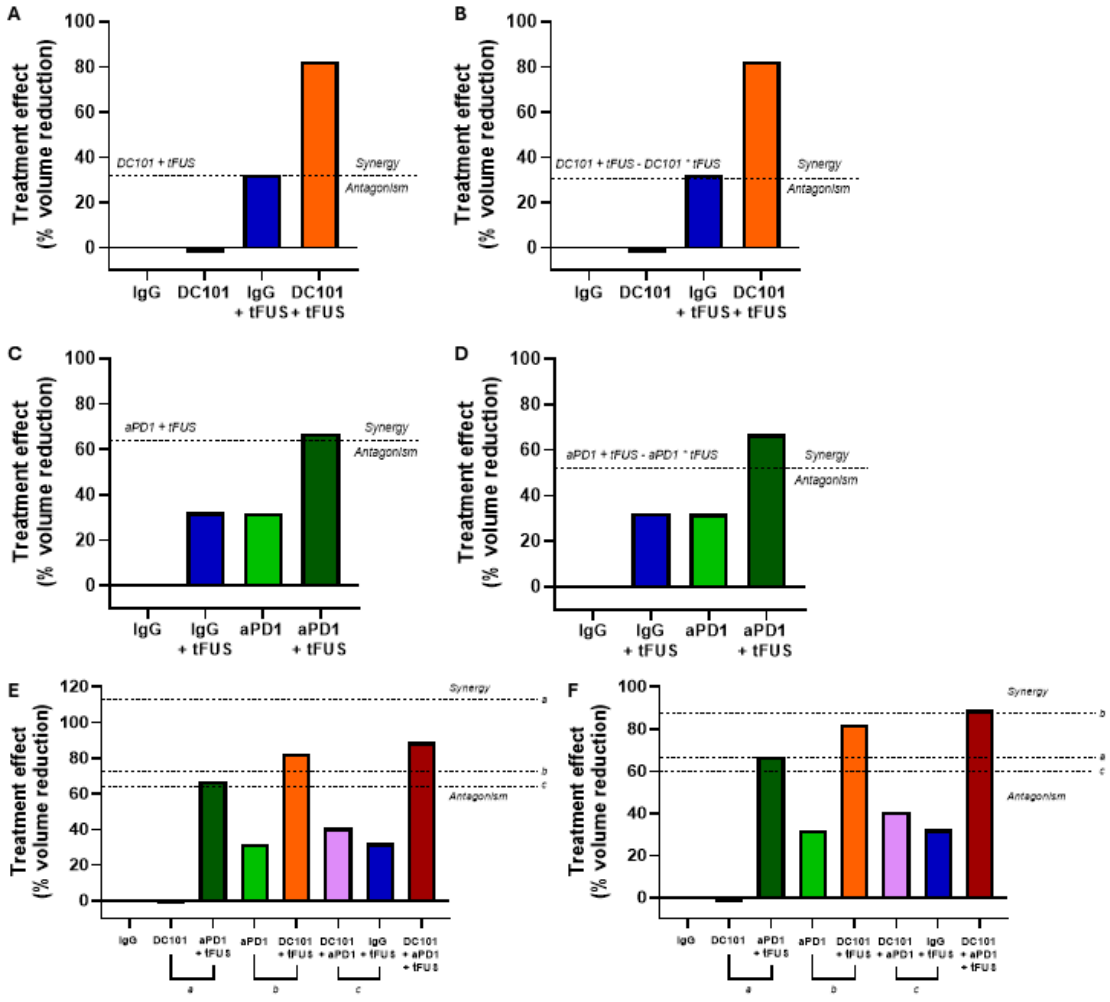

Figure 4.7. DC101, aPD1, and tFUS interaction depends on specific therapeutic combination. A "treatment effect" metric was created by quantifying the average percentage of tumor volume reduction for each treatment group compared to control. The nature of this effect (antagonistic, additive, or synergistic) was determined by calculating both Response Additivity and Bliss Independence model. **A, B.** Based on these methods, DC101 and tFUS act synergistically to reduce EMT6 tumor volume. **C, D.** aPD1 and tFUS likely act additively, perhaps with some minor synergy. **E, F.** To assess the nature of combining DC101, aPD1, and tFUS, we determined effect thresholds by comparing this triple combination to that of DC101 and aPD1 + tFUS (a), aPD1 and DC101 + tFUS (b), and DC101 + aPD1 and IgG + tFUS (c), finding that the combinatory effect of all three therapies is likely additive.

4.7 Chapter 4 Supplemental Figures

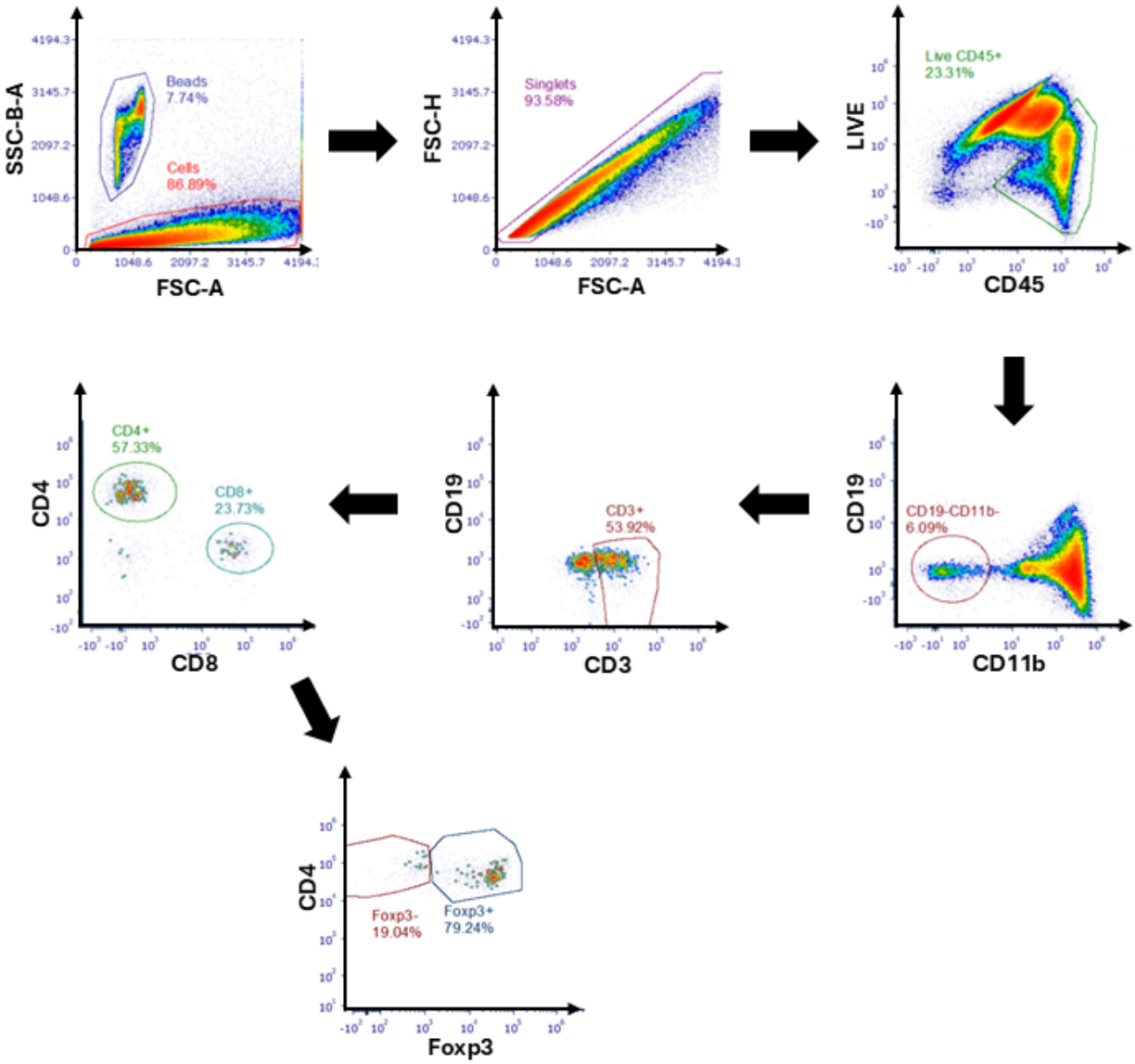

Figure 4.S1. Intratumoral immune staining gating strategy post-DC101 treatment.

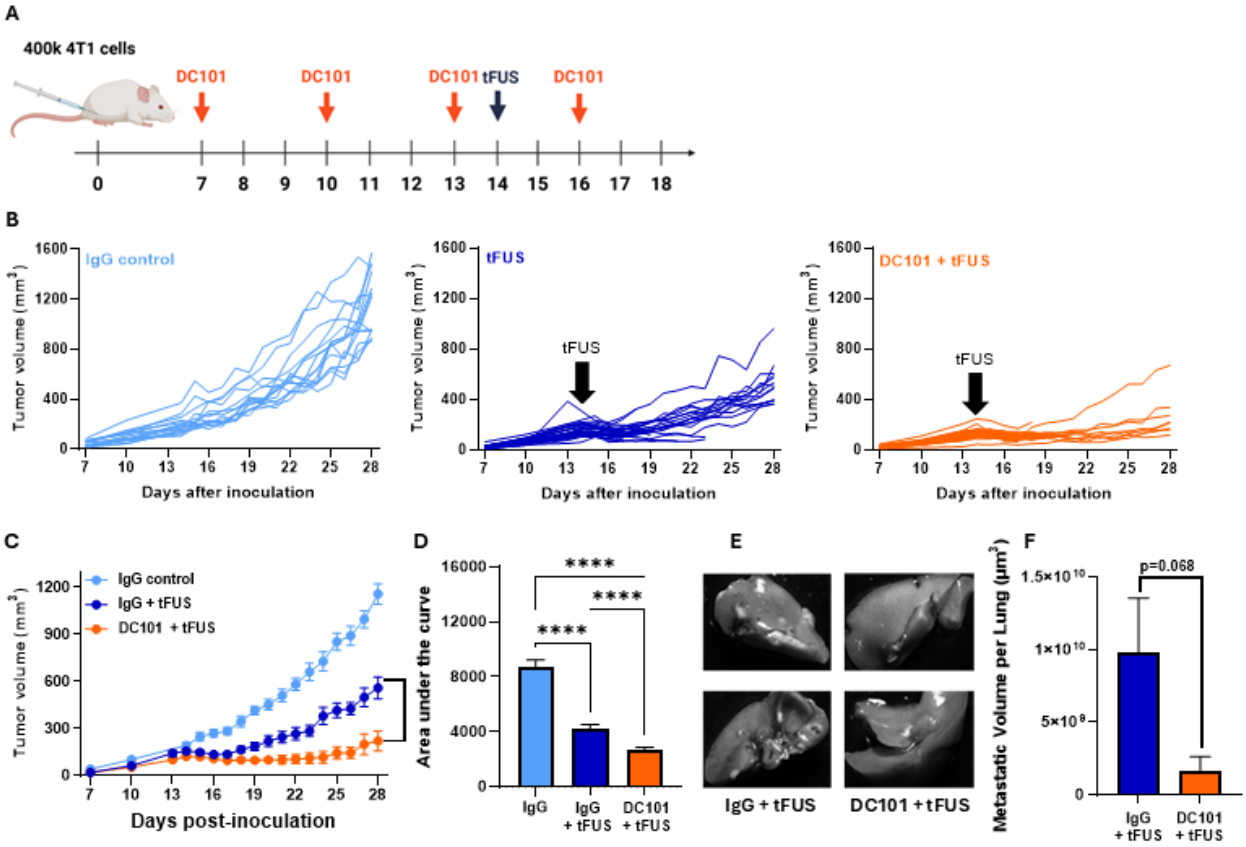

Figure 4.S2. DC101 and tFUS curb primary tumor growth and prevent distant metastases of 4T1 tumors. A. Timeline for inoculation and treatment. **B.** Individual growth curves. **C.** Grouped tumor growth over time. Mixed-model, two-way, repeated measures. Means ± SEM. **D.** Area under the curve (AUC) for tumor growth. Two-way ANOVA with Tukey test ($p < 0.0001$ for all comparisons). Means ± SEM. **E.** Representative lungs stained with India ink, with metastases visible in white. **F.** Estimated metastatic lung volume quantified in ImageJ. Welch's t-test.

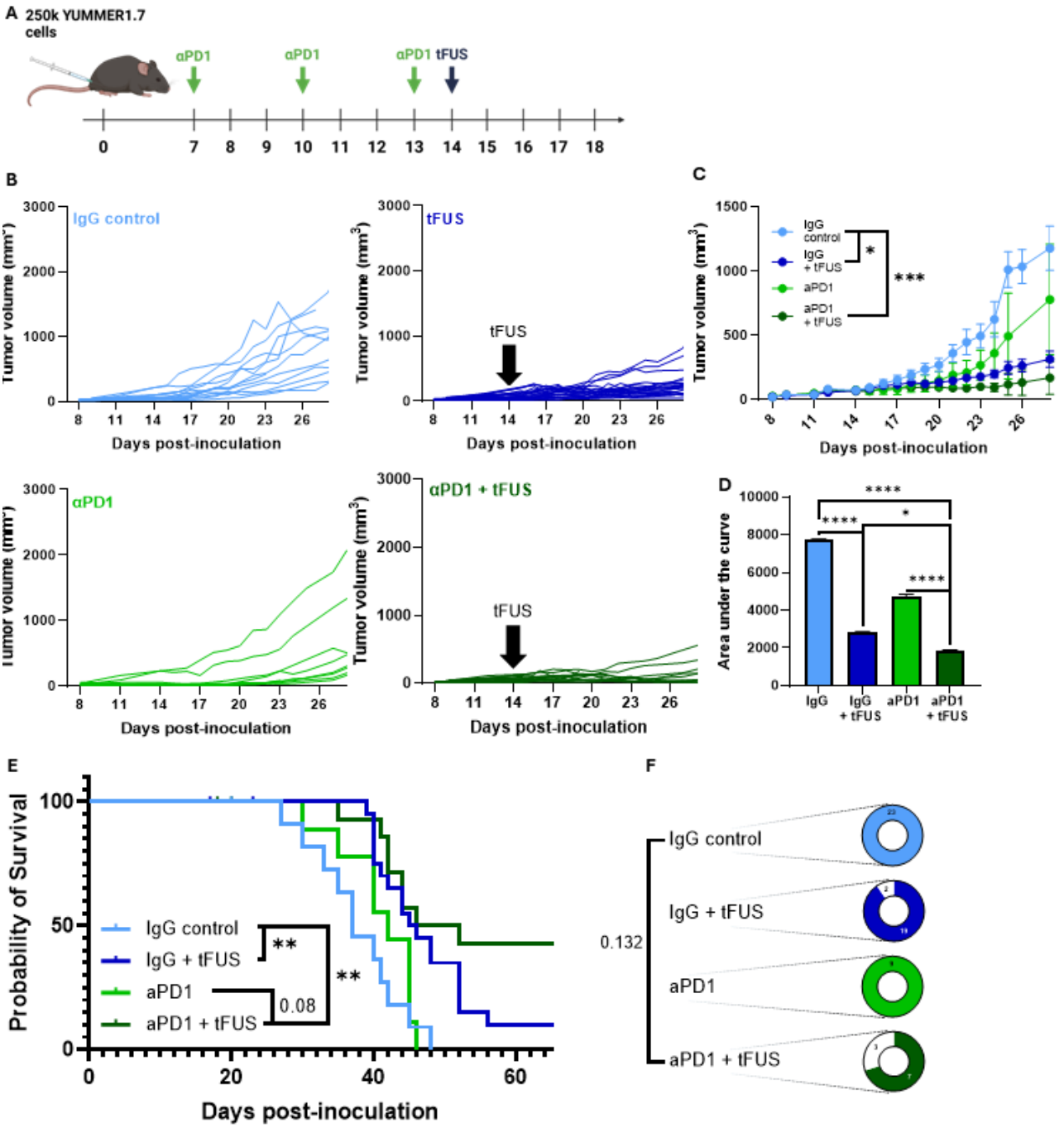

Figure 4.S3. tFUS and aPD1 cooperate to control tumor growth in YUMMER1.7 tumors. A. Timeline for inoculation and treatment. **B.** Individual growth curves. **C.** Grouped tumor growth over time. Mixed-model, two-way, repeated measures ANOVA. Means ± SEM. **D.** Area under the curve (AUC) for tumor growth. Two-way ANOVA with Tukey test ($p < 0.0001$ for all shown except tFUS vs. aPD1 + tFUS $p = 0.0373$). Means ± SEM. **E.** Kaplan-Meier curve depicting overall survival, with significance assessed by log-rank (IgG vs. tFUS $p = 0.0048$, aPD1 vs. aPD1 + tFUS $p = 0.0828$, IgG vs. aPD1 + tFUS $p = 0.003$). **F.** Tumor eradication rate, Fisher's exact test.

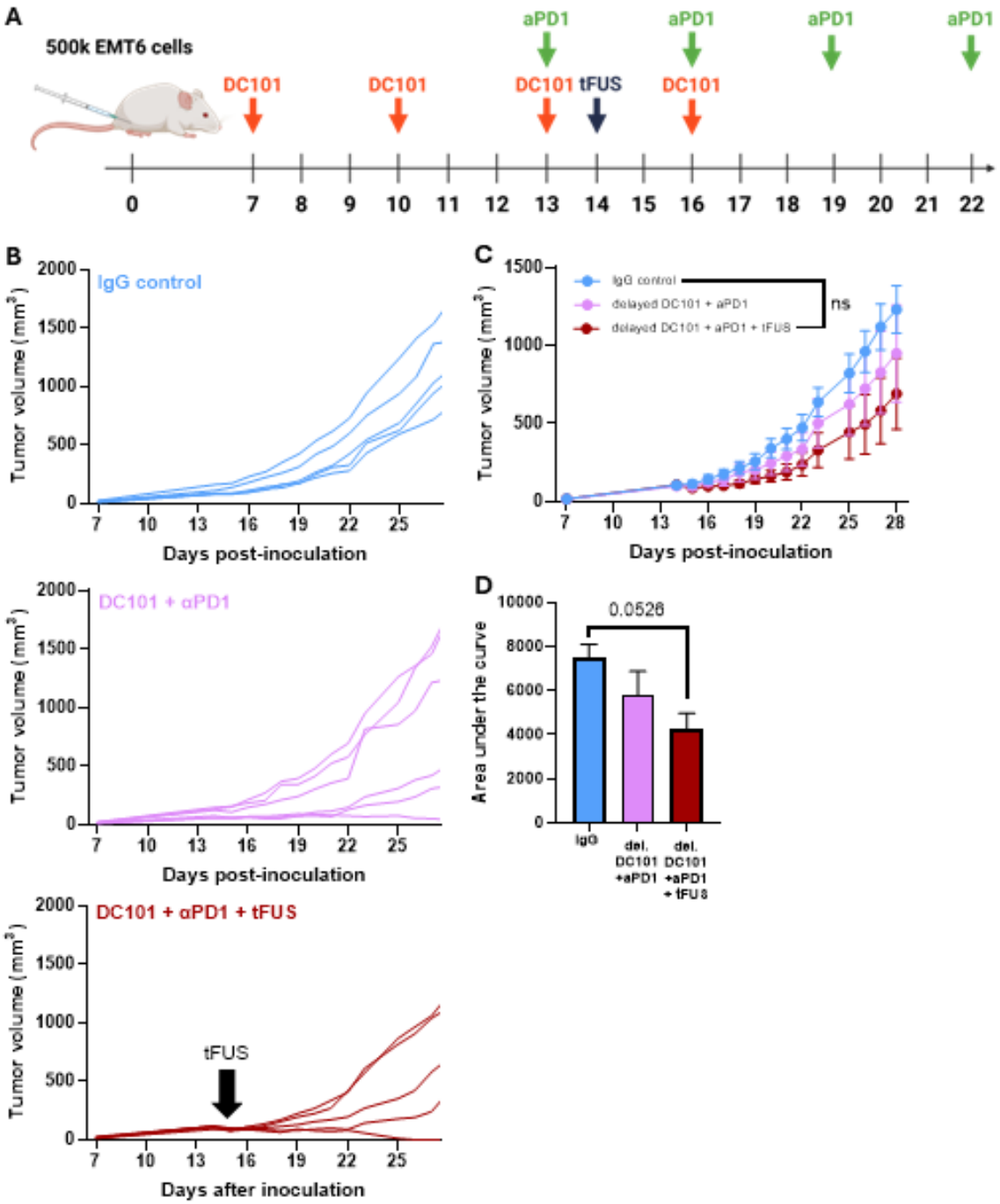

Figure 4.S4. Tuning tFUS, DC101, and aPD1 timing is essential to control tumor growth. A. Timeline for inoculation and treatment. **B.** Individual growth curves. **C.** Grouped tumor growth over time. Mixed-model, two-way, repeated measures ANOVA ($p = 0.302$). Means ± SEM. **D.** Area under the curve (AUC) for tumor growth. Two-way ANOVA with Tukey test (IgG vs. DC101 + aPD1 $p = 0.503$, DC101 + aPD1 vs. DC101 + aPD1 + tFUS $p = 0.560$). Means ± SEM.

CHAPTER 5: FUTURE DIRECTIONS

6.1 EXPLORING ALTERNATIVE TUMOR MODELS

6.1.1 IMPLANTABLE TUMOR MODELS

In both Chapter 3 and Chapter 4, we leverage murine solid tumor models to study how vascular normalization and FUS synergize in drug delivery and immunotherapy contexts, respectively. However, we can improve upon our cancer models to more faithfully recapitulate human solid tumors. We began these experiments in FUS System 2, where there was greater concern of off-target vital organ heating during tFUS—we therefore positioned the tumor on the flank to avoid the complication of heat-related toxicity that may be incurred with orthotopically implanted mammary fat pad tumors. This is not a physiologically relevant position for a breast cancer tumor to growth, and additionally, tumor placement is known to impact tumor growth dynamics. The variable of TNBC tumor placement has been found to impact important variables such as vascular density and capacity to metastasize in TNBC models [198], indicating that angiogenesis and tumor immune infiltrate likely differ in TNBC tumors implanted in the flank compared to in the mammary fat pad. Since pro-angiogenic signaling and tumor immunology are variables of particular interest in this work, implanting these tumors in the mammary fat pad would serve as a more representative model for human breast cancer and is important to consider going forward.

6.1.2 INDUCIBLE TUMOR MODELS

Genetically engineered mouse models (GEMMs) serve as another potential avenue to continue the work showcased in Chapter 3 and Chapter 4. GEMMs are most often initiated by tamoxifen injection, which causes either the inactivation of tumor suppressor genes or activation of oncogenes [199]. This process allows tumor growth to occur through a series of biological steps

much more analogous to human disease as compared to the rapid growth of much more homogenous tumors induced by a bolus injection of cells [200]. This induction timeline is much longer than that for injectable tumors and renders tumor growth in GEMMs much more heterogeneous from mouse to mouse. However, employing GEMMs would better allow us to approximate angiogenesis dynamics and immune infiltrate in our *in vivo* experiments given these models' comparative proximity to human disease. Additionally, many GEMMs are designed to express exogenous antigens or fluorescent tags, which would facilitate the study of antigen release, dendritic cell activation, and lymphatic clearance. Applying the concepts illustrated in Chapters 3 and 4 in GEMMs could allow us to better predict the translatability of the therapeutic regimens we have designed.

6.2 Assessing Effects of Alternative Tumor Normalization Strategies

6.2.1 Vascular Normalization Strategies

Across the studies undertaken in this dissertation, we have explored the concept of tumor vascular normalization alongside two different FUS modalities. Due to a preponderance of extant literature on DC101 and its capacity to modulate tumor vessel properties, we decided to employ it in lieu of other anti-angiogenic drugs. Additionally, DC101 is analogous to a VEGFR2 monoclonal antibody, ramucimurab, which is currently approved for some indications in colorectal cancer, hepatocellular carcinoma, non-small cell lung cancer, and stomach adenocarcinoma [201]. However, other angiogenic drugs are even more widely used in the clinic. A more common anti-angiogenic drug to find in the clinic is bevacizumab, an antibody that binds to VEGF and is currently used in cervical cancer, colorectal cancer, glioblastoma, hepatocellular carcinoma, nonsquamous non-small cell lung cancer, ovarian cancer, and renal cell carcinoma applications [202], and has also been used for vascular normalization in tumors. Outside of monoclonal antibodies—atixinib, a tyrosine kinase inhibitor (TKI) inhibiting VEGFR1 and VEGFR3 tyrosine

kinases [203]; lenvatinib, a TKI that targets all VEGFRs and fibroblast growth factor receptors (FGFRs) [204]; sorafenib, a multi-TKI that targets Braf, VEGFR2, and platelet-derived growth factor receptor-beta (PDGFR-β) [205]; sunitinib, a multi-TKI that targets VEGFR1 and VEGFR2, PDGFR-α and PDGFR-β, KIT, and FLT3 [206]; and vandetanib, a multi-TKI that targets VEGFR2, EGFR, and RET tyrosine kinases [207]—are currently used in the clinic. Despite their lack of target specificity, these TKIs are much less expensive to manufacture than antibody-based therapies, have high oral availability, are less likely to experience steric or convective hindrances when entering tumors due to their smaller size, and have demonstrated capacity for vascular normalization [208], [209], [210], [211], [212], [213]. This combined with the translatability of these drugs makes them interesting candidates for further vascular normalization and FUS research.

6.2.2 Tumor Normalization Strategies

Apart from strategies that target tumor blood vessels to improve delivery, other groups have attempted to improve drug delivery by modulating properties of the tumor stroma. For example, hyaluronidase has been employed to remodel the tumor microenvironment [214], [215], yielding improved nanoparticle delivery following “stromal normalization” [216]. Similarly, another group employed TGB-β blockade in mammary carcinoma models, finding that pericyte coverage and vascular perfusion increased, while the collagen-I content within the tumors decreased, showing evidence of “normalized” stroma [217], in addition to other groups demonstrating tumor normalization following TGB-β blockade [218], [219]. We expect that improving vessel function while also reducing steric barriers in tumors could be highly beneficial for augmenting drug delivery with FUS, and although these approaches depart from the VEGFR2-targeted approach employed in this dissertation, their success in other preclinical studies warrants future investigation.

6.3 Further Refining mFUS Parameters for Drug Delivery

In Chapter 3, we refine mFUS parameters to maximize Gadospin-D delivery in 4T1 tumors. We chose to adjust the parameters of treatment point density and peak-negative pressure (PNP), which are FUS parameters that are commonly tuned to increase drug delivery. However, the FUS parameter space is vast and can be explored far beyond the studies we highlight in this dissertation. Exploring a wider range of PNPs, pulsing and sonication duration, and increasing the number of sonication sessions may further augment the amount of drug delivery within solid tumors.

6.3.1 Refining PNP to Maximize Drug Delivery

First, a wider range of FUS PNPs could be examined to maximize model drug delivery. In this dissertation, we did not test PNPs lower than 0.7 MPa. For context, 0.7 MPa is just above the top of the “safe” preclinical PNP range for blood-brain barrier opening due to the risk of hemorrhaging brain blood vessels [220]. This is less a safety concern for extracranial solid tumor; in fact, we are more concerned with impeding vessel perfusion at this PNP. If vessels are destroyed, they become unable to serve as drug delivery conduits. We expect that this is indeed occurring at the 1 MPa PNP condition, at least at the center of the ultrasound focus. This is likely why drug delivery decreases with FUS compared to passive accumulation in the 1 MPa + high treatment point density treatment condition—it is probable that many blood vessels are being destroyed due to the treatment points being so close to one another. At 1 PNP + low treatment density, there is more space between each treatment points. One effect of this is that FUS PNP drops off beyond the -6 dB focus, resulting in coverage of most of the tumor with a much lower PNP. Treating the tumor at a high treatment point density with a PNP below 0.7 MPa, such as 0.3 or 0.4 MPa, may be employed to achieve similar effects without sacrificing as much vascular function withing the FUS focus. Alternatively, an approach called passive cavitation detection (PCD) monitoring may be employed. This technique is frequently used in BBB opening contexts

and uses live feedback from the transducer to ratchet down the PNP in real time if MBs are cavitating too violently [221], which better accounts for variation between patients [222]. Although the FUS treatment settings using PCD may be more difficult to reproduce, it permits FUS treatments to have a more reproducible effect within an experiment, allowing us to better attribute the drug delivery we observe to effective delivery without as much concern for vessel destruction. Each of these PNP-modifications may be considered going forward to further refine FUS parameters.

6.3.2 Modifying Treatment Duration to Maximize Drug Delivery

Second, pulse length, or the duration of the pulsing sequence when the FUS is “on”; pulse repetition frequency, or the frequency of pulsing sequences; and sonication duration; are all parameters related to treatment time that can alter drug delivery dynamics. Using shorter delays between cycles, or a lower pulse repetition, has been shown to increase contrast agent accumulation in the brain [223], which may translate to success in extracranial tumors. Increasing pulse length was found to increase MRI signal enhancement, with limited benefit as PNP increases from 0.3 to 0.6 MPa [224]. Lengthening sonication duration has also shown to increase MRI signal enhancement, especially up to five minutes [225]; our sonications only last three. These studies underscore the importance of pulse length, pulsing frequency, and sonication duration on MR-visible contrast agents, highlighting their relevance to the tuning of mFUS parameters beyond Chapter 3.

6.3.3 Increasing Sonication Sessions to Maximize Drug Delivery

Finally, the number of sonication sessions may be altered to maximize drug delivery to solid tumors using mFUS. Repeated sonication has become more common in FUS clinical trials [226]—if repeat BBB opening can be safely executed and delivery can be enhanced on multiple days, the prolonged delivery enhancement may confer a clinical benefit. Given our use of

nonfunctional drug in Chapter 3, we only sonicate each tumor once, then measure the signal change as Gadovist or Gadospin-D accumulate in the tumors for about 15 minutes post-sonication. Conditional on parameter optimization to minimize vascular damage, sonicating tumors multiple times concomitant with intravenous drug infusion would be even more beneficial to maximize drug delivery, especially when using a bioactive drug. Taking anti-PD1 immunotherapy as an example, three delivery sessions could be performed, each three days apart given the ~3-day circulating half-life of monoclonal antibodies, which should increase the quantity of anti-PD1 entering the tumor on not just one occasion, but three. To assess whether lasting vascular damage is occurring, perfusion imaging of the tumors could be performed prior to each sonication. As this mFUS + DC101 paradigm is extended past the quantification of model drug, assessing parameters like the number of sonication sessions is essential to maximize treatment effect.

6.4 Better Understanding mFUS Effects on Tumor Vasculature

6.4.1 Assessing Vessel Damage Post-Sonication

We acquire precise spatial and temporal concentration data on intratumoral model drug delivery in Chapter 3. We do not, however, quantify the effects of mFUS on the tumor vasculature, which may be essential to apply this work to drugs which are not model drugs. Since mFUS is known to damage capillaries in the brain at PNPs we employ in Chapter 3, it is important to understand if similar damage is occurring in our 4T1 tumor model post-sonication. Vessel injury could be assessed through a terminal experiment, where tumors are harvested post-sonication and stained to visualize erythrocyte extravasation into the tumor bulk and visible vessel damage. A nonterminal experiment could also be employed—CEUS imaging using a MB injection pre- and post-sonication would provide valuable functional information. If vessels do not reperfuse

following sonication, even if they do not appear damaged by histological readouts, their capacity to permit adequate drug transport during repeated sonications is unlikely.

6.4.2 Assessing Vessel Modulation Post-Sonication

mFUS is also capable of inducing bioeffects that may complement a quantitative increase in drug delivery to tumors. mFUS is known to induce cell adhesion molecule (CAM) expression on endothelial cells, which improves the capacity for leukocytes to extravasate into tumors. Since vascular normalization provides immunological benefits as outlined in Chapter 4, in addition to vascular normalization improving FUS-mediated drug delivery in Chapter 3, it is important to consider additional means by which mFUS may enhance tumor responses to drug delivery. Flow cytometry could be used to identify if CAM expression increases on endothelial cells following mFUS, which may occur in concert with or separately from expected CAM expression increases on tumor vasculature following vascular normalization. This secondary effect is important to consider when using mFUS to enhance biologic drug delivery—measuring CAM expression allows us to isolate another variable that may confound tumor growth data if left unmeasured.

6.5 Biologic Drug Delivery with Vascular Normalization and mFUS

Although we extensively quantify drug delivery concentration and distribution throughout solid tumors in Chapter 3, we do not quantify the biological effects of this augmented delivery using biologic drugs, and FUS parameters that we refine in Chapter 3 may therefore be leveraged to do so. At a basic level, tumor outgrowth could serve as a functional proxy related to the amount of drug delivered post-FUS. Independent of FUS, we know that DC101 synergizes with many drugs to improve drug delivery—however, it is not known if this effect is due to increased accumulation of drug within the tumor, a more favorable immune environment, or some combination of the two. For this reason, it is important to use appropriate methods including

immunoPET or MRI quantification of bioactive drugs to separate the effect of drug delivery from other FUS or DC101-mediated effects on tumor growth.

6.5.1 *IMMUNOPET FOR QUANTIFYING BIOLOGIC DRUG DELIVERY*

To quantify biologic drug delivery in parallel with longitudinal tumor growth tracking, immune-positron emission tomography (immuno-PET). Many groups, including our own, have employed PET imaging to quantify delivery of bioactive drugs labeled with radioisotopes [227], which is essential for nonterminal experiments in solid tumors [228]. Following this quantification, they have tracked tumor outgrowth and survival over time, after which correlation between the dose of drug delivered to the tumor can be calculated to link the quantity of drug delivered to treatment outcomes. Since we observe the greatest synergy between DC101 and mFUS in Chapter 3 when applied to the larger Gadospin-D contrast agent, we expect that employing immuno-PET to quantify antibody delivery would yield the most interesting results. Since EMT6 is only partially responsive to anti-PD1, it would serve as an excellent candidate to evaluate correlation between delivery and growth control. Importantly, radioisotopes of bioactive antibodies can be readily synthesized, which makes immunoPET a more flexible imaging technology compared to MRI, which requires MR-visible contrast agents. Using immunoPET or similar tools could serve as a low-resolution metric to assess drug delivery while concomitantly tracking tumor growth over time.

6.5.2 *T1-MAPPING FOR QUANTIFYING BIOLOGIC DRUG DELIVERY*

MRI T1-mapping could also be integrated with biologic drugs to link quantified drug delivery to treatment outcomes. This tool offers much higher spatial resolution than immuno-PET and is already integrated well with the system we use to administer mFUS. Additionally, IgG antibodies studded with Gadovist (Gad-IgG) have been MR-imaged in the past [229], a model we could employ to conjugate Gadolinium to anti-PD1 molecules, for instance. If designing new drug

delivery vehicles proved prohibitive in the advancement of these projects, Gad-IgG could be administered alongside anti-PD1 during mFUS sonication. Although this is an imperfect system, an IgG molecule should approximate a functional anti-PD1 functional antibody, allowing for simultaneous model drug quantification and functional drug delivery. Separately, smaller molecules are delivered with greater efficacy using nanoparticles, including cisplatin [230], which EMT6 is partially responsive to—iron oxide nanoparticles, whose delivery our group has quantified using MRI T1-mapping, could be used as an MR-visible delivery vehicle carrying cisplatin cargo [231]. Although employing MRI to quantify functional drug delivery may be more technically challenging when it comes to molecule synthesis, our group's expertise in MR imaging leaves to door open to combining MR-imaging of drug delivery with longitudinal tumor growth studies.

6.6 Leveraging Radiomics to Better Understand Dynamics of Model Drug Delivery

Beyond the radiological data that we collect in the Chapter 3 T1-mapping experiments, we have discussed that MR-visible biologic drugs may be leveraged to better understand drug delivery to solid tumors and how delivery heterogeneity impacts treatment outcomes. In the field of radiomics, MR images are acquired and then processed to obtain what are known as MR "features", including descriptive, or "semantic" features, such as shape, size, and vascularity [232]; and mathematically derived, or "agnostic" features, such as skewness, kurtosis, Laplacian transforms, and Haralick textures [232]. We can draw upon many of these semantic features without MRI, but integrating T1-mapping MRI with another MR imaging technique, arterial spin labelling, can permit the acquisition of perfusion data within the same dataset [233]. Agnostic features are higher-order statistical characteristics of MR-images that can draw out differences in voxels or patterns between them [232], which can add nuance to MR data already being acquired in the experiments suggested in Chapter 6.3. By building further data analysis into experiments

where the tumor growth outcome and the quantity of drug delivered are already captured, radiomics analyses may help us better understand why patterns of delivery result in treatment outcomes in ways that were unobservable in the experiments highlighted in Chapter 3, permitting us to correlate delivery and outcome data in novel ways.

6.7 Adaptive Immune Responses Following tFUS and Vascular Normalization

In Chapter 4, we find that tFUS combined with DC101 and anti-PD1 help control primary tumor growth, metastases, improve animal survival, and resist rechallenge in a T cell-dependent manner. This set of observational and mechanistic studies lays out a framework for how tFUS synergizes with immunomodulatory drugs to generate T cell-mediated immunity, especially in the EMT6 tumor model. However, additional experiments may resolve outstanding questions about the adaptive immune mechanisms responsible for the findings outlined in Chapter 4. These include studies probing T cell infiltration and function, antigen release and acquisition by dendritic cells and B lymphocytes, T cell dependence of primary tumor eradication, and abscopal effect.

6.7.1 T cell Infiltration and Function Post-tFUS Combination Therapy

First, although we assess how T cells contribute to long-term immunity in Chapter 4, the direct contribution of infiltrating T cells and their effector function has yet to be explored in the context of this dissertation. It is likely that tFUS ablates many leukocytes within the tumor and that little immune infiltration occurs in the days immediately post-ablation due to thermally induced apoptosis and disruption or destruction of tumor vasculature. However, previous work done by our lab group indicates by day 7 post-thermal ablation, leukocytes are present in the tumor [54], suggesting that this would be a reasonable time point to assess tumor immune infiltrate in the context of Chapter 4. Many treated tumors are quite small at this stage, making it challenging to obtain enough cells from each tumor to run statistical analyses following flow cytometry. However,

if enough cells were able to be isolated from tumors at this time point, we might expect that the number of T cells that can extravasate into the tumor in the DC101 or DC101 + aPD1 ablated groups may be elevated, which could be simply calculated using normalized CD4+Foxp3- and CD8+ T cell counts. Digging deeper, since tFUS is known to liberate tumor debris [234], we expect that CD8 T cells in ablated groups may be more likely to express CD44, an antigen experience-related protein [235], or have higher CD44 geometric mean fluorescence (GMF). Relatedly, we could probe T cell exhaustion and activation using CD44, PD1, and an exhaustion marker like Tim-3 to assess the effector T cells' phenotype. Beyond phenotypic markers, their effector function could also be evaluated by staining for TNF-α and IFN-γ. If tumors were too small to collect enough immune cells, circulating immune cells could be collected and analyzed. Previous studies have shown that post-tFUS and immunotherapy, the share of CD8 T cells that are antigen-experienced may increase in peripheral blood a week or two post-ablation [54], highlighting the potential for repeat blood draws post-ablation to inform the mechanisms behind EMT6 tumor eradication following the combination ablation regimens we designed. Furthermore, these blood draws are nonterminal, allowing us to potentially correlate circulating immune cell data with longer term treatment outcomes. This array of potential flow cytometry experiments would elucidate the phenotype and behavior of intratumoral T cells post-tFUS, an essential step in understanding the immune mechanisms behind the treatment effects we observe in Chapter 4.

6.7.2 Dendritic Cells Post-tFUS Combination Therapy

Second, we do not investigate the effects of tFUS and its combination with DC101 or anti-PD1 on antigen acquisition by dendritic cells (DCs). Often referred to as the bridge between innate and adaptive immunity, probing dendritic cells' interaction with tumor antigen and potential behavioral change based on treatment combination may help us understand the immune underpinnings behind the anti-tumor effects we observe in Chapter 4. Previous studies show that boiling histotripsy, a mechanical form of high-intensity FUS, causes a large increase in antigen

presence in tumor-draining lymph nodes (TDLNs) 1 day post-histotripsy treatment of B16F10-Zsgreen tumors, which abates by 4 days post-histotripsy [186]. An increase in the number and share of dendritic cells that are mature and activated (CD86highMHCIIhigh) was also observed in the histotripsy studies [186], indicating that not only does antigen acquisition occur post-tFUS, but that tFUS also increases DCs' capacity to prompt T cell activation. A separate group similarly found that two days following peritumoral CpG injection and histotripsy or tFUS sonication of EG.7-OVA lymphoma tumors, a greater share of DCs in TDLNs were activated compared to those in non-draining LNs and in sham controls [236]. Although tFUS may denature some tumor antigen as compared to boiling histotripsy, it would be useful to observe whether DC antigen acquisition, maturation, and activation occur to understand the robust response we observe with tFUS combined with DC101 and/or anti-PD1.

6.7.3 B Lymphocytes Post-tFUS Combination Therapy

Third, another cell type we do not assess in Chapter 4 are B lymphocytes, or B cells. This lymphocyte subset has a wide range of potential functions, including antigen acquisition, presentation, T cell activation, antibody production, and anti-cancer cytotoxicity. B cells are activated either through helper T cells' binding to B cells CD40 protein or by large antigen fragments [237]. Like DCs, B cells can also acquire antigen and present it to T cells, which can yield T cell activation [238]. Additionally, B cells produce antigen-specific antibodies—if this antigen is present on a cancer cell's cell membrane, the antibody can bind to it and mark it for cell death [239]. B cells can also produce cytokines like granzymes that can themselves induce cancer cell death [239].

B cells are an understudied lymphocyte population in the development of immunotherapies, a trend that extends to focused ultrasound immunomodulation. However, although they do not study the impact of B cells, some preclinical and preclinical studies do observe changes in B cells post-sonication. Our lab group has observed that a day post-

histotripsy treatment of B16F10-Zsgreen tumors, the number of B cells in TDLNs that have taken up tumor antigen compared to sham control mice markedly increases [186]. Similarly, 1-2 weeks post thermal ablation of human breast tumors, histological samples have a much higher number of intratumoral B cells than control tumors [240]. Although we have not measured B cells in our studies, we expect that if antigen is being released and acquired by DCs in TDLNs, the same is likely true for B cells. Flow cytometry assays could be used to evaluate antigen acquisition post-tFUS in addition to measuring B cell activation markers, both of which may help us better understand the development of adaptive immunity post-tFUS combination therapy.

6.7.4 Mechanisms of Tumor Eradication Post-tFUS Combination Therapy

Fourth, although we test the T cell dependence of secondary rechallenge in Chapter 4, we do not test the T cell dependence of primary tumor eradication. Therefore, performing CD4 and CD8 depletions soon after tFUS would help answer an essential question: through what mechanisms does tFUS combined with DC101 and anti-PD1 eradicate EMT6 tumors? The clearest, most linear hypothesis is that that long-term T cell-dependent immunity stems from a T cell-dependent response against the primary tumor. In this case, now-activated dendritic cells expose effector T cells to tumor antigen, followed by T cell infiltration of tumors and killing of cancer cells. Another possibility is that the acquisition of tumor antigen occurs separately from primary tumor eradication. Although we establish that our tFUS ablation is partial, the tFUS regimen we employ may debulk the tumor sufficiently to cause its eradication, which could plausibly occur in parallel with an increase antigen acquisition by DCs post-tFUS. T cells could thus be exposed to antigen by DCs, resulting in the formation of long-term T cell memory. Yet another possibility is incomplete T cell depletion—antibody depletion has been found to incompletely deplete tissue-resident memory cells [183], [241], which may also be the case for tumors whose vasculature is no longer highly functional. In this case, although circulating T cells may be depleted, anti-CD4 and anti-CD8 may not be able to reach T cells within the tumor,

resulting in their persistence and contribution to lasting anti-tumor immunity. There are many mechanisms that may link the primary tumor eradication and T cell-dependent rechallenge rejection we observe, and better understanding the connection between the two will inform the implementation of tFUS-based therapies going forward.

6.7.5 Abscopal Effect Post-tFUS Combination Therapy

Finally, we do not evaluate the effects of DC101 + anti-PD1 + tFUS on distal EMT6 tumors. This is important to explore given that most patients with solid tumors do not die from primary tumor complications, but from metastases [242]. Using a rechallenge model to assess long-term immune responses is a useful mechanistic exercise but does not directly address how anti-tumor immunity would combat metastatic spread or growth. We do evaluate metastasis in the 4T1 model after treating with DC101 + tFUS, where we find that this combination results in a trending decrease in lung metastasis—however, EMT6 tumors do not readily metastasize. This leaves two options to test whether DC101 + anti-PD1 followed by the sonication of a primary tumor can control an unsonicated tumor: a secondary, subcutaneous tumor, or induced lung metastasis. Importantly, these two models would yield distinct outputs. Measuring the growth of a secondary, subcutaneous tumor is straightforward and could be tracked in parallel with the primary, sonicated tumor. Despite the ease of this approach, most metastases in humans are much smaller than their primary tumor at the time of treatment, so inoculating two tumors at once in a mouse and sonicating one does not represent a commonly occurring human cancer condition. Additionally, most human TNBC metastasis does not occur in or beneath the skin. A secondary subcutaneous tumor could be induced after the primary tumor, but the timing of the secondary tumor's inoculation would require optimization, as its size and a mounting immune response with the injection of DC101 + aPD1 may result in the secondary tumor not growing at all. The other secondary tumor approach would involve an intravenous injection of EMT6 cells into the mouse already bearing the primary tumor, which is known to yield lung metastases [243]. This model

would better recapitulate the common clinical condition of lung metastases in human TNBC patients [244], but would also require either the euthanasia of animals to measure metastases at a given time point, or the use of survival data, since the secondary tumor would be challenging to measure while the animal is alive. Whichever the method, asking whether the treatment combinations we devise in Chapter 4 induce abscopal control of distal, unsonicated tumors is worth pursuing and would be enlightening for future clinical translation.

6.5 Innate Immune Responses Following tFUS and Vascular Normalization

While focusing heavily on the adaptive immune response to tFUS combination therapy in Chapter 4, the innate immune response is not to be ignored. Innate immune cells, particularly myeloid-derived suppressor cells (MDSCs), make up a large fraction of the tumor immune infiltrate, and often promote immunosuppression within tumors. Although adaptive immunity is necessary to induce long-term anti-tumor responses in the therapeutic regimens we designed, cells like MDSCs, tumor-associated macrophages, and natural killer cells may also be involved in the response to tFUS combination therapy.

6.8.1 Myeloid-Derived Suppressor Cells Post-tFUS Combination Therapy

MDSCs are a highly prevalent immunosuppressive innate immune cell in 4T1 and EMT6 tumors [245]. They are thus an important part of the tumor immune environment and are responsible for significant immunosuppression. Eliminating intratumoral MDSCs with gemcitabine in combination with tFUS has proven effective at driving long-term tumor control and survival 4T1 tumors [54], underscoring the importance of addressing this cell type in immunotherapeutic interventions.

Ablation of immunosuppressive MDSCs may occur following tFUS, as MDSCs have been shown to be sensitive to hyperthermia [246]. Interestingly, other groups have

demonstrated that tFUS increases the number of MDSCs at distal tumor sites 3 and 7 days post-sonication [55], indicating that the inflammatory response initiated by tFUS may actually increase MDSC recruitment in the long term. However, even temporarily eliminating a large share of MDSCs via tFUS may alleviate immunosuppression in the tumor, permitting intratumoral T cells to better carry out their effector function. One might hypothesize that MDSC ablation would increase the efficacy of anti-PD1 due to a likely reduction in immunosuppression, but since we did not observe synergy between tFUS and anti-PD1 in Chapter 4, this may be an unlikely hypothesis. However, this may be a function of anti-PD1 dosing timing, so this hypothesis cannot be discounted.

MDSCs also thrive in hypoxic environments, a characteristic typical of solid tumors that DC101 often reduces. In fact, hypoxia is known to increase the immunosuppressive capacity of MDSCs [72], which can be reversed upon exposure to normoxic conditions and vascular normalization [71]. If DC101 is improving intratumoral oxygenation in our experiments, one reason for synergy between tFUS and DC101 may lie in a mitigation of MDSCs' immunosuppressive effects upon effector T cells. This could be measured by PD-L1 expression, CD39 and CD73 expression, and IL-10 and IFN-γ production by MDSCs, all of which are involved with MDSC immunosuppression of T cells [247].

6.8.2 Tumor-Associated Macrophages Post-tFUS Combination Therapy

Tumor-associated macrophages (TAMs) are another key myeloid cell subset within tumors that can either contribute to cancer cell-killing or suppression of effector T cell function, depending on their polarization [248]. Although TAMs' response to tFUS has not been observed in many publications, one set of studies has shown that FUS hyperthermia can polarize TAMs to a more anti-tumor phenotype [249]. Additionally, hypoxia has been found to polarize anti-tumor TAMs and MDSCs into pro-tumor TAMs, resulting in greater immunosuppression [250]—through normalizing oxygen levels in the tumor, DC101 may reduce this unfavorable TAM

polarization. Similarly, MDSCs have been shown to make TAMs more immunosuppressive. Assessing the number of CD11b+F4/80+ TAMs that produce IL-10, Arginase 1, and express PD-L1 by flow cytometry may elucidate the role of TAMs in immunosuppression following tFUS. Resulting changes in TAM phenotype by agents used in the DC101 + tFUS combination group may partially explain the synergy we observe between the two therapeutics.

6.8.3 Natural Killer Cells Post-tFUS Combination Therapy

When activated, natural killer (NK) cells promote tumor cell death by producing cytokines like perforin and granzymes. This innate immune cell type makes up small percentage of all intratumoral immune cells, but tFUS has been shown to both increase the number of NK cells in the spleen and TDLN post-sonication [251], in addition to tFUS increasing the number of NK cells in ablated breast cancer 7-14 days post-ablation in human patients [252]. Separately, NK cell infiltration has been shown to increase in clinical trials following tFUS. Since IFN-γ, IL-2, and IL-12 production can be increased post-sonication [253], [254], [255], [256] and can promote NK cells activation and proliferation [257], tFUS may augment NK cell activity through these mechanisms. DAMP production is known to increase post-tFUS, but it is not known DAMPs affect DC activity. Although we currently know little about the contribution of NK cells to immune responses to tFUS, better understanding how this important immune cell type interacts with tFUS may be essential to mechanistically uncovering how tFUS synergizes with immunotherapy.

6.4 Summary

In this dissertation we design novel treatment paradigms that combine DC101, a clinical drug analog, with two different FUS modalities. We establish that vascular normalization synergizes both mFUS and tFUS, allowing us to more effectively deliver drugs and augment the efficacy of immunotherapy in solid tumors. Future experiments will improve our understanding of

the mechanisms behind this impactful work and move our preclinical research closer treatment that can impact human patients.

REFERENCES

[1] "Cancer deaths - Health, United States." Accessed: Mar. 09, 2025. [Online]. Available: https://www.cdc.gov/nchs/hus/topics/cancer-deaths.htm

[2] "Common Cancer Sites — Cancer Stat Facts." Accessed: Mar. 09, 2025. [Online]. Available: https://seer.cancer.gov/statfacts/html/common.html

[3] I. A. Khawar, J. H. Kim, and H. J. Kuh, "Improving drug delivery to solid tumors: Priming the tumor microenvironment," *Journal of Controlled Release*, vol. 201, pp. 78–89, Mar. 2015, doi: 10.1016/J.JCONREL.2014.12.018.

[4] Y. Tie, F. Tang, Y. quan Wei, and X. wei Wei, "Immunosuppressive cells in cancer: mechanisms and potential therapeutic targets," *Journal of Hematology & Oncology 2022 15:1*, vol. 15, no. 1, pp. 1–33, May 2022, doi: 10.1186/S13045-022-01282-8.

[5] R. K. Jain and E. L. Steele, "A New Target for Tumor Therapy," *N Engl J Med*, vol. 360, no. 25, p. 2669, Jun. 2009, doi: 10.1056/NEJMCIBR0902054.

[6] "Treatment of Triple-negative Breast Cancer | Treatment of TNBC | American Cancer Society." Accessed: Mar. 09, 2025. [Online]. Available: https://www.cancer.org/cancer/types/breast-cancer/treatment/treatment-of-triple-negative.html

[7] C. Diez de los Rios de la Serna, C. B. Boers-Doets, T. Wiseman, B. Radia, and R. Hammond, "Early Recognition and Management of Side Effects Related to Systemic Anticancer Therapy for Advanced Breast Cancer," *Semin Oncol Nurs*, vol. 40, no. 1, p. 151553, Feb. 2024, doi: 10.1016/J.SONCN.2023.151553.

[8] L. Zhong *et al.*, "Small molecules in targeted cancer therapy: advances, challenges, and future perspectives," *Signal Transduction and Targeted Therapy 2021 6:1*, vol. 6, no. 1, pp. 1–48, May 2021, doi: 10.1038/s41392-021-00572-w.

[9] K. C. Valkenburg, A. E. De Groot, and K. J. Pienta, "Targeting the tumour stroma to improve cancer therapy," *Nat Rev Clin Oncol*, vol. 15, no. 6, p. 366, Jun. 2018, doi: 10.1038/S41571-018-0007-1.

[10] M. W. Dewhirst and T. W. Secomb, "Transport of drugs from blood vessels to tumour tissue," *Nat Rev Cancer*, vol. 17, no. 12, p. 738, Dec. 2017, doi: 10.1038/NRC.2017.93.

[11] G. Planes-Laine *et al.*, "PD-1/PD-L1 Targeting in Breast Cancer: The First Clinical Evidences are Emerging—A Literature Review," *Cancers 2019, Vol. 11, Page 1033*, vol. 11, no. 7, p. 1033, Jul. 2019, doi: 10.3390/CANCERS11071033.

[12] J. Galon and D. Bruni, “Approaches to treat immune hot, altered and cold tumours with combination immunotherapies,” *Nature Reviews Drug Discovery 2018 18:3*, vol. 18, no. 3, pp. 197–218, Jan. 2019, doi: 10.1038/s41573-018-0007-y.

[13] S. Maleki Vareki, “High and low mutational burden tumors versus immunologically hot and cold tumors and response to immune checkpoint inhibitors,” *J Immunother Cancer*, vol. 6, no. 1, pp. 1–5, Dec. 2018, doi: 10.1186/S40425-018-0479-7/FIGURES/1.

[14] P. Guha, K. R. Heatherton, K. P. O’connell, I. S. Alexander, and S. C. Katz, “Assessing the Future of Solid Tumor Immunotherapy,” *Biomedicines*, vol. 10, no. 3, p. 655, Mar. 2022, doi: 10.3390/BIOMEDICINES10030655.

[15] R. Park, L. Lopes, C. R. Cristancho, I. M. Riano, and A. Saeed, “Treatment-Related Adverse Events of Combination Immune Checkpoint Inhibitors: Systematic Review and Meta-Analysis,” *Front Oncol*, vol. 10, p. 258, Mar. 2020, doi: 10.3389/FONC.2020.00258.

[16] D. Wu, Q. Chen, X. Chen, F. Han, Z. Chen, and Y. Wang, “The blood–brain barrier: Structure, regulation and drug delivery,” *Signal Transduction and Targeted Therapy 2023 8:1*, vol. 8, no. 1, pp. 1–27, May 2023, doi: 10.1038/s41392-023-01481-w.

[17] C. M. Gorick *et al.*, “Applications of focused ultrasound-mediated blood-brain barrier opening,” *Adv Drug Deliv Rev*, vol. 191, p. 114583, Dec. 2022, doi: 10.1016/J.ADDR.2022.114583.

[18] A. Burgess, K. Shah, O. Hough, and K. Hynynen, “Focused ultrasound-mediated drug delivery through the blood-brain barrier,” *Expert Rev Neurother*, vol. 15, no. 5, p. 477, May 2015, doi: 10.1586/14737175.2015.1028369.

[19] K. F. Timbie, B. P. Mead, and R. J. Price, “Drug and Gene Delivery Across the Blood-Brain Barrier with Focused Ultrasound,” *J Control Release*, vol. 219, p. 61, Dec. 2015, doi: 10.1016/J.JCONREL.2015.08.059.

[20] A. Abrahao *et al.*, “First-in-human trial of blood–brain barrier opening in amyotrophic lateral sclerosis using MR-guided focused ultrasound,” *Nature Communications 2019 10:1*, vol. 10, no. 1, pp. 1–9, Sep. 2019, doi: 10.1038/s41467-019-12426-9.

[21] A. R. Rezai *et al.*, “Focused ultrasound–mediated blood-brain barrier opening in Alzheimer’s disease: long-term safety, imaging, and cognitive outcomes,” *J Neurosurg*, vol. 139, no. 1, pp. 275–283, Nov. 2022, doi: 10.3171/2022.9.JNS221565.

[22] “Study Details | Safety of BBB Opening With the SonoCloud | ClinicalTrials.gov.” Accessed: Mar. 18, 2024. [Online]. Available: https://clinicaltrials.gov/study/NCT02253212

[23] A. Carpentier *et al.*, “Repeated blood–brain barrier opening with a nine-emitter implantable ultrasound device in combination with carboplatin in recurrent glioblastoma: a phase I/II clinical trial,” *Nature Communications 2024 15:1*, vol. 15, no. 1, pp. 1–12, Feb. 2024, doi: 10.1038/s41467-024-45818-7.

[24] H. Hashizume *et al.*, “Openings between Defective Endothelial Cells Explain Tumor Vessel Leakiness,” *Am J Pathol*, vol. 156, no. 4, p. 1363, 2000, doi: 10.1016/S0002-9440(10)65006-7.

[25] H. F. Dvorak, J. A. Nagy, J. T. Dvorak, and A. M. Dvorak, “Identification and characterization of the blood vessels of solid tumors that are leaky to circulating macromolecules,” *Am J Pathol*, vol. 133, no. 1, p. 95, 1988, Accessed: Mar. 09, 2025. [Online]. Available: https://pmc.ncbi.nlm.nih.gov/articles/PMC1880651/

[26] T. Stylianopoulos, J. D. Martin, M. Snuderl, F. Mpekris, S. R. Jain, and R. K. Jain, “Coevolution of solid stress and interstitial fluid pressure in tumors during progression: Implications for vascular collapse,” *Cancer Res*, vol. 73, no. 13, pp. 3833–3841, Jul. 2013, doi: 10.1158/0008-5472.CAN-12-4521/651152/AM/CO-EVOLUTION-OF-SOLID-STRESS-AND-INTERSTITIAL.

[27] O. Trédan, C. M. Galmarini, K. Patel, and I. F. Tannock, “Drug resistance and the solid tumor microenvironment,” *J Natl Cancer Inst*, vol. 99, no. 19, pp. 1441–1454, Oct. 2007, doi: 10.1093/JNCI/DJM135.

[28] R. Margolis, L. Basavarajappa, J. Li, G. Obaid, and K. Hoyt, “Image-guided focused ultrasound-mediated molecular delivery to breast cancer in an animal model,” *Phys Med Biol*, vol. 68, no. 15, pp. 10.1088/1361-6560/ace23d, Aug. 2023, doi: 10.1088/1361-6560/ACE23D.

[29] S. Lee *et al.*, “Preclinical study to improve microbubble-mediated drug delivery in cancer using an ultrasonic probe with an interchangeable acoustic lens,” *Scientific Reports 2021 11:1*, vol. 11, no. 1, pp. 1–10, Jun. 2021, doi: 10.1038/s41598-021-92097-z.

[30] S. Snipstad *et al.*, “Ultrasound Improves the Delivery and Therapeutic Effect of Nanoparticle-Stabilized Microbubbles in Breast Cancer Xenografts,” *Ultrasound Med Biol*, vol. 43, no. 11, pp. 2651–2669, Nov. 2017, doi: 10.1016/J.ULTRASMEDBIO.2017.06.029.

[31] E. M. Knavel and C. L. Brace, “Tumor ablation: Common modalities and general practices,” Dec. 2013. doi: 10.1053/j.tvir.2013.08.002.

[32] A. S. Hatzfeld-Charbonnier *et al.*, “Influence of heat stress on human monocyte-derived dendritic cell functions with immunotherapeutic potential for antitumor vaccines,” *J Leukoc Biol*, vol. 81, no. 5, p. 1179, May 2007, doi: 10.1189/JLB.0506347.

[33] T. A. Mace, L. Zhong, K. M. Kokolus, and E. A. Repasky, “Effector CD8+ T cell IFN-γ production and cytotoxicity are enhanced by mild hyperthermia,” *International Journal of Hyperthermia*, vol. 28, no. 1, p. 9, Feb. 2012, doi: 10.3109/02656736.2011.616182.

[34] M. Yu *et al.*, “Microwave ablation of primary breast cancer inhibits metastatic progression in model mice via activation of natural killer cells,” *Cell Mol Immunol*, vol. 18, no. 9, p. 2153, Sep. 2020, doi: 10.1038/S41423-020-0449-0.

[35] W. Xiao *et al.*, “The CXCL10/CXCR3 Pathway Contributes to the Synergy of Thermal Ablation and PD-1 Blockade Therapy against Tumors,” *Cancers (Basel)*, vol. 15, no. 5, p. 1427, Mar. 2023, doi: 10.3390/CANCERS15051427/S1.

[36] K. Lemdani *et al.*, “Therapeutic and cytotoxic responses after radiofrequency ablation combined to in situ immunomodulation and PD1 blockade in colorectal cancer.,” *Journal of Clinical Oncology*, vol. 36, no. 15_suppl, pp. e15562–e15562, May 2018, doi: 10.1200/JCO.2018.36.15_SUPPL.E15562.

[37] Y. Wu *et al.*, “Cryoablation reshapes the immune microenvironment in the distal tumor and enhances the anti-tumor immunity,” *Front Immunol*, vol. 13, p. 930461, Aug. 2022, doi: 10.3389/FIMMU.2022.930461/FULL.

[38] E. Domingo-Musibay *et al.*, “Endogenous Heat-Shock Protein Induction with or Without Radiofrequency Ablation or Cryoablation in Patients with Stage IV Melanoma,” *Oncologist*, vol. 22, no. 9, pp. 1026-e93, Sep. 2017, doi: 10.1634/THEONCOLOGIST.2017-0060.

[39] X. Guo *et al.*, “Immunological effect of irreversible electroporation on hepatocellular carcinoma,” *BMC Cancer*, vol. 21, no. 1, Dec. 2021, doi: 10.1186/S12885-021-08176-X.

[40] R. Nuccitelli, J. C. Berridge, Z. Mallon, M. Kreis, B. Athos, and P. Nuccitelli, “Nanoelectroablation of Murine Tumors Triggers a CD8-Dependent Inhibition of Secondary Tumor Growth,” *PLoS One*, vol. 10, no. 7, Jul. 2015, doi: 10.1371/JOURNAL.PONE.0134364.

[41] R. J. E. van den Bijgaart, D. C. Eikelenboom, M. Hoogenboom, J. J. Fütterer, M. H. den Brok, and G. J. Adema, “Thermal and mechanical high-intensity focused ultrasound: perspectives on tumor ablation, immune effects and combination strategies,” *Cancer Immunol Immunother*, vol. 66, no. 2, p. 247, Feb. 2016, doi: 10.1007/S00262-016-1891-9.

[42] Y. Zhang, J. Deng, J. Feng, and F. Wu, “Enhancement of antitumor vaccine in ablated hepatocellular carcinoma by high-intensity focused ultrasound,” *World Journal of Gastroenterology : WJG*, vol. 16, no. 28, p. 3584, Jul. 2010, doi: 10.3748/WJG.V16.I28.3584.

[43] J. Z. Xia, F. L. Xie, L. F. Ran, X. P. Xie, Y. M. Fan, and F. Wu, “High-intensity focused ultrasound tumor ablation activates autologous tumor-specific cytotoxic T lymphocytes,” *Ultrasound Med Biol*, vol. 38, no. 8, pp. 1363–1371, Aug. 2012, doi: 10.1016/J.ULTRASMEDBIO.2012.03.009.

[44] Z. Hu *et al.*, “Release of endogenous danger signals from HIFU-treated tumor cells and their stimulatory effects on APCs,” *Biochem Biophys Res Commun*, vol. 335, no. 1, p. 124, Sep. 2005, doi: 10.1016/J.BBRC.2005.07.071.

[45] D. E. Kruse, M. A. Mackanos, C. E. O'Connell-Rodwell, C. H. Contag, and K. W. Ferrara, "Short-duration Focused Ultrasound Stimulation of Hsp70 Expression In Vivo," *Phys Med Biol*, vol. 53, no. 13, p. 3641, Jul. 2008, doi: 10.1088/0031-9155/53/13/017.

[46] R. J. E. van den Bijgaart, D. C. Eikelenboom, M. Hoogenboom, J. J. Fütterer, M. H. den Brok, and G. J. Adema, "Thermal and mechanical high-intensity focused ultrasound: perspectives on tumor ablation, immune effects and combination strategies," *Cancer Immunology, Immunotherapy*, vol. 66, no. 2, pp. 247–258, Feb. 2017, doi: 10.1007/S00262-016-1891-9/TABLES/2.

[47] A. De Maio, G. Alfieri, M. Mattone, P. Ghanouni, and A. Napoli, "High-Intensity Focused Ultrasound Surgery for Tumor Ablation: A Review of Current Applications," *Radiol Imaging Cancer*, vol. 6, no. 1, Jan. 2024, doi: 10.1148/RYCAN.230074/ASSET/IMAGES/LARGE/RYCAN.230074.TBL1.JPEG.

[48] H. D. Do *et al.*, "Combination of thermal ablation by focused ultrasound, pFAR4-IL-12 transfection and lipidic adjuvant provide a distal immune response," *Explor Target Antitumor Ther*, vol. 3, no. 6, p. 398, 2022, doi: 10.37349/ETAT.2022.00090.

[49] R. Yang *et al.*, "Effects of high-intensity focused ultrasound in the treatment of experimental neuroblastoma," *J Pediatr Surg*, vol. 27, no. 2, pp. 246–251, Feb. 1992, doi: 10.1016/0022-3468(92)90321-W.

[50] N. D. Sheybani, A. R. Witter, E. A. Thim, H. Yagita, T. N. J. Bullock, and R. J. Price, "Combination of thermally ablative focused ultrasound with gemcitabine controls breast cancer via adaptive immunity," *J Immunother Cancer*, vol. 8, no. 2, p. e001008, Aug. 2020, doi: 10.1136/JITC-2020-001008.

[51] W. Hundt, C. E. O'Connell-Rodwell, M. D. Bednarski, S. Steinbach, and S. Guccione, "In Vitro Effect of Focused Ultrasound or Thermal Stress on HSP70 Expression and Cell Viability in Three Tumor Cell Lines," *Acad Radiol*, vol. 14, no. 7, pp. 859–870, Jul. 2007, doi: 10.1016/j.acra.2007.04.008.

[52] Z. Hu *et al.*, "Release of endogenous danger signals from HIFU-treated tumor cells and their stimulatory effects on APCs," *Biochem Biophys Res Commun*, vol. 335, no. 1, pp. 124–131, Sep. 2005, doi: 10.1016/j.bbrc.2005.07.071.

[53] F. Wu *et al.*, "Expression of tumor antigens and heat-shock protein 70 in breast cancer cells after high-intensity focused ultrasound ablation," *Ann Surg Oncol*, vol. 14, no. 3, pp. 1237–1242, Mar. 2007, doi: 10.1245/s10434-006-9275-6.

[54] N. D. Sheybani, A. R. Witter, E. A. Thim, H. Yagita, T. N. J. Bullock, and R. J. Price, "Combination of thermally ablative focused ultrasound with gemcitabine controls breast cancer via adaptive immunity," *J Immunother Cancer*, vol. 8, no. 2, pp. 1–15, 2020, doi: 10.1136/jitc-2020-001008.

[55] B. Z. Fite *et al.*, “Immune modulation resulting from MR-guided high intensity focused ultrasound in a model of murine breast cancer,” *Sci Rep*, vol. 11, no. 1, p. 927, Dec. 2021, doi: 10.1038/S41598-020-80135-1.

[56] M. T. Silvestrini *et al.*, “Priming is key to effective incorporation of image-guided thermal ablation into immunotherapy protocols,” *JCI Insight*, vol. 2, no. 6, p. e90521, 2017, doi: 10.1172/jci.insight.90521.

[57] X. Han *et al.*, “In situ thermal ablation of tumors in combination with nano-adjuvant and immune checkpoint blockade to inhibit cancer metastasis and recurrence,” *Biomaterials*, vol. 224, Dec. 2019, doi: 10.1016/j.biomaterials.2019.119490.

[58] H. Hashizume *et al.*, “Openings between defective endothelial cells explain tumor vessel leakiness,” *Am J Pathol*, vol. 156, no. 4, pp. 1363–1380, 2000, doi: 10.1016/S0002-9440(10)65006-7.

[59] D. J. Hicklin and L. M. Ellis, “Role of the vascular endothelial growth factor pathway in tumor growth and angiogenesis,” *Journal of Clinical Oncology*, vol. 23, no. 5, pp. 1011–1027, Sep. 2005, doi: 10.1200/JCO.2005.06.081/ASSET/IMAGES/JCO06081F03.JPEG.

[60] E. Fakhrejahani and M. Toi, “Tumor Angiogenesis: Pericytes and Maturation Are Not to Be Ignored,” *J Oncol*, vol. 2012, p. 261750, 2011, doi: 10.1155/2012/261750.

[61] R. K. Jain, “Transport of molecules across tumor vasculature,” *Cancer Metastasis Rev*, vol. 6, no. 4, pp. 559–593, Dec. 1987, doi: 10.1007/BF00047468.

[62] M. W. Dewhirst and T. W. Secomb, “Transport of drugs from blood vessels to tumour tissue,” *Nat Rev Cancer*, vol. 17, no. 12, p. 738, Dec. 2017, doi: 10.1038/NRC.2017.93.

[63] R. K. Jain, “Normalization of tumor vasculature: An emerging concept in antiangiogenic therapy,” *Science (1979)*, vol. 307, no. 5706, pp. 58–62, 2005, doi: 10.1126/science.1104819.

[64] A. R. Pries *et al.*, “Structural Adaptation and Heterogeneity of Normal and Tumor Microvascular Networks,” *PLoS Comput Biol*, vol. 5, no. 5, p. e1000394, 2009, doi: 10.1371/JOURNAL.PCBI.1000394.

[65] J. W. Baish *et al.*, “Scaling rules for diffusive drug delivery in tumor and normal tissues,” *Proc Natl Acad Sci U S A*, vol. 108, no. 5, pp. 1799–1803, Feb. 2011, doi: 10.1073/PNAS.1018154108/SUPPL_FILE/PNAS.1018154108_SI.PDF.

[66] A. Vito, N. El-Sayes, and K. Mossman, “Hypoxia-Driven Immune Escape in the Tumor Microenvironment,” *Cells*, vol. 9, no. 4, pp. 1–20, 2020, doi: 10.3390/cells9040992.

[67] M. Bourhis, J. Palle, I. Galy-Fauroux, and M. Terme, “Direct and Indirect Modulation of T Cells by VEGF-A Counteracted by Anti-Angiogenic Treatment,” *Front Immunol*, vol. 12, Mar. 2021, doi: 10.3389/FIMMU.2021.616837.

[68] J. R. Byrnes *et al.*, “Hypoxia Is a Dominant Remodeler of the Effector T Cell Surface Proteome Relative to Activation and Regulatory T Cell Suppression,” *Mol Cell Proteomics*, vol. 21, no. 4, p. 100217, Apr. 2022, doi: 10.1016/J.MCPRO.2022.100217.

[69] P. P. Cunha *et al.*, “Oxygen levels at the time of activation determine T cell persistence and immunotherapeutic efficacy,” *Elife*, vol. 12, May 2023, doi: 10.7554/ELIFE.84280.

[70] K. Mimura, K. Kono, A. Takahashi, Y. Kawaguchi, and H. Fujii, “Vascular endothelial growth factor inhibits the function of human mature dendritic cells mediated by VEGF receptor-2,” *Cancer Immunology, Immunotherapy*, vol. 56, no. 6, pp. 761–770, 2007, doi: 10.1007/s00262-006-0234-7.

[71] Y. Zhang *et al.*, “VEGFR2 activity on myeloid cells mediates immune suppression in the tumor microenvironment,” *JCI Insight*, vol. 6, no. 23, 2021, doi: 10.1172/jci.insight.150735.

[72] C. A. Corzo *et al.*, “HIF-1α regulates function and differentiation of myeloid-derived suppressor cells in the tumor microenvironment,” *Journal of Experimental Medicine*, vol. 207, no. 11, pp. 2439–2453, 2010, doi: 10.1084/jem.20100587.

[73] I. Kim, S. O. Moon, S. H. Kim, H. J. Kim, Y. S. Koh, and G. Y. Koh, “Vascular Endothelial Growth Factor Expression of Intercellular Adhesion Molecule 1 (ICAM-1), Vascular Cell Adhesion Molecule 1 (VCAM-1), and E-selectin through Nuclear Factor-κB Activation in Endothelial Cells,” *Journal of Biological Chemistry*, vol. 276, no. 10, pp. 7614–7620, 2001, doi: 10.1074/jbc.M009705200.

[74] M. B. Lawrence, G. S. Kansas, E. J. Kunkel, and K. Ley, “Threshold levels of fluid shear promote leukocyte adhesion through selectins (CD62L,P,E) [published erratum appears in J Cell Biol 1997 Apr 7;137(1):261],” *J Cell Biol*, vol. 136, no. 3, pp. 717–727, 1997.

[75] S. Rollin *et al.*, “VEGF-mediated endothelial P-selectin translocation: Role of VEGF receptors and endogenous PAF synthesis,” *Blood*, vol. 103, no. 10, pp. 3789–3797, 2004, doi: 10.1182/blood-2003-07-2272.

[76] S. C. Tromp *et al.*, “Tumor angiogenesis factors reduce leukocyte adhesion in vivo,” *Int Immunol*, vol. 12, no. 5, pp. 671–676, 2000, doi: 10.1093/intimm/12.5.671.

[77] A. E. M. Dirkx *et al.*, “Tumor angiogenesis modulates leukocyte-vessel wall interactions in Vivo by reducing endothelial adhesion molecule expression,” *Cancer Res*, vol. 63, no. 9, pp. 2322–2329, 2003.

[78] Z. R. Huinen, E. J. M. Huijbers, J. R. van Beijnum, P. Nowak-Sliwinska, and A. W. Griffioen, “Anti-angiogenic agents — overcoming tumour endothelial cell anergy and improving immunotherapy outcomes,” *Nat Rev Clin Oncol*, vol. 18, no. 8, pp. 527–540, 2021, doi: 10.1038/s41571-021-00496-y.

[79] F. Winkler *et al.*, “Kinetics of vascular normalization by VEGFR2 blockade governs brain tumor response to radiation: Role of oxygenation, angiopoietin-1, and matrix

metalloproteinases," *Cancer Cell*, vol. 6, no. 6, pp. 553–563, Dec. 2004, doi: 10.1016/J.CCR.2004.10.011/ATTACHMENT/F4453261-250F-4E35-9361-A1BE10F7C938/MMC1.PDF.

[80] R. K. Jain, R. T. Tong, and L. L. Munn, "Effect of Vascular Normalization by Antiangiogenic Therapy on Interstitial Hypertension, Peritumor Edema, and Lymphatic Metastasis: Insights from a Mathematical Model," *Cancer Res*, vol. 67, no. 6, pp. 2729–2735, Mar. 2007, doi: 10.1158/0008-5472.CAN-06-4102.

[81] R. T. Tong, Y. Boucher, S. V. Kozin, F. Winkler, D. J. Hicklin, and R. K. Jain, "Vascular Normalization by Vascular Endothelial Growth Factor Receptor 2 Blockade Induces a Pressure Gradient Across the Vasculature and Improves Drug Penetration in Tumors," *Cancer Res*, vol. 64, no. 11, pp. 3731–3736, Jun. 2004, doi: 10.1158/0008-5472.CAN-04-0074.

[82] Y. Huang, T. Stylianopoulos, D. G. Duda, D. Fukumura, and R. K. Jain, "Benefits of vascular normalization are dose- and time-dependent," *Cancer Res*, vol. 73, no. 23, pp. 7144–7146, Dec. 2013, doi: 10.1158/0008-5472.CAN-13-1989.

[83] J. Garcia *et al.*, "Bevacizumab (Avastin®) in cancer treatment: A review of 15 years of clinical experience and future outlook," *Cancer Treat Rev*, vol. 86, p. 102017, Jun. 2020, doi: 10.1016/J.CTRV.2020.102017.

[84] R. N. Gacche, "Compensatory angiogenesis and tumor refractoriness," *Oncogenesis 2015 4:6*, vol. 4, no. 6, pp. e153–e153, Jun. 2015, doi: 10.1038/oncsis.2015.14.

[85] F. M. Iwamoto *et al.*, "Patterns of relapse and prognosis after bevacizumab failure in recurrent glioblastoma," *Neurology*, vol. 73, no. 15, p. 1200, 2009, doi: 10.1212/WNL.0B013E3181BC0184.

[86] S. Goel, H.-K. Wong, and R. K. Jain, "Vascular Normalization as a Therapeutic Strategy for Malignant and Nonmalignant Disease", doi: 10.1101/cshperspect.a006486.

[87] R. T. Tong, Y. Boucher, S. V. Kozin, F. Winkler, D. J. Hicklin, and R. K. Jain, "Vascular normalization by vascular endothelial growth factor receptor 2 blockade induces a pressure gradient across the vasculature and improves drug penetration in tumors," *Cancer Res*, vol. 64, no. 11, pp. 3731–3736, Jun. 2004, doi: 10.1158/0008-5472.CAN-04-0074.

[88] T. Stylianopoulos and R. K. Jain, "Combining two strategies to improve perfusion and drug delivery in solid tumors," *Proc Natl Acad Sci U S A*, vol. 110, no. 46, pp. 18632–18637, Nov. 2013, doi: 10.1073/PNAS.1318415110/-/DCSUPPLEMENTAL.

[89] V. P. Chauhan *et al.*, "Angiotensin inhibition enhances drug delivery and potentiates chemotherapy by decompressing tumour blood vessels," *Nat Commun*, vol. 4, 2013, doi: 10.1038/NCOMMS3516.

[90] K. Matuszewska, M. Pereira, D. Petrik, J. Lawler, and J. Petrik, “Normalizing Tumor Vasculature to Reduce Hypoxia, Enhance Perfusion, and Optimize Therapy Uptake,” *Cancers (Basel)*, vol. 13, no. 17, Sep. 2021, doi: 10.3390/CANCERS13174444.

[91] H. Zhu *et al.*, “Recombinant human endostatin enhances the radioresponse in esophageal squamous cell carcinoma by normalizing tumor vasculature and reducing hypoxia,” *Scientific Reports 2015 5:1*, vol. 5, no. 1, pp. 1–9, Sep. 2015, doi: 10.1038/srep14503.

[92] H. Huang *et al.*, “VEGF suppresses T-lymphocyte infiltration in the tumor microenvironment through inhibition of NF-κB-induced endothelial activation,” *FASEB Journal*, vol. 29, no. 1, pp. 227–238, 2015, doi: 10.1096/fj.14-250985.

[93] A. E. M. Dirkx *et al.*, “Anti-angiogenesis therapy can overcome endothelial cell anergy and promote leukocyte-endothelium interactions and infiltration in tumors,” *The FASEB Journal*, vol. 20, no. 6, pp. 621–630, Apr. 2006, doi: 10.1096/FJ.05-4493COM.

[94] W. A. Muller, “Leukocyte-Endothelial Cell Interactions in the Inflammatory Response,” *Laboratory Investigation 2002 82:5*, vol. 82, no. 5, pp. 521–534, May 2002, doi: 10.1038/labinvest.3780446.

[95] A. W. Griffioen, C. A. Damen, G. H. Blijham, and G. Groenewegen, “Tumor Angiogenesis Is Accompanied by a Decreased Inflammatory Response of Tumor-Associated Endothelium,” *Blood*, vol. 88, no. 2, pp. 667–673, Jul. 1996, doi: 10.1182/BLOOD.V88.2.667.BLOODJOURNAL882667.

[96] V. P. Chauhan *et al.*, “Normalization of tumour blood vessels improves the delivery of nanomedicines in a size-dependent manner,” *Nature Nanotechnology 2012 7:6*, vol. 7, no. 6, pp. 383–388, Apr. 2012, doi: 10.1038/nnano.2012.45.

[97] B. Farsaci *et al.*, “Immune consequences of decreasing tumor vasculature with antiangiogenic tyrosine kinase inhibitors in combination with therapeutic vaccines,” *Cancer Immunol Res*, vol. 2, no. 11, pp. 1090–1102, Nov. 2014, doi: 10.1158/2326-6066.CIR-14-0076/470275/AM/IMMUNE-CONSEQUENCES-OF-DECREASING-TUMOR.

[98] O. Draghiciu, H. W. Nijman, B. N. Hoogeboom, T. Meijerhof, and T. Daemen, “Sunitinib depletes myeloid-derived suppressor cells and synergizes with a cancer vaccine to enhance antigen-specific immune responses and tumor eradication,” *Oncoimmunology*, vol. 4, no. 3, pp. 1–11, 2015, doi: 10.4161/2162402X.2014.989764.

[99] Y. Huang *et al.*, “Vascular normalizing doses of antiangiogenic treatment reprogram the immunosuppressive tumor microenvironment and enhance immunotherapy,” *Proc Natl Acad Sci U S A*, vol. 109, no. 43, pp. 17561–17566, Oct. 2012, doi: 10.1073/PNAS.1215397109/-/DCSUPPLEMENTAL.

[100] R. K. Shrimali, Z. Yu, M. R. Theoret, D. Chinnasamy, N. P. Restifo, and S. A. Rosenberg, “Antiangiogenic agents can increase lymphocyte infiltration into tumor and enhance the effectiveness of adoptive immunotherapy of cancer,” *Cancer Res*, vol. 70, no. 15, p. 6171, Aug. 2010, doi: 10.1158/0008-5472.CAN-10-0153.

[101] S. Shi, R. Wang, Y. Chen, H. Song, L. Chen, and G. Huang, “Combining Antiangiogenic Therapy with Adoptive Cell Immunotherapy Exerts Better Antitumor Effects in Non-Small Cell Lung Cancer Models,” *PLoS One*, vol. 8, no. 6, Jun. 2013, doi: 10.1371/JOURNAL.PONE.0065757.

[102] L. Tao, G. Huang, S. Shi, and L. Chen, “Bevacizumab improves the antitumor efficacy of adoptive cytokine-induced killer cells therapy in non-small cell lung cancer models,” *Medical Oncology*, vol. 31, no. 1, pp. 1–8, Jan. 2014, doi: 10.1007/S12032-013-0777-3/FIGURES/4.

[103] A. E. *et al.*, “Combined antiangiogenic and anti-PD-L1 therapy stimulates tumor immunity through HEV formation,” *Sci Transl Med*, vol. 9, no. 385, 2017, [Online]. Available: http://www.embase.com/search/results?subaction=viewrecord&from=export&id=L615419521%0Ahttp://dx.doi.org/10.1126/scitranslmed.aak9679

[104] M. Schmittnaegel *et al.*, “Dual angiopoietin-2 and VEGFA inhibition elicits antitumor immunity that is enhanced by PD-1 checkpoint blockade,” *Sci Transl Med*, vol. 9, no. 385, 2017, doi: 10.1126/scitranslmed.aak9670.

[105] Q. Li *et al.*, “Low-dose anti-angiogenic therapy sensitizes breast cancer to PD-1 blockade,” *Clinical Cancer Research*, vol. 26, no. 7, pp. 1712–1724, 2020, doi: 10.1158/1078-0432.CCR-19-2179.

[106] S. Yasuda *et al.*, “Simultaneous blockade of programmed death 1 and vascular endothelial growth factor receptor 2 (VEGFR2) induces synergistic anti-tumour effect in vivo,” *Clin Exp Immunol*, vol. 172, no. 3, pp. 500–506, 2013, doi: 10.1111/cei.12069.

[107] E. Allen *et al.*, “Combined antiangiogenic and anti-PD-L1 therapy stimulates tumor immunity through HEV formation,” *Sci Transl Med*, vol. 9, no. 385, Apr. 2017, doi: 10.1126/SCITRANSLMED.AAK9679/SUPPL_FILE/AAK9679_SM.PDF.

[108] Y. Li *et al.*, “Treatment with a VEGFR-2 antibody results in intra-tumor immune modulation and enhances anti-tumor efficacy of PD-L1 blockade in syngeneic murine tumor models,” *PLoS One*, vol. 17, no. 7 July, pp. 1–16, 2022, doi: 10.1371/journal.pone.0268244.

[109] L. Meder *et al.*, “Combined VEGF and PD-L1 blockade displays synergistic treatment effects in an autochthonous mouse model of small cell lung cancer,” *Cancer Res*, vol. 78, no. 15, pp. 4270–4281, 2018, doi: 10.1158/0008-5472.CAN-17-2176.

[110] M. Di Tacchio *et al.*, “Tumor vessel normalization, immunostimulatory reprogramming, and improved survival in glioblastoma with combined inhibition of PD-1, angiopoietin-2,

and VEGF," *Cancer Immunol Res*, vol. 7, no. 12, pp. 1910–1927, Dec. 2019, doi: 10.1158/2326-6066.CIR-18-0865/470862/AM/TUMOR-VESSEL-NORMALIZATION-IMMUNO-STIMULATORY.

[111] 3 Kohei Shigeta1, 2,#, Meenal Datta1,#, Tai Hato1, "Dual PD-1 and VEGFR-2 blockade promotes vascular normalization and enhances anti-tumor immune responses in HCC," *Hepatology*, vol. 176, no. 5, pp. 139–148, 2020, doi: 10.1002/hep.30889.Dual.

[112] K. Kersten, K. E. de Visser, M. H. van Miltenburg, and J. Jonkers, "Genetically engineered mouse models in oncology research and cancer medicine," *EMBO Mol Med*, vol. 9, no. 2, p. 137, Feb. 2016, doi: 10.15252/EMMM.201606857.

[113] S. Ragusa *et al.*, "Antiangiogenic immunotherapy suppresses desmoplastic and chemoresistant intestinal tumors in mice," *J Clin Invest*, vol. 130, no. 3, pp. 1199–1216, Mar. 2020, doi: 10.1172/JCI129558.

[114] M. Singh *et al.*, "Anti-VEGF antibody therapy does not promote metastasis in genetically engineered mouse tumour models," *J Pathol*, vol. 227, no. 4, pp. 417–430, Jan. 2012, doi: 10.1002/PATH.4053.

[115] B. K. Majeti, J. H. Lee, B. H. Simmons, and F. Shojaei, "VEGF is an important mediator of tumor angiogenesis in malignant lesions in a genetically engineered mouse model of lung adenocarcinoma," *BMC Cancer*, vol. 13, no. 1, pp. 1–7, Apr. 2013, doi: 10.1186/1471-2407-13-213/FIGURES/4.

[116] S. Ragusa *et al.*, "Antiangiogenic immunotherapy suppresses desmoplastic and chemoresistant intestinal tumors in mice," *J Clin Invest*, vol. 130, no. 3, pp. 1199–1216, Mar. 2020, doi: 10.1172/JCI129558.

[117] M. Schmittnaegel *et al.*, "Dual angiopoietin-2 and VEGFA inhibition elicits antitumor immunity that is enhanced by PD-1 checkpoint blockade," *Sci Transl Med*, vol. 9, no. 385, Apr. 2017, doi: 10.1126/SCITRANSLMED.AAK9670.

[118] A. Martinez-Usatorre *et al.*, "Overcoming microenvironmental resistance to PD-1 blockade in genetically engineered lung cancer models," *Sci Transl Med*, vol. 13, no. 606, Aug. 2021, doi: 10.1126/SCITRANSLMED.ABD1616/SUPPL_FILE/SCITRANSLMED.ABD1616_TABLES_S1_AND_S2.ZIP.

[119] M. A. Jacobetz *et al.*, "Hyaluronan impairs vascular function and drug delivery in a mouse model of pancreatic cancer," *Gut*, vol. 62, no. 1, pp. 112–120, Jan. 2013, doi: 10.1136/GUTJNL-2012-302529.

[120] Y. Haibe *et al.*, "Resistance Mechanisms to Anti-angiogenic Therapies in Cancer," *Front Oncol*, vol. 10, p. 479832, Feb. 2020, doi: 10.3389/FONC.2020.00221/XML/NLM.

[121] S. M. Tolaney *et al.*, "Role of vascular density and normalization in response to neoadjuvant bevacizumab and chemotherapy in breast cancer patients," *Proc Natl Acad*

Sci U S A, vol. 112, no. 46, pp. 14325–14330, Nov. 2015, doi: 10.1073/PNAS.1518808112/-/DCSUPPLEMENTAL.

[122] E. Bullitt *et al.*, “Vessel tortuosity and brain tumor malignancy: a blinded study,” *Acad Radiol*, vol. 12, no. 10, pp. 1232–1240, Oct. 2005, doi: 10.1016/J.ACRA.2005.05.027.

[123] T. T. Batchelor *et al.*, “Phase II study of cediranib, an oral pan-vascular endothelial growth factor receptor tyrosine kinase inhibitor, in patients with recurrent glioblastoma,” *J Clin Oncol*, vol. 28, no. 17, pp. 2817–2823, Jun. 2010, doi: 10.1200/JCO.2009.26.3988.

[124] C. G. Willett *et al.*, “Direct evidence that the VEGF-specific antibody bevacizumab has antivascular effects in human rectal cancer,” *Nat Med*, vol. 10, no. 2, pp. 145–147, Feb. 2004, doi: 10.1038/NM988.

[125] P. S. Hegde *et al.*, “Predictive impact of circulating vascular endothelial growth factor in four phase III trials evaluating bevacizumab,” *Clin Cancer Res*, vol. 19, no. 4, pp. 929–937, Feb. 2013, doi: 10.1158/1078-0432.CCR-12-2535.

[126] V. A. Levin, J. Chan, M. Datta, J. L. Yee, and R. K. Jain, “Effect of angiotensin system inhibitors on survival in newly diagnosed glioma patients and recurrent glioblastoma patients receiving chemotherapy and/or bevacizumab,” *J Neurooncol*, vol. 134, no. 2, pp. 325–330, Sep. 2017, doi: 10.1007/S11060-017-2528-3/FIGURES/3.

[127] R. J. Motzer *et al.*, “Avelumab plus Axitinib versus Sunitinib for Advanced Renal-Cell Carcinoma,” *New England Journal of Medicine*, vol. 380, no. 12, pp. 1103–1115, Mar. 2019, doi: 10.1056/NEJMOA1816047/SUPPL_FILE/NEJMOA1816047_DATA-SHARING.PDF.

[128] A. Sandler *et al.*, “Paclitaxel–Carboplatin Alone or with Bevacizumab for Non–Small-Cell Lung Cancer,” *New England Journal of Medicine*, vol. 355, no. 24, pp. 2542–2550, Dec. 2006, doi: 10.1056/NEJMOA061884/ASSET/085B8775-00FA-4CA3-B5EC-4C1D4A30DFE0/ASSETS/IMAGES/LARGE/NEJMOA061884_T3.JPG.

[129] C. Cremolini *et al.*, “FOLFOXIRI plus bevacizumab versus FOLFIRI plus bevacizumab as first-line treatment of patients with metastatic colorectal cancer: Updated overall survival and molecular subgroup analyses of the open-label, phase 3 TRIBE study,” *Lancet Oncol*, vol. 16, no. 13, pp. 1306–1315, Oct. 2015, doi: 10.1016/S1470-2045(15)00122-9.

[130] V. P. Grignol *et al.*, “A phase 2 trial of bevacizumab and high-dose interferon alpha 2b in metastatic melanoma,” *Journal of Immunotherapy*, vol. 34, no. 6, pp. 509–515, Jul. 2011, doi: 10.1097/CJI.0B013E31821DCEFD.

[131] P. Schmid *et al.*, “KEYNOTE-522: Phase III study of pembrolizumab (pembro) + chemotherapy (chemo) vs placebo + chemo as neoadjuvant therapy followed by pembro vs placebo as adjuvant therapy for triple-negative breast cancer (TNBC).,” *Journal of Clinical Oncology*, vol. 36, no. 15_suppl, pp. TPS602–TPS602, May 2018, doi: 10.1200/JCO.2018.36.15_SUPPL.TPS602.

[132] “Common Cancer Sites — Cancer Stat Facts.” Accessed: Feb. 28, 2024. [Online]. Available: https://seer.cancer.gov/statfacts/html/common.html

[133] D. Fukumura, R. K. Jain, and E. L. Steele, “Tumor microvasculature and microenvironment: Targets for anti-angiogenesis and normalization,” *Microvasc Res*, vol. 74, no. 3, pp. 72–84, 2007.

[134] R. K. Jain, J. D. Martin, and T. Stylianopoulos, “The role of mechanical forces in tumor growth and therapy,” *Annu Rev Biomed Eng*, vol. 16, p. 321, Jul. 2014, doi: 10.1146/ANNUREV-BIOENG-071813-105259.

[135] F. Moradi Kashkooli, M. Soltani, and M. H. Hamedi, “Drug delivery to solid tumors with heterogeneous microvascular networks: Novel insights from image-based numerical modeling,” *European Journal of Pharmaceutical Sciences*, vol. 151, p. 105399, Aug. 2020, doi: 10.1016/J.EJPS.2020.105399.

[136] N. D. Sheybani *et al.*, “ImmunoPET-informed sequence for focused ultrasound-targeted mCD47 blockade controls glioma,” *Journal of Controlled Release*, vol. 331, pp. 19–29, Mar. 2021, doi: 10.1016/J.JCONREL.2021.01.023.

[137] R. K. Jain, “Normalizing tumor vasculature with anti-angiogenic therapy: a new paradigm for combination therapy,” *Nat Med*, vol. 7, no. 9, pp. 987–989, 2001, doi: 10.1038/NM0901-987.

[138] F. Winkler *et al.*, “Kinetics of vascular normalization by VEGFR2 blockade governs brain tumor response to radiation: Role of oxygenation, angiopoietin-1, and matrix metalloproteinases,” *Cancer Cell*, vol. 6, no. 6, pp. 553–563, Dec. 2004, doi: 10.1016/J.CCR.2004.10.011.

[139] S. Goel *et al.*, “Normalization of the vasculature for treatment of cancer and other diseases,” *Physiol Rev*, vol. 91, no. 3, pp. 1071–1121, 2011, doi: 10.1152/PHYSREV.00038.2010/ASSET/IMAGES/LARGE/Z9J0031125910015.JPEG.

[140] H. S. Abyaneh, M. Regenold, T. D. McKee, C. Allen, and M. A. Gauthier, “Towards extracellular matrix normalization for improved treatment of solid tumors,” *Theranostics*, vol. 10, no. 4, p. 1960, 2020, doi: 10.7150/THNO.39995.

[141] Y. Huang *et al.*, “Vascular normalizing doses of antiangiogenic treatment reprogram the immunosuppressive tumor microenvironment and enhance immunotherapy,” *Proc Natl Acad Sci U S A*, vol. 109, no. 43, pp. 17561–17566, Oct. 2012, doi: 10.1073/PNAS.1215397109/-/DCSUPPLEMENTAL.

[142] T. Yang *et al.*, “Vascular Normalization: A New Window Opened for Cancer Therapies,” *Front Oncol*, vol. 11, p. 719836, Aug. 2021, doi: 10.3389/FONC.2021.719836/BIBTEX.

[143] D. G. Fisher *et al.*, “Focused Ultrasound Blood-Brain Barrier Opening Arrests the Growth and Formation of Cerebral Cavernous Malformations,” *bioRxiv*, p. 2024.01.31.577810, Feb. 2024, doi: 10.1101/2024.01.31.577810.

[144] “Combined Therapy of Local and Metastatic 4T1 Breast Tumor in Mice Using SU6668, an Inhibitor of Angiogenic Receptor Tyrosine Kinases, and the Immunostimulator B7.2-IgG Fusion Protein1 | Cancer Research | American Association for Cancer Research.” Accessed: May 06, 2024. [Online]. Available: https://aacrjournals.org/cancerres/article/62/20/5727/509275/Combined-Therapy-of-Local-and-Metastatic-4T1

[145] E. Hoffmann *et al.*, “Vascular response patterns to targeted therapies in murine breast cancer models with divergent degrees of malignancy,” *Breast Cancer Res*, vol. 25, no. 1, p. 56, Dec. 2023, doi: 10.1186/S13058-023-01658-9.

[146] J. J. Arroyo-Crespo *et al.*, “Characterization of triple-negative breast cancer preclinical models provides functional evidence of metastatic progression,” *Int J Cancer*, vol. 145, no. 8, pp. 2267–2281, Oct. 2019, doi: 10.1002/IJC.32270.

[147] B. Schrörs *et al.*, “Multi-Omics Characterization of the 4T1 Murine Mammary Gland Tumor Model,” *Front Oncol*, vol. 10, p. 1195, Jul. 2020, doi: 10.3389/FONC.2020.01195/FULL.

[148] K. P. Fabian, M. R. Padget, R. Fujii, J. Schlom, and J. W. Hodge, “Differential combination immunotherapy requirements for inflamed (warm) tumors versus T cell excluded (cool) tumors: engage, expand, enable, and evolve,” *J Immunother Cancer*, vol. 9, no. 2, p. e001691, Feb. 2021, doi: 10.1136/JITC-2020-001691.

[149] Y. Huang, T. Stylianopoulos, D. G. Duda, D. Fukumura, and R. K. Jain, “Benefits of vascular normalization are dose- and time-dependent,” *Cancer Res*, vol. 73, no. 23, pp. 7144–7146, Dec. 2013, doi: 10.1158/0008-5472.CAN-13-1989.

[150] M. L. Chen, L. Lesko, and R. L. Williams, “Measures of exposure versus measures of rate and extent of absorption,” *Clin Pharmacokinet*, vol. 40, no. 8, pp. 565–572, Sep. 2001, doi: 10.2165/00003088-200140080-00001/FIGURES/TAB1.

[151] M. Abdel-Tawab *et al.*, “An exploratory study on the effect of mechanical stress on particle formation in monoclonal antibody infusions,” *Arch Pharm (Weinheim)*, vol. 356, no. 8, p. 2300101, Aug. 2023, doi: 10.1002/ARDP.202300101.

[152] C. M. Gorick *et al.*, “Sonoselective transfection of cerebral vasculature without blood-brain barrier disruption,” *Proc Natl Acad Sci U S A*, vol. 117, no. 11, pp. 5644–5654, 2020, doi: 10.1073/pnas.1914595117.

[153] J. Li, X. Gao, M. Dominik Nickel, J. Cheng, and J. Zhu, “Native T1 mapping for differentiating the histopathologic type, grade, and stage of rectal adenocarcinoma: a pilot study,” *Cancer Imaging*, vol. 22, no. 1, Dec. 2022, doi: 10.1186/S40644-022-00461-7.

[154] D. Kuetting *et al.*, “Evaluation of malignant effusions using MR-based T1 mapping,” *Sci Rep*, vol. 11, no. 1, Dec. 2021, doi: 10.1038/S41598-021-86632-1.

[155] K. Herrmann *et al.*, “Dynamic Quantitative T1 Mapping in Orthotopic Brain Tumor Xenografts,” *Transl Oncol*, vol. 9, no. 2, p. 147, Apr. 2016, doi: 10.1016/J.TRANON.2016.02.004.

[156] G. Donatelli *et al.*, “Quantitative T1 mapping detects blood–brain barrier breakdown in apparently non-enhancing multiple sclerosis lesions,” *Neuroimage Clin*, vol. 40, p. 103509, Jan. 2023, doi: 10.1016/J.NICL.2023.103509.

[157] Y. Xue *et al.*, “In vivo T1 mapping for quantifying glymphatic system transport and cervical lymph node drainage,” *Scientific Reports 2020 10:1*, vol. 10, no. 1, pp. 1–13, Sep. 2020, doi: 10.1038/s41598-020-71582-x.

[158] C. Chauhan *et al.*, “Normalization of Tumour Blood Vessels Improves the Delivery of Nanomedicines in a Size-Dependent Manner,” *Nat Nanotechnol*, vol. 7, no. 6, pp. 383–388, 2012, doi: 10.1038/nnano.2012.45.

[159] Y. Huang, T. Stylianopoulos, D. G. Duda, D. Fukumura, and R. K. Jain, “Benefits of vascular normalization are dose-and time-dependent”, doi: 10.1158/0008-5472.CAN-13-1989.

[160] N. Qayum *et al.*, “Tumor Vascular Changes Mediated by Inhibition of Oncogenic Signaling,” *Cancer Res*, vol. 69, no. 15, p. 6347, Aug. 2009, doi: 10.1158/0008-5472.CAN-09-0657.

[161] H. Wildiers *et al.*, “Effect of antivascular endothelial growth factor treatment on the intratumoral uptake of CPT-11”, doi: 10.1038/sj.bjc.6601005.

[162] R. K. Jain, R. T. Tong, and L. L. Munn, “Effect of Vascular Normalization by Antiangiogenic Therapy on Interstitial Hypertension, Peritumor Edema, and Lymphatic Metastasis: Insights from a Mathematical Model,” *Cancer Res*, vol. 67, no. 6, p. 2729, Mar. 2007, doi: 10.1158/0008-5472.CAN-06-4102.

[163] Q. Zhou, P. Guo, and J. M. Gallo, “Impact of Angiogenesis Inhibition by Sunitinib on Tumor Distribution of Temozolomide,” *Clinical Cancer Research*, vol. 14, no. 5, pp. 1540–1549, Mar. 2008, doi: 10.1158/1078-0432.CCR-07-4544.

[164] P. V. Dickson *et al.*, “Bevacizumab-Induced Transient Remodeling of the Vasculature in Neuroblastoma Xenografts Results in Improved Delivery and Efficacy of Systemically Administered Chemotherapy,” *Clinical Cancer Research*, vol. 13, no. 13, pp. 3942–3950, Jul. 2007, doi: 10.1158/1078-0432.CCR-07-0278.

[165] M. Ohta *et al.*, “TSU68, an antiangiogenic receptor tyrosine kinase inhibitor, induces tumor vascular normalization in a human cancer xenograft nude mouse model,” *Surg Today*, vol. 39, no. 12, pp. 1046–1053, Dec. 2009, doi: 10.1007/S00595-009-4020-Y/METRICS.

[166] K. Matuszewska, M. Pereira, D. Petrik, J. Lawler, and J. Petrik, “Normalizing tumor vasculature to reduce hypoxia, enhance perfusion, and optimize therapy uptake,” *Cancers (Basel)*, vol. 13, no. 17, pp. 1–19, 2021, doi: 10.3390/cancers13174444.

[167] A. E. M. Dirkx *et al.*, “Anti-angiogenesis therapy can overcome endothelial cell anergy and promote leukocyte-endothelium interactions and infiltration in tumors,” *The FASEB Journal*, vol. 20, no. 6, pp. 621–630, Apr. 2006, doi: 10.1096/FJ.05-4493COM.

[168] D. M. McDonald and P. Baluk, “Imaging of angiogenesis in inflamed airways and tumors: newly formed blood vessels are not alike and may be wildly abnormal: Parker B. Francis lecture,” *Chest*, vol. 128, no. 6 Suppl, pp. 602S-608S, 2005, doi: 10.1378/CHEST.128.6_SUPPL.602S-A.

[169] “Fluctuations in red cell flux in tumor microvessels can lead to transient hypoxia and reoxygenation in tumor parenchyma - PubMed.” Accessed: Jan. 21, 2025. [Online]. Available: https://pubmed.ncbi.nlm.nih.gov/8968110/

[170] L. Piali, A. Fichtd, H. J. Terpe, B. A. Imhof, and R. H. Gisler, “Endothelial vascular cell adhesion molecule 1 expression is suppressed by melanoma and carcinoma,” *Journal of Experimental Medicine*, vol. 181, no. 2, pp. 811–816, 1995, doi: 10.1084/jem.181.2.811.

[171] A. W. Griffioen, C. A. Damen, S. Martinotti, G. H. Blijham, and G. Groenewegen, “Endothelial intercellular adhesion molecule-1 expression is suppressed in human malignancies: The role of angiogenic factors,” *Cancer Res*, vol. 56, no. 5, pp. 1111–1117, 1996.

[172] S. Tang *et al.*, “Immune Checkpoint Inhibitors in Non-Small Cell Lung Cancer: Progress, Challenges, and Prospects,” *Cells*, vol. 11, no. 3, p. 320, Feb. 2022, doi: 10.3390/CELLS11030320.

[173] T. J. Okobi *et al.*, “Immune Checkpoint Inhibitors as a Treatment Option for Bladder Cancer: Current Evidence,” *Cureus*, vol. 15, no. 6, p. e40031, Jun. 2023, doi: 10.7759/CUREUS.40031.

[174] W. Xu, M. B. Atkins, and D. F. McDermott, “Checkpoint inhibitor immunotherapy in kidney cancer,” *Nature Reviews Urology 2020 17:3*, vol. 17, no. 3, pp. 137–150, Feb. 2020, doi: 10.1038/s41585-020-0282-3.

[175] S. Makaremi *et al.*, “Immune Checkpoint Inhibitors in Colorectal Cancer: Challenges and Future Prospects,” *Biomedicines*, vol. 9, no. 9, p. 1075, 2021, doi: 10.3390/BIOMEDICINES9091075.

[176] S. Venkatachalam, T. R. McFarland, N. Agarwal, and U. Swami, “Immune Checkpoint Inhibitors in Prostate Cancer,” *Cancers (Basel)*, vol. 13, no. 9, p. 2187, May 2021, doi: 10.3390/CANCERS13092187.

[177] A. C. Huang and R. Zappasodi, “A decade of checkpoint blockade immunotherapy in melanoma: understanding the molecular basis for immune sensitivity and resistance,”

Nature Immunology 2022 23:5, vol. 23, no. 5, pp. 660–670, Mar. 2022, doi: 10.1038/s41590-022-01141-1.

[178] R. Thomas, G. Al-Khadairi, and J. Decock, “Immune Checkpoint Inhibitors in Triple Negative Breast Cancer Treatment: Promising Future Prospects,” *Front Oncol*, vol. 10, p. 600573, Feb. 2021, doi: 10.3389/FONC.2020.600573.

[179] Y. Ju *et al.*, “Barriers and opportunities in pancreatic cancer immunotherapy,” *npj Precision Oncology 2024 8:1*, vol. 8, no. 1, pp. 1–18, Sep. 2024, doi: 10.1038/s41698-024-00681-z.

[180] N. Goda *et al.*, “The ratio of CD8 + lymphocytes to tumor-infiltrating suppressive FOXP3 + effector regulatory T cells is associated with treatment response in invasive breast cancer,” *Discover. Oncology*, vol. 13, no. 1, p. 27, Dec. 2022, doi: 10.1007/S12672-022-00482-5.

[181] C. C. Preston *et al.*, “The Ratios of CD8+ T Cells to CD4+CD25+ FOXP3+ and FOXP3- T Cells Correlate with Poor Clinical Outcome in Human Serous Ovarian Cancer,” *PLoS One*, vol. 8, no. 11, p. e80063, Nov. 2013, doi: 10.1371/JOURNAL.PONE.0080063.

[182] S. J. Hobbs and J. C. Nolz, “Targeted Expansion of Tissue-Resident CD8+ T Cells to Boost Cellular Immunity in the Skin,” *Cell Rep*, vol. 29, no. 10, p. 2990, Dec. 2019, doi: 10.1016/J.CELREP.2019.10.126.

[183] R. A. Clark *et al.*, “Skin effector memory T cells do not recirculate and provide immune protection in alemtuzumab-treated CTCL patients,” *Sci Transl Med*, vol. 4, no. 117, p. 117ra7, Jan. 2012, doi: 10.1126/SCITRANSLMED.3003008.

[184] N. P. Goplen *et al.*, “Tissue-resident CD8+ T cells drive age-associated chronic lung sequelae after viral pneumonia,” *Sci Immunol*, vol. 5, no. 53, Nov. 2020, doi: 10.1126/SCIIMMUNOL.ABC4557.

[185] S. Abe *et al.*, “Original research: Combination of ultrasound-based mechanical disruption of tumor with immune checkpoint blockade modifies tumor microenvironment and augments systemic antitumor immunity,” *J Immunother Cancer*, vol. 10, no. 1, p. 3717, Jan. 2022, doi: 10.1136/JITC-2021-003717.

[186] E. A. Thim *et al.*, “Focused ultrasound ablation of melanoma with boiling histotripsy yields abscopal tumor control and antigen-dependent dendritic cell activation,” *Theranostics*, vol. 14, no. 4, p. 1647, 2024, doi: 10.7150/THNO.92089.

[187] F. Liu *et al.*, “Boosting high-intensity focused ultrasound-induced anti-tumor immunity using a sparse-scan strategy that can more effectively promote dendritic cell maturation,” *J Transl Med*, vol. 8, pp. 1–12, 2010, doi: 10.1186/1479-5876-8-7.

[188] Y. Jin *et al.*, “Different syngeneic tumors show distinctive intrinsic tumor-immunity and mechanisms of actions (MOA) of anti-PD-1 treatment,” *Scientific Reports 2022 12:1*, vol. 12, no. 1, pp. 1–18, Feb. 2022, doi: 10.1038/s41598-022-07153-z.

[189] D. Duarte and N. Vale, “Evaluation of synergism in drug combinations and reference models for future orientations in oncology,” *Current Research in Pharmacology and Drug Discovery*, vol. 3, p. 100110, Jan. 2022, doi: 10.1016/J.CRPHAR.2022.100110.

[190] “Anti-Vascular endothelial growth factor treatment augments tumor radiation response under normoxic or hypoxic conditions - PubMed.” Accessed: Jan. 18, 2025. [Online]. Available: https://pubmed.ncbi.nlm.nih.gov/11034104/

[191] H. Wildiers *et al.*, “Effect of antivascular endothelial growth factor treatment on the intratumoral uptake of CPT-11,” *Br J Cancer*, vol. 88, no. 12, p. 1979, Jun. 2003, doi: 10.1038/SJ.BJC.6601005.

[192] Y. Kodera *et al.*, “Sunitinib inhibits lymphatic endothelial cell functions and lymph node metastasis in a breast cancer model through inhibition of vascular endothelial growth factor receptor 3,” *Breast Cancer Research*, vol. 13, no. 3, pp. 1–11, Jun. 2011, doi: 10.1186/BCR2903/TABLES/1.

[193] Y. Hong *et al.*, “VEGF-A promotes tissue repair-associated lymphatic vessel formation via VEGFR-2 and the α1β1 and α2β1 integrins,” *The FASEB Journal*, vol. 18, no. 10, pp. 1111–1113, Jul. 2004, doi: 10.1096/FJ.03-1179FJE.

[194] Y. Zhang *et al.*, “Heterogeneity in VEGFR3 levels drives lymphatic vessel hyperplasia through cell-autonomous and non-cell-autonomous mechanisms,” *Nature Communications 2018 9:1*, vol. 9, no. 1, pp. 1–15, Apr. 2018, doi: 10.1038/s41467-018-03692-0.

[195] Z. Wang *et al.*, “DC101, an anti-VEGFR2 agent, promotes high-endothelial venule formation and immune infiltration versus SAR131675 and fruquintinib,” *Biochem Biophys Res Commun*, vol. 661, pp. 10–20, 2023, doi: 10.1016/j.bbrc.2023.04.018.

[196] D. Sano *et al.*, “The Effect of Combination Anti–Endothelial Growth Factor Receptor and Anti–Vascular Endothelial Growth Factor Receptor 2 Targeted Therapy on Lymph Node Metastasis: A Study in an Orthotopic Nude Mouse Model of Squamous Cell Carcinoma of the Oral Tongue,” *Arch Otolaryngol Head Neck Surg*, vol. 135, no. 4, pp. 411–420, Apr. 2009, doi: 10.1001/ARCHOTO.2009.14.

[197] A. Asrir *et al.*, “Tumor-associated high endothelial venules mediate lymphocyte entry into tumors and predict response to PD-1 plus CTLA-4 combination immunotherapy,” *Cancer Cell*, vol. 0, no. 0, Feb. 2022, doi: 10.1016/J.CCELL.2022.01.002.

[198] Y. Zhang *et al.*, “Establishment of a murine breast tumor model by subcutaneous or orthotopic implantation,” *Oncol Lett*, vol. 15, no. 5, p. 6233, May 2018, doi: 10.3892/OL.2018.8113.

[199] K. Kersten, K. E. de Visser, M. H. van Miltenburg, and J. Jonkers, “Genetically engineered mouse models in oncology research and cancer medicine,” *EMBO Mol Med*, vol. 9, no. 2, p. 137, Feb. 2016, doi: 10.15252/EMMM.201606857.

[200] C. R. Ireson, M. S. Alavijeh, A. M. Palmer, E. R. Fowler, and H. J. Jones, “The role of mouse tumour models in the discovery and development of anticancer drugs,” *British Journal of Cancer 2019 121:2*, vol. 121, no. 2, pp. 101–108, Jun. 2019, doi: 10.1038/s41416-019-0495-5.

[201] “Ramucirumab - NCI.” Accessed: Mar. 10, 2025. [Online]. Available: https://www.cancer.gov/about-cancer/treatment/drugs/ramucirumab

[202] “Bevacizumab - NCI.” Accessed: Mar. 10, 2025. [Online]. Available: https://www.cancer.gov/about-cancer/treatment/drugs/bevacizumab

[203] D. D. Hu-Lowe *et al.*, “Nonclinical antiangiogenesis and antitumor activities of axitinib (AG-013736), an oral, potent, and selective inhibitor of vascular endothelial growth factor receptor tyrosine kinases 1, 2, 3,” *Clin Cancer Res*, vol. 14, no. 22, pp. 7272–7283, Nov. 2008, doi: 10.1158/1078-0432.CCR-08-0652.

[204] M. Matsuki *et al.*, “Lenvatinib inhibits angiogenesis and tumor fibroblast growth factor signaling pathways in human hepatocellular carcinoma models,” *Cancer Med*, vol. 7, no. 6, pp. 2641–2653, Jun. 2018, doi: 10.1002/CAM4.1517.

[205] S. Kim *et al.*, “Sorafenib inhibits the angiogenesis and growth of orthotopic anaplastic thyroid carcinoma xenografts in nude mice,” *Mol Cancer Ther*, vol. 6, no. 6, pp. 1785–1792, Jun. 2007, doi: 10.1158/1535-7163.MCT-06-0595.

[206] S. De Boüard *et al.*, “Antiangiogenic and anti-invasive effects of sunitinib on experimental human glioblastoma,” *Neuro Oncol*, vol. 9, no. 4, p. 412, Oct. 2007, doi: 10.1215/15228517-2007-024.

[207] L. Li, J. Yu, S. Jiao, W. Wang, F. Zhang, and S. Sun, “Vandetanib (ZD6474) induces antiangiogenesis through mTOR–HIF-1 alpha–VEGF signaling axis in breast cancer cells,” *Onco Targets Ther*, vol. 11, p. 8543, 2018, doi: 10.2147/OTT.S175578.

[208] N. Une *et al.*, “The anti-angiogenic agent lenvatinib induces tumor vessel normalization and enhances radiosensitivity in hepatocellular tumors,” *Med Oncol*, vol. 38, no. 6, Jun. 2021, doi: 10.1007/S12032-021-01503-Z.

[209] J. Ma and D. J. Waxman, “Dominant Effect of Anti-angiogenesis in Combination Therapy Involving Cyclophosphamide and the VEGF Receptor Tyrosine Kinase Inhibitor Axitinib,” *Clin Cancer Res*, vol. 15, no. 2, p. 578, Jan. 2009, doi: 10.1158/1078-0432.CCR-08-1174.

[210] A. Weiss *et al.*, “Angiostatic treatment prior to chemo- or photodynamic therapy improves anti-tumor efficacy,” *Sci Rep*, vol. 5, Mar. 2015, doi: 10.1038/SREP08990.

[211] D. G. Duda and R. K. Jain, “Revisiting Antiangiogenic Multikinase Inhibitors in the Era of Immune Checkpoint Blockade: The Case of Sorafenib,” *Cancer Res*, vol. 82, no. 20, pp. 3665–3667, Oct. 2022, doi: 10.1158/0008-5472.CAN-22-2639.

[212] S. Matsumoto *et al.*, “Anti-angiogenic agent sunitinib transiently increases tumor oxygenation and suppresses cycling hypoxia,” *Cancer Res*, vol. 71, no. 20, p. 6350, Oct. 2011, doi: 10.1158/0008-5472.CAN-11-2025.

[213] J. H. Tai, J. Tessier, A. J. Ryan, L. Hoffman, X. Chen, and T. Y. Lee, “Assessment of Acute Antivascular Effects of Vandetanib with High-Resolution Dynamic Contrast-Enhanced Computed Tomographic Imaging in a Human Colon Tumor Xenograft Model in the Nude Rat,” *Neoplasia*, vol. 12, no. 9, p. 697, 2010, doi: 10.1593/NEO.10292.

[214] H. Gong *et al.*, “Hyaluronidase To Enhance Nanoparticle-Based Photodynamic Tumor Therapy,” *Nano Lett*, vol. 16, no. 4, pp. 2512–2521, Apr. 2016, doi: 10.1021/ACS.NANOLETT.6B00068/SUPPL_FILE/NL6B00068_SI_003.AVI.

[215] Y. Liu *et al.*, “Remotely boosting hyaluronidase activity to normalize the hypoxic immunosuppressive tumor microenvironment for photothermal immunotherapy,” *Biomaterials*, vol. 284, May 2022, doi: 10.1016/J.BIOMATERIALS.2022.121516.

[216] C. J. Whatcott, H. Han, R. G. Posner, G. Hostetter, and D. D. Von Hoff, “Targeting the tumor microenvironment in cancer: why hyaluronidase deserves a second look,” *Cancer Discov*, vol. 1, no. 4, p. 291, Sep. 2011, doi: 10.1158/2159-8290.CD-11-0136.

[217] J. Zonneville, A. Safina, A. M. Truskinovsky, C. L. Arteaga, and A. V. Bakin, “TGF-β signaling promotes tumor vasculature by enhancing the pericyte-endothelium association,” *BMC Cancer*, vol. 18, no. 1, pp. 1–13, Jun. 2018, doi: 10.1186/S12885-018-4587-Z/FIGURES/6.

[218] M. Panagi *et al.*, “TGF-β inhibition combined with cytotoxic nanomedicine normalizes triple negative breast cancer microenvironment towards anti-tumor immunity,” *Theranostics*, vol. 10, no. 4, pp. 1910–1922, 2020, doi: 10.7150/THNO.36936.

[219] L. J *et al.*, “TGF-β blockade improves the distribution and efficacy of therapeutics in breast carcinoma by normalizing the tumor stroma,” *Proc Natl Acad Sci U S A*, vol. 109, no. 41, pp. 16618–16623, Oct. 2012, doi: 10.1073/PNAS.1117610109.

[220] M. S. Felix *et al.*, “Ultrasound-mediated blood-brain barrier opening improves whole brain gene delivery in mice,” *Pharmaceutics*, vol. 13, no. 8, p. 1245, Aug. 2021, doi: 10.3390/PHARMACEUTICS13081245/S1.

[221] P. Mondou, S. Mériaux, F. Nageotte, J. Vappou, A. Novell, and B. Larrat, “State of the art on microbubble cavitation monitoring and feedback control for blood-brain-barrier opening using focused ultrasound,” *Phys Med Biol*, vol. 68, no. 18, Sep. 2023, doi: 10.1088/1361-6560/ACE23E.

[222] C. Y. Chien *et al.*, “Quality assurance for focused ultrasound-induced blood-brain barrier opening procedure using passive acoustic detection,” *EBioMedicine*, vol. 102, p. 105066, Apr. 2024, doi: 10.1016/j.ebiom.2024.105066.

[223] W. Lim Kee Chang *et al.*, “Rapid short-pulses of focused ultrasound and microbubbles deliver a range of agent sizes to the brain,” *Scientific Reports 2023 13:1*, vol. 13, no. 1, pp. 1–12, Apr. 2023, doi: 10.1038/s41598-023-33671-5.

[224] G. Samiotaki and E. E. Konofagou, “Dependence of the Reversibility of Focused-Ultrasound-Induced Blood–Brain Barrier Opening on Pressure and Pulse Length In Vivo,” *IEEE Trans Ultrason Ferroelectr Freq Control*, vol. 60, no. 11, p. 2257, 2013, doi: 10.1109/TUFFC.2013.6644731.

[225] R. Chopra, N. Vykhodtseva, and K. Hynynen, “Influence of Exposure Time and Pressure Amplitude on Blood−Brain-Barrier Opening Using Transcranial Ultrasound Exposures,” *ACS Chem Neurosci*, vol. 1, no. 5, p. 391, May 2010, doi: 10.1021/CN9000445.

[226] A. Carpentier *et al.*, “Repeated blood–brain barrier opening with a nine-emitter implantable ultrasound device in combination with carboplatin in recurrent glioblastoma: a phase I/II clinical trial,” *Nature Communications 2024 15:1*, vol. 15, no. 1, pp. 1–12, Feb. 2024, doi: 10.1038/s41467-024-45818-7.

[227] N. D. Sheybani *et al.*, “ImmunoPET-informed sequence for focused ultrasound-targeted mCD47 blockade controls glioma,” *J Control Release*, vol. 331, pp. 19–29, Mar. 2021, doi: 10.1016/J.JCONREL.2021.01.023.

[228] R. Manafi-Farid *et al.*, “ImmunoPET: Antibody-Based PET Imaging in Solid Tumors,” *Front Med (Lausanne)*, vol. 9, p. 916693, Jun. 2022, doi: 10.3389/FMED.2022.916693/PDF.

[229] E. C. Unger *et al.*, “Magnetic resonance imaging using gadolinium labeled monoclonal antibody,” *Invest Radiol*, vol. 20, no. 7, pp. 693–700, 1985, doi: 10.1097/00004424-198510000-00008.

[230] M. A. Nejad and H. M. Urbassek, “Diffusion of cisplatin molecules in silica nanopores: Molecular dynamics study of a targeted drug delivery system,” *J Mol Graph Model*, vol. 86, pp. 228–234, Jan. 2019, doi: 10.1016/J.JMGM.2018.10.021.

[231] M. Rahman, “Magnetic Resonance Imaging and Iron-oxide Nanoparticles in the era of Personalized Medicine,” *Nanotheranostics*, vol. 7, no. 4, p. 424, 2023, doi: 10.7150/NTNO.86467.

[232] R. J. Gillies, P. E. Kinahan, and H. Hricak, “Radiomics: Images Are More than Pictures, They Are Data,” *Radiology*, vol. 278, no. 2, p. 563, Feb. 2015, doi: 10.1148/RADIOL.2015151169.

[233] S. Petcharunpaisan, J. Ramalho, M. Castillo, and O. Carmichael, “Arterial spin labeling in neuroimaging,” *World J Radiol*, vol. 2, no. 10, p. 384, 2010, doi: 10.4329/WJR.V2.I10.384.

[234] R. J. E. van den Bijgaart, D. C. Eikelenboom, M. Hoogenboom, J. J. Fütterer, M. H. den Brok, and G. J. Adema, “Thermal and mechanical high-intensity focused ultrasound:

perspectives on tumor ablation, immune effects and combination strategies," *Cancer Immunol Immunother*, vol. 66, no. 2, p. 247, Feb. 2016, doi: 10.1007/S00262-016-1891-9.

[235] J. Schumann, K. Stanko, U. Schliesser, C. Appelt, and B. Sawitzki, "Differences in CD44 Surface Expression Levels and Function Discriminates IL-17 and IFN-γ Producing Helper T Cells," *PLoS One*, vol. 10, no. 7, p. e0132479, Jul. 2015, doi: 10.1371/JOURNAL.PONE.0132479.

[236] R. J. E. van den Bijgaart *et al.*, "Mechanical high-intensity focused ultrasound creates unique tumor debris enhancing dendritic cell-induced T cell activation," *Front Immunol*, vol. 13, p. 1038347, Dec. 2022, doi: 10.3389/FIMMU.2022.1038347/BIBTEX.

[237] Q. Vos, A. Lees, Z. Q. Wu, C. M. Snapper, and J. J. Mond, "B-cell activation by T-cell-independent type 2 antigens as an integral part of the humoral immune response to pathogenic microorganisms," *Immunol Rev*, vol. 176, pp. 154–170, 2000, doi: 10.1034/J.1600-065X.2000.00607.X.

[238] I. Rastogi, D. Jeon, J. E. Moseman, A. Muralidhar, H. K. Potluri, and D. G. McNeel, "Role of B cells as antigen presenting cells," *Front Immunol*, vol. 13, p. 954936, Sep. 2022, doi: 10.3389/FIMMU.2022.954936.

[239] C. M. Laumont, A. C. Banville, M. Gilardi, D. P. Hollern, and B. H. Nelson, "Tumour-infiltrating B cells: immunological mechanisms, clinical impact and therapeutic opportunities," *Nature Reviews Cancer 2022 22:7*, vol. 22, no. 7, pp. 414–430, Apr. 2022, doi: 10.1038/s41568-022-00466-1.

[240] P. Lu, X. Q. Zhu, Z. L. Xu, Q. Zhou, J. Zhang, and F. Wu, "Increased infiltration of activated tumor-infiltrating lymphocytes after high intensity focused ultrasound ablation of human breast cancer," *Surgery*, vol. 145, no. 3, pp. 286–293, Mar. 2009, doi: 10.1016/j.surg.2008.10.010.

[241] S. N. Christo, S. L. Park, S. N. Mueller, and L. K. Mackay, "The Multifaceted Role of Tissue-Resident Memory T Cells," *Annu Rev Immunol*, vol. 42, no. 1, pp. 317–345, Jun. 2024, doi: 10.1146/ANNUREV-IMMUNOL-101320-020220/CITE/REFWORKS.

[242] H. Dillekås, M. S. Rogers, and O. Straume, "Are 90% of deaths from cancer caused by metastases?," *Cancer Med*, vol. 8, no. 12, p. 5574, Sep. 2019, doi: 10.1002/CAM4.2474.

[243] P. R. TWENTYMAN, "The Growth of the Emt6 Tumour In the Lungs of Balb C Mice Following Intravenous Inoculation of Tumour Cells From Culture," *Cell Prolif*, vol. 11, no. 1, pp. 57–68, Jan. 1978, doi: 10.1111/J.1365-2184.1978.TB00875.X.

[244] N. Harbeck *et al.*, "Breast cancer," *Nature Reviews Disease Primers 2019 5:1*, vol. 5, no. 1, pp. 1–31, Sep. 2019, doi: 10.1038/s41572-019-0111-2.

[245] M. Ouzounova *et al.*, "Monocytic and granulocytic myeloid derived suppressor cells differentially regulate spatiotemporal tumour plasticity during metastatic cascade," *Nature*

Communications 2017 8:1, vol. 8, no. 1, pp. 1–13, Apr. 2017, doi: 10.1038/ncomms14979.

[246] C. MacDonald *et al.*, “Comparing thermal stress reduction strategies that influence MDSC accumulation in tumor bearing mice,” *Cell Immunol*, vol. 361, Mar. 2021, doi: 10.1016/J.CELLIMM.2021.104285.

[247] C. Groth *et al.*, “Immunosuppression mediated by myeloid-derived suppressor cells (MDSCs) during tumour progression,” *British Journal of Cancer 2018 120:1*, vol. 120, no. 1, pp. 16–25, Nov. 2018, doi: 10.1038/s41416-018-0333-1.

[248] A. Mantovani, F. Marchesi, A. Malesci, L. Laghi, and P. Allavena, “Tumor-Associated Macrophages as Treatment Targets in Oncology,” *Nat Rev Clin Oncol*, vol. 14, no. 7, p. 399, Jul. 2017, doi: 10.1038/NRCLINONC.2016.217.

[249] K. Ektate, M. C. Munteanu, H. Ashar, J. Malayer, and A. Ranjan, “Chemo-immunotherapy of colon cancer with focused ultrasound and Salmonella-laden temperature sensitive liposomes (thermobots),” *Scientific Reports 2018 8:1*, vol. 8, no. 1, pp. 1–12, Aug. 2018, doi: 10.1038/s41598-018-30106-4.

[250] I. B. Barsoum, M. Koti, D. R. Siemens, and C. H. Graham, “Mechanisms of hypoxia-mediated immune escape in cancer,” *Cancer Res*, vol. 74, no. 24, pp. 7185–7190, Dec. 2014, doi: 10.1158/0008-5472.CAN-14-2598.

[251] A. Eranki *et al.*, “High Intensity Focused Ultrasound (HIFU) Triggers Immune Sensitization of Refractory Murine Neuroblastoma to Checkpoint Inhibitor Therapy,” *Clin Cancer Res*, vol. 26, no. 5, p. 1152, Mar. 2019, doi: 10.1158/1078-0432.CCR-19-1604.

[252] P. Lu, X. Q. Zhu, Z. L. Xu, Q. Zhou, J. Zhang, and F. Wu, “Increased infiltration of activated tumor-infiltrating lymphocytes after high intensity focused ultrasound ablation of human breast cancer,” *Surgery*, vol. 145, no. 3, pp. 286–293, Mar. 2009, doi: 10.1016/J.SURG.2008.10.010.

[253] S. Bandyopadhyay *et al.*, “Low intensity focused ultrasound induces reversal of tumor-induced T cell tolerance and prevents immune escape,” *J Immunol*, vol. 196, no. 4, p. 1964, Feb. 2016, doi: 10.4049/JIMMUNOL.1500541.

[254] Z. Hu *et al.*, “Release of endogenous danger signals from HIFU-treated tumor cells and their stimulatory effects on APCs,” *Biochem Biophys Res Commun*, vol. 335, no. 1, p. 124, Sep. 2005, doi: 10.1016/J.BBRC.2005.07.071.

[255] F. Wu, L. Zhou, and W. R. Chen, “Host antitumour immune responses to HIFU ablation,” *International Journal of Hyperthermia*, vol. 23, no. 2, pp. 165–171, 2007, doi: 10.1080/02656730701206638.

[256] M. T. Silvestrini *et al.*, “Priming is key to effective incorporation of image-guided thermal ablation into immunotherapy protocols,” *JCI Insight*, vol. 2, no. 6, p. e90521, Mar. 2017, doi: 10.1172/JCI.INSIGHT.90521.

[257] E. Vivier, E. Tomasello, M. Baratin, T. Walzer, and S. Ugolini, “Functions of natural killer cells,” *Nature Immunology 2008 9:5*, vol. 9, no. 5, pp. 503–510, Apr. 2008, doi: 10.1038/ni1582.